AD A047610

AFGL-TR-77-0104

INVESTIGATIONS OF TECTONIC STRESS

by Charles B. Archambeau

The Regents of the University of Colorado
Boulder, Boulder County
Colorado 80309

DDC
RECEIVED
DEC 13 1977
F

26 April 1977

Final Technical Report for Period 16 September 1975 - 31 December 1976

Approved for public release; distribution unlimited

Sponsored by

Defense Advanced Research Projects Agency
ARPA Order No. 1795 - Amendment #5

Monitored by

AIR FORCE GEOPHYSICS LABORATORY
AIR FORCE SYSTEMS COMMAND
UNITED STATES AIR FORCE
HANSCOM AFB, MASSACHUSETTS 01731

AD No.
DDC FILE COPY

ARPA Order Number
1795

Program Code Number
FY7121

Name of Contractor
The Regents of the
University of Colorado

Effective Date of Contract
16 September 1975

Contract Number
F19628-76-C-0061

Principal Investigator and
Phone Number
C.B. Archambeau
(303) 492-8028

AFGL Project Scientist and
Phone Number
Ker Thomson
861-3661

Contract Expiration Date
31 December 1976

The views and conclusions contained in this document are those of the authors and should not be interpreted as necessarily representing the official policies, either expressed or implied, of the Defense Advanced Research Projects Agency or the U.S. Government.

Qualified requestors may obtain additional copies from the Denfense Documentation Center. All others should apply to the National Technical Information Service.

Unclassified

SECURITY CLASSIFICATION OF THIS PAGE (When Data Entered)

REPORT DOCUMENTATION PAGE	READ INSTRUCTIONS BEFORE COMPLETING FORM
1. REPORT NUMBER: AFGL-TR-77-0104	2. GOVT ACCESSION NO.
3. RECIPIENT'S CATALOG NUMBER	
4. TITLE (and Subtitle): INVESTIGATIONS OF TECTONIC STRESS,	5. TYPE OF REPORT & PERIOD COVERED: Final Technical Report, 16 Sept 75 - 31 Dec 76
6. PERFORMING ORG. REPORT NUMBER	
7. AUTHOR(s): Charles B. Archambeau	8. CONTRACT OR GRANT NUMBER(s): F19628-76-C-0061
9. PERFORMING ORGANIZATION NAME AND ADDRESS: The Regents of the University of Colorado, Boulder County, Boulder, Colorado 80309	10. PROGRAM ELEMENT, PROJECT, TASK AREA & WORK UNIT NUMBERS: ~~PE62701E~~ ARPA Order No. 1795
11. CONTROLLING OFFICE NAME AND ADDRESS: Air Force Geophysics Laboratory, Hanscom AFB, Massachusetts 01731, Contract Monitor/Ker Thomson/LW	12. REPORT DATE: 26 April 1977
	13. NUMBER OF PAGES: 158 (12 169p.)
14. MONITORING AGENCY NAME & ADDRESS (if different from Controlling Office): Defense Advanced Research Projects Agency, 1400 Wilson Blvd., Arlington, VA 22209	15. SECURITY CLASS. (of this report): Unclassified
	15a. DECLASSIFICATION/DOWNGRADING SCHEDULE

16. DISTRIBUTION STATEMENT (of this Report)

Approved for public release; distribution unlimited

17. DISTRIBUTION STATEMENT (of the abstract entered in Block 20, if different from Report)

18. SUPPLEMENTARY NOTES

Sponsored by Defense Advanced Research Projects Agency
ARPA Order No. 1795 - Amendment No. 5

19. KEY WORDS (Continue on reverse side if necessary and identify by block number)

discriminants, stress field, tectonic, relaxation source models, earthquakes, $m_b - M_s$

20. ABSTRACT (Continue on reverse side if necessary and identify by block number)

Results relating to the analytical modeling of earthquakes by relaxation-source theory models are summarized. A general theory of failure using concepts of a generalized phase change is developed. Applications to explosion-earthquake discrimination and earthquake source parameter estimation, particularly tectonic stress determinations, are discussed and the theoretical basis for $m_b - M_s$ discrimination and discrimination using spectral magnitude parameters is emphasized. Computer based signal analysis methods are described and applications to the estimation of discriminatory parameters are

DD FORM 1 JAN 73 1473 EDITION OF 1 NOV 65 IS OBSOLETE

Unclassified

SECURITY CLASSIFICATION OF THIS PAGE (When Data Entered)

088400

20. illustrated, using a large data set Eurasia. Observational methods and results for P wave spectral discrimination of earthquakes and explosions are described, and it is concluded that the observed behavior of these spectral magnitudes is in agreement with the theoretical predictions and can serve as a very powerful discrimination procedure.

Stress field estimates are inferred from the set of world-wide $m_b - M_s$ data for the period 1968-1975, for the North Pacific region. The results show zones of high stress, the maximum being near 1 kbar, and that these zones are also seismic gaps. Small earthquakes occurring in these high stress regions are more explosion-like than normal due to the high stress drops associated with them.

Table of Contents

Index of Figures ---------- iv

I. Introduction---------- 1

II. Theoretical Investigations: Seismic Source Theory and Models----- 4

III. Summary of m_b vs M_s and Variable Frequency Magnitude Methods of Event Discrimination and Stress Estimation---------- 15

IV. Signal Analysis for Discrimination and Stress Estimation---------- 37

V. Stress Estimates for the North Pacific Circumference---------- 57

VI. Summary and Conclusions---------- 77

References---------- 80

Appendix A: Dynamics in Prestressed Media with Moving Phase Boundaries: A Continuum Theory of Failure in Solids - by C.B. Archambeau and J.B. Minister---------- 89

ACCESSION for
NTIS White Section
DDC Buff Section
UNANNOUNCED
JUSTIFICATION
BY
DISTRIBUTION/AVAILABILITY CODES
Dist. and/or SPECIAL
A

Index of Figures

Figure 1. Near field spectra for the Hollister earthquakes recorded at a distance of approximately 40 km from the source (U. of Washington data). 7

Figure 2. Comparison of a theoretically predicted earthquake spectrum with an observed earthquake spectrum (solid circles). The spectra are composites of both P and S waves from the event and contain both near and far field spectral components (i.e., the total field spectrum of the event). The spectrum was observed at a point only 14 km from the hypocenter of the earthquake. Harris Ranch earthquake (California) of 27 Oct 1969. (Data from Johnson and McEvilly, 1974) 9

Figure 3. Scaling of the spectrum for different fault lengths, with the ratio of the semi-major axis length to major axis length of the fault held fixed. 12

Figure 4. An example of the compressional (P) wave train predicted theoretically for a 10 km rupture in a prestressed medium. The upper figure shows the P wave part of the seismograph that would be observed at a distance of 3500 km (1 mantle arrival), the lower figure shows the P wave train that would be observed at about 2500 km (3 mantle arrivals). 17

Figure 5. Examples of Rayleigh type surface generated by different sized ruptures in a prestressed medium 18

Figure 6. Examples of Love type (pure shear) surface waves generated by the same set of theoretical earthquake models used in Figure 5. 19

Figure 7. Theoretical seismograms at an epicentral distance of $\approx$ 4050 km and two azimuths with respect to the strike-slip earthquake sources. All records have been scaled to stress drop $\sigma(0)$ = 100 bars. The focal depth, fault length and m_b are indicated on each record. At left is the maximum peak-to-peak amplitude in millimicrons at 1 Hz. The bar indicates the phase at which the m_b measurement is made and T is the apparent period of this phase. 21

Figure 8. Theoretical seismograms for several azimuths for an earthquake source at two orientations, strike-slip dip-slip. The source depth is 25 km and the epicentral distance is 4000 km. 23

Figure 9. Theoretical seismograms for five depths and two epicentral distances for the relaxation source model of Archambeau (1968). The faulting is strike-slip and the azimuth is 30° from the strike. 25

Figure 10. Theoretical m_b-M_s curves for dip-slip earthquakes at 10 km depth all with the same rupture velocity $v_R = .9\ v_s$, but having variable maximum dimension and stress drop. 27

Figure 11. Theoretical and observed m_b-M_s data for Alaskan-Aleutian Arc region earthquakes in the depth range from 0 to 20 km. The curves shown on the figure are parameterized with respect to stress drop with the rupture dimension variable along each of the curves. 29

Figure 12. Application of a "comb" of narrow band filters to seismic events to obtain spectral amplitudes and time of energy arrival for several frequencies in the seismic band. An explosion and a deep earthquake are illustrated. The amplitudes obtained are used to compute variable frequency magnitudes $\bar{m}_b(f)$ for P waves. 31

Figure 13. Theoretically predicted spectral body wave and surface wave magnitudes $\bar{m}_b(f)$ and $\bar{M}_s(f)$ for earthquakes and explosions illustrated by a series of plots of m_b vs $\bar{M}_s$ and $\bar{m}_b(f_1)$ vs $\bar{m}_b(f_2)$ with $f_2 > f_1$. The first plot, at the upper left, shows the typical variation of the $\bar{m}_b$ vs $\bar{M}_s$ curve for different prestress levels. Similar variations apply to all the plots. 34

Figure 14. Signal Analysis Program Flowchart. 39

Figure 15. Flowchart indicating principal mathematical operations embodied in the signal analysis program. 40

Figure 16a. Original time series. 43

Figure 16b. Summed time series. 43

Figure 16c. Filter envelopes - original signal. 44

Figure 16d. Filter envelopes - composite signal. 44

Figure 16e. Sum of envelopes - original signal. 45

Figure 16f. Sum of envelopes - composite signal. 45

Figure 17. Examples of increaing signal-to-noise ratio for a presumed explosion (top left frame) recorded at Norway with successive application of high frequency narrow-band filters. Arrow at top denotes approximate arrival times of the P-wave on the unfiltered trace. 47

Figure 18. Polarization filtering of Chartreuse-KNUT record (Δ = 312 km) where indicated phase arrivals are predicted for body phases. 49

Figure 19. Spectral magnitudes, $\bar{m}_b$, computed at 0.45 Hz and 2.25 Hz. The presumed explosions numbered 35 and 138 occurred at Novaya Zemlya. 53

Figure 20. Spectral magnitude estimates at f_c = 0.6 Hz and f_c = 5.0 Hz for an event population recorded at the Oyer array in Norway. 54

Figure 21. Maximum filter amplitudes with noise correction for the same event population plotted in Figure 20. 55

Figure 22. Observed m_b-M_s data for the Alaska-Aleutian Arc Seismic Region shown with the theoretical m_b-M_s curves with prestress as a parameter for the curves and fault length variable along each curve. Theoretical curves and data are for dip slip and thrust events. 58

Figure 23. Observed m_b-M_s data for the California Nevada seismic region shown with theoretical m_b-M_s curves for thrust and dip slip type earthquakes. 59

Figure 24. Observed m_b-M_s data for the Japan-Kuriles-Kamchatka seismic region shown with theoretical m_b-M_s curves for thrust or dip slip earthquakes. The events observed are essentially all thrust or dip slip type. The mean stress drop for the population is somewhat larger than 100 bars with many events having stress drops near 1 kilobar. 60

Figure 25. Epicenter stress map from events in Alaskan-Aleutian Arc region having focal depths in the range from 0 to 20 km. Each event is denoted by a time sequenced event number, the stress drop and its m_b and M_s values as shown in the legend. The stress drop values are contoured to show the spatial stress pattern and provide a useful indication of the consistency of the results. The event numbers provide an indication of the time sequence of the sampling. If shear melting occurs in the failure zone (on the failure "plane"), then the stress levels shown are equal to the ambient prestress levels in the material. 63

Figure 26. Epicentral stress map for events in the Alaskan-Aleutian Arc region having focal depths in the 20 to 33 km range. Events listed as being at a depth of 33 km are omitted from the data set shown and are treated separately since the assignment of a 33 km depth is the indication of unknown depth for an event. Note the high stress zones along the Alaskan peninsula in this depth range. This high stress zone appears to be correlated with the high stress region plunging downward and eastward along the Pacific plate boundary. 64

Figure 27. Epicentral stress map from events in the Alaskan-Aleutian Arc region having focal depths in the 33 to 40 km range. Events listed with hypocenters at 33km are omitted. The high stress zone along the Alaska Peninsula is seen to persist through this depth interval, with the stress levels being, again, near the 1 kilobar level. 65

Figure 28. Epicentral stress map from events in the Alaskan-Aleutian Arc region having focal depths in the 40 to 50 km range. The high stress zone along the peninsula is larger and more extensive in this depth range than at the shallower depths. It is likely to be the depth range for nucleation of a very large earthquake as a result of failure along the plate boundary from just west of Kodiak Island to the end of the Alaskan Peninsula. For stress levels near 1 kbar, as shown, this event could occur at any time. 66

Figure 29. Epicentral stress map from events in the Japan-Kuriles-Kambhatka region for the depth range from 0 to 20 km. The high stress zone in the Kuriles region corresponds to a shallow stress concentration of apparently large dimension within the Asian plate, which is being underthrust by the Pacific plate.

Figure 30. Epicentral stress map from events in the Japan-Kuriles-Kamchatka region for the depth range from 20 to 33 km. High stress zones occur along the Kamchatka and Hokkaido-Honshu coasts, with the latter zone showing a complex pattern of high and low stresses characteristic of zones of recent large earthquakes such as event no. 61. 69

Figure 31. Epicentral stress map from events in the Japan-Kuriles-Kamchatka region for the depth range form 33 to 40 km. The high stress zone off the Honshu coast appears more regular and extensive in this depth range and constitutes a high risk zone--especially in view of its proximity to Tokyo. 70

Figure 32. Epicentral stress map for the Japan-Kuriles seismic region from events having focal depths in the depth range 40 to 50 km, with events occurring before the large event, No. 193, represented. This event and its aftershocks occurred within the moderately high stress zone off the northeast point of Hokkaido and results in a considerable change in the stress level and spatial pattern. 73

Figure 33. Epicentral stress map for the Japan-Kuriles-Kamchatka seismic region from events having focal depths given as 33 km, with only the events before the large event No. 144 represented. Event No. 144, which occurred off the coast of Kamchatka, and its aftershocks are not included so that the stress field prior to this event is shown. It corresponds to the northern-most high stress zone along the Kamchatka coast. 74

Figure 35. Epicentral stress map for the Japan-Kuriles-Kamchatka from events with focal depths at 33 km, with event No. 144 and its aftershocks included. The stress field in the northern high stress zone is now much reduced, with some high stress indicating events occurring near what appears to be the edges of the new failure zone. The stress level, as evidenced by the event sampling, therefore appears to be much lower, as would be expected, but with higher stress near the edges of the recent failure "plane" formed by the large event, as also would be required. 75

I. Introduction.

The principal objectives of this study were to:

(1) Refine and extend both the theory of earthquake radiation field generation and the approximate models derived from this general theory.

(2) Apply the theory in a manner designed to provide a theoretical basis for the currently used discrimination methods, in particular the m_b vs M_s method.

(3) To design and verify new discrimination methods which are simplier, more reliable and that apply over a larger magnitude range than the m_b vs M_s method.

(4) To reliably estimate earthquake source parameters, in particular tectonic stress drops, using the theory as a framework for the interpretation and as a basis for defining appropriate observational measurements.

(5) To study earthquakes found to be high stress drop events with emphasis on testing the discrimination methods with these events.

The results of the work in these areas is discussed in the following sections. The emphasis has been nearly equally divided in the first four areas, while the final objective has been much less developed in terms of final results. The theoretical work, discussed in the next section II has resulted in the development of a very general theoretical framework for the description of the radiation fields from earthquakes. We are still developing specific models involving considerations of failure zone geometry, boundary condition approximations and prestress spatial variations. However a number of first order models have been constructed and are in use. They appear to be in rather surprisingly good agreement with observations and complex numerical models of earthquakes.

The source theory coupled with rather general wave propagation theory has been used to generate theoretical m_b and M_s predictions for a wide class of earthquakes. These results, when compared with comparable results for explosion sources, provide a detailed explanation of the m_b vs M_s discriminant. These results are discussed and illustrated in sections III and IV of this report.

We have also devised a variable frequency magnitude discriminate employing magnitude measurements at particular fequencies, for both body and surface waves, with a pair of such measurements used in the same manner as the (m_b, M_s) pair for discrimination of explosions and earthquakes. A high frequency body wave discriminate, using an event magnitude pair measured near .4 Hz and near 3 Hz has been studied extensively using hundreds of actual events from Eurasia. We find this discriminate to be superior to the m_b vs M_s approach and to be applicable over a wider event magnitude range. The method is also less costly to implement and has been computer automated so that it is easy and cheap to apply. This approach is discussed in sections III and IV.

Several hundred events from the Alaska-Aleutians and Japan-Kamchatka regions were used to infer the tectonic stress levels within the lithosphere. The theoretical m_b vs M_s results were used as the basis for the inference of stress drop and final, maximum, failure zone dimension. Moderate sized events were used in this study in order to avoid uncertainties associated with strongly variable prestress and stress drop. These latter problems and considerations are discussed in the following section II while the results of the stress study are summarized in section V.

Much of the work reported has been carried on in a joint research effort with personnel at Systems, Science and Software and with J.B. Minster at

the California Institute of Technology. Therefore the work reported has been jointly supported by a number of agencies under several grants and contracts, both at CIRES and at the other organizations. However, all the work reported has at least in part been supported under this contract.

II. Theoretical Investigations: Seismic Source Theory and Models.

Relaxation theory models have been used to provide a description of the radiation field from an earthquake. The theory is described by Archambeau (1968, 1972) and Minster (1973). The Appendix A contains a very general formulation of the theory that incorporates the dynamical boundary conditions explicitly in a general Green's function formulation (Archambeau and Minster, 1977). Minster (1973) and Minster and Archambeau (1977) have incorporated the theory in computer codes which allow detailed computation of the radiated field from a number of models and these have been combined with body and surface wave propagation methods to allow the field to be predicted at both near and teleseismic distances, in both the time and frequency domains (Cherry et al., 1973; Cherry et al., 1974; Savino et al., 1975; Bache and Archambeau, 1976; Bach and Harkrider, 1976). The wave theory has been adapted from a number of sources and utilizes generalized ray methods (e.g., Gilbert and Helmberger, 1972; Wiggins and Helmberger, 1973) as well as classical ray theory and full wave theory for both body and surface waves (e.g., Bach and Harkrider, 1976; Harkrider, 1964; and Harkrider and Archambeau, 1976). The wave propagation theory is reasonably straight forward and we use either a generalized ray theory or full wave theory when required--such as in the near field distance range from the source, at caustics at teleseismic distance ranges and in the computation of the crustal transfer functions at the source and receiver. For studies of some classes of events, in particularly complex structural regions, we can employ three dimensional ray tracing (e.g., Engdahl, 1973; and Engdahl and Lee, 1975).

Current relaxation theory models are also being refined to include effects such as spatially variable prestress (and stress drop) and variable rupture velocity. They are also being extended to account for the dynamic

boundary conditions connecting these variables (Archambeau and Minster, 1977). In addition, source models with ellipsoidal rupture zones and with variable failure material properties will be included, with all these complications being incorporated through the use of combined numerical-analytical methods. These developments were partially completed during the contract period of this report with the results to be incorporated as the models are perfected. It is felt that in view of the clear evidence for complex failure behavior, such as variable stress drops along the failure "plane" (e.g., Jungels, 1973, Jungels and Frazier, 1973; Hanks, 1974) as well as observations of "multiple events" which is another (extreme) manifestation of variable stress drop; then it is important to obtain "higher order" models so that we can investigate and assess the importance of these effects in detail (see also Archambeau, 1975, for additional comments).

In this regard, however, we have compared predictions of the currently used relaxation theory models to numerically computed radiation fields from relatively complex two and three dimensional failure models incorporating plasticity and a rather general failure condition (Cherry, Bache and Masso, 1976 and Cherry, Halda and Hamilton, 1976). The fields obtained from the numerical calculations were compared to those predicted from the analytical relaxation theory models, for which the same prestress, rupture velocity and maximum rupture dimension were used, and it was found that the two results were essentially the same. This implies that the analytical models, even though idealized and employing a failure zone of circular cross-section, are good approximations to failure situations in which the failure region is both narrow and subject to nonlinear flow laws. This

agreement also suggests that the radiated field is insensitive to the thickness of the failure zone used in the models, so long as the overall surface area of the failure region is comparable to that for the (expected) thin zone. Further the results imply that the radiated field is also insensitive to any localized plastic flow occurring near the rupture front prior to actual failure, so long as the failure rate used for the analytical model is comparable to the rate of actual failure zone growth. The numerical modeling did not, however, include spatial variations of prestress, so no detailed information on the effect of prestress concentration was obtained; nor could we therefore make comparisons to the approximations used in current relaxation source theory models to account for stress localization effects (i.e., to evaluate the "R_s approximation" as introduced by Archambeau, 1968.) However, additional work in this area is in progress and we hope to evaluate its influence on the radiated field in general circumstances.

The spectral complications of the observed seismic field from earthquakes are indicated by the spectra shown in Figure (1). The data were recorded in the near field distance range by the University of Washington and displacement spectra for several earthquakes are shown. The detectors were long period vertical seismometers, and the noise at high frequency is rather high.

It is apparent that all the spectra are quite strongly peaked and that at low frequency the spectra increase as f^{-n}, with $n \gtrsim 1$. The latter effect is expected to be f^{-1}, due to the static offset in displacement from "near field" terms, and the observed variation may be a combination of the expected behavior and noise (of various origins). The peak in the spectra may be due to interference due to wave propagation effects giving rise to cancellation and a spectral "hole" (between -1.5 and -1.0 on the

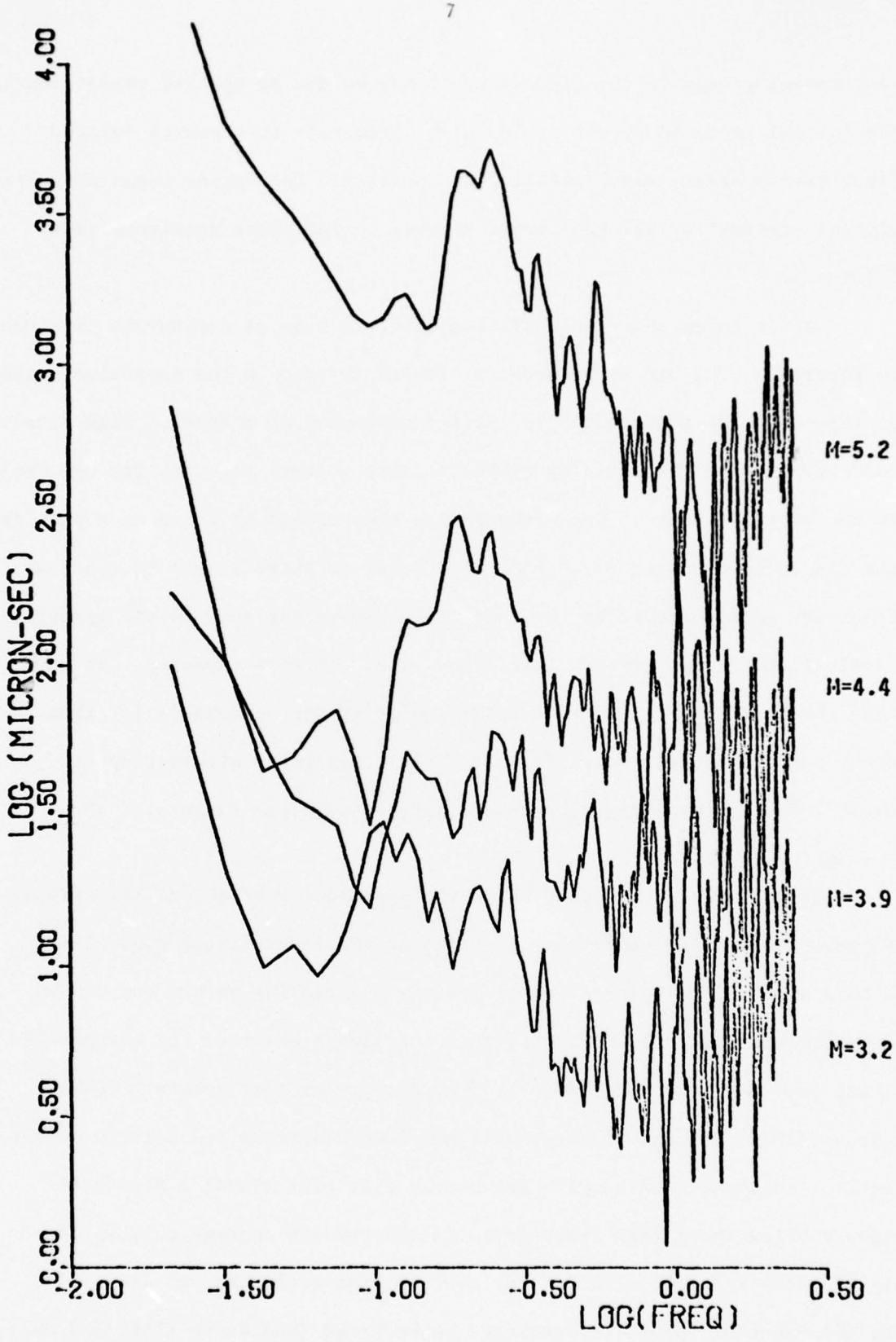

Figure 1. Near field spectra for the Hollister earthquakes recorded at a distance of approximately 40 km from the source (U. of Washington data).

log frequency axis in the figure) or it may be due to spatial variations in the initial tectonic stress field which gives rise to a source related interference effect and a peak in the spectrum. The latter seems more likely since it occurs for all the events as well as for other receivers (see Figure 2).

A fit to an observed radiation spectrum from an earthquake is shown in Figure 2. The distance factor R_s (which is used in the approximate theory to represent the characteristic spatial dimension of a zone of high stress concentration in the vicinity of the failure volume) accounts for the "hole" in the spectrum near .1 Hz, although its true effect is to cause a peak in the displacement spectrum so that the "hole" is actually due to a higher frequency peak followed by the near field caused increase in the spectral level at much lower frequencies (below .1 Hz, in this example). In any case the fault dimensions and rupture velocity are reasonable for this event and a prestrain level (e) of 5×10^{-4} implies a stress drop of about 150 bars for a rigidity change before and after failure of about 3×10^{11} dynes/cm^2.

It should be noted that while the spectral observations illustrated in Figures 1 and 2 indicated complications at the lower frequencies giving rise to a spectral peak (or a spectral minimum depending on how one wishes to describe the spectra), this effect is not always observed for earthquakes - at least over a fairly wide range of frequencies for some events. Tucker and Brune (1973) for example have obtained S wave spectra for a large number of small aftershock events which are nearly flat over almost a decade of frequency below the corner frequency. In the present context this would imply that the spatial extent of the zone of high prestress was large. In fact, the spectral "peak" is predicted to be broad (and quite flat) and only

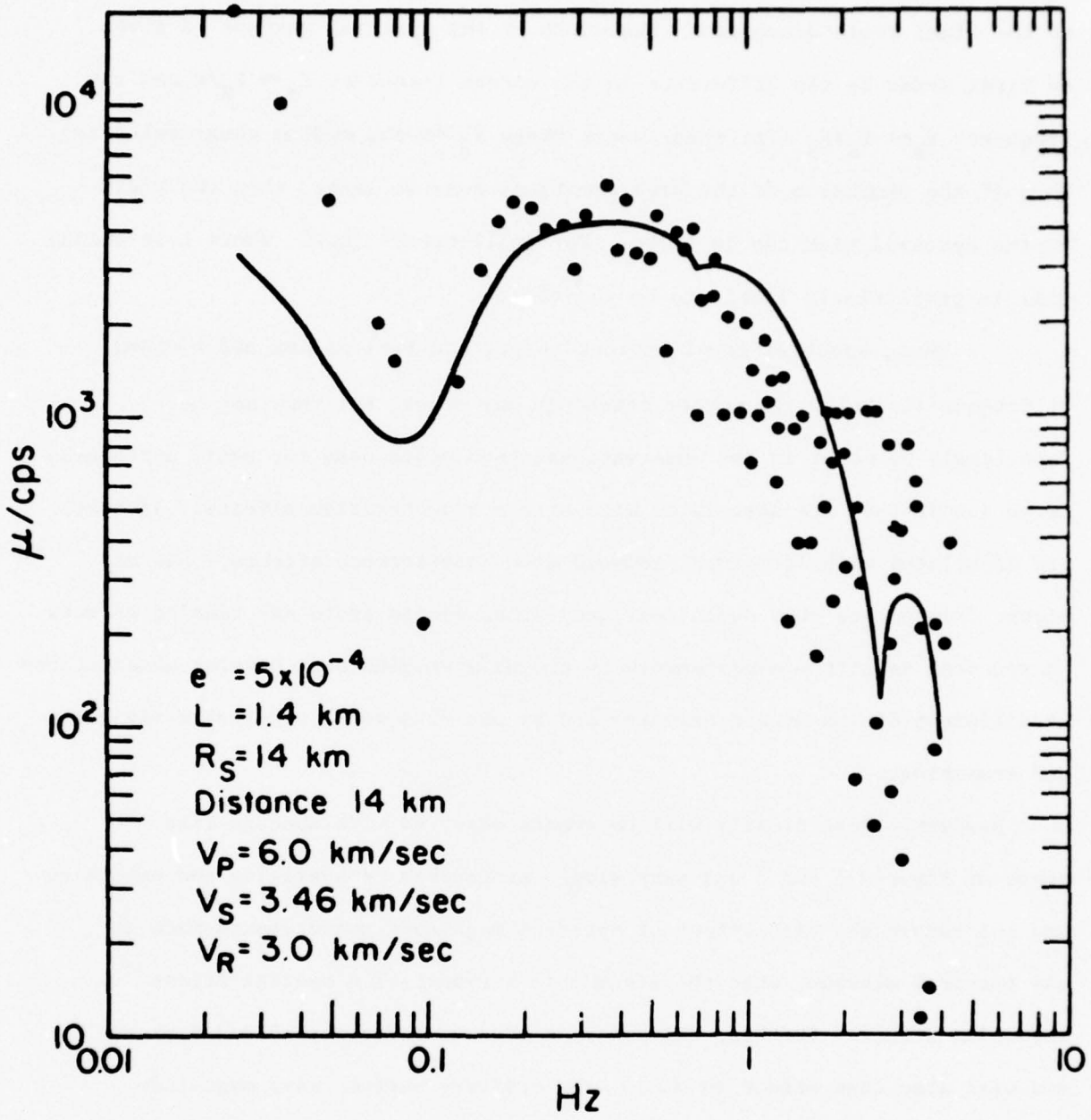

Figure 2. Comparison of a theoretically predicted earthquake spectrum with an observed earthquake spectrum (solid circles). The spectra are composites of both P and S waves from the event and contain both near and far field spectral components (i.e., the total field spectrum of the event). The spectrum was observed at a point only 14 km from the hypocenter of the earthquake. Harris Ranch earthquake (California) of 27 Oct. 1969. (Data from Johnson and McEvilly, 1974.)

sharply peaked when the dimension (R_s) of the high stress zone is comparable to the final fault dimension. The width of the spectral maximum is given to first order by the difference in the corner frequency $f_c \sim V_R/L$ and the frequency $f_s \sim V_S/R_S$ (for shear waves where V_S is the medium shear velocity). Thus if the dimension of the high prestress zone is large, then the width of the spectral peak can be large. For small events (i.e., where L is small) this is particularly likely to be the case.

Thus, spectral complications (e.g., spectral maxima and minima) at frequencies below the corner frequency may occur, but they may be less likely to occur in the observational band width used for small earthquake detection if they are associated with stress concentration effects. If they are associated with structural induced wave interference effects - and at higher frequencies they definitely are - then we can avoid any biasing effects in spectral magnitude measutements by proper averaging over several observations at different distances and aximuths and by use of several spectral estimates and smoothing.

However, there clearly will be events observed with spectra like those of Figures 1 and 2 and such simple procedures as averaging and smoothing may not remove the bias effect of spectral magnitude measurements made in the spectral minimum, when the minimum is a result of a spatial stress variation effect. Further, this minimum may occur for both P and S waves and will also then affect (reduce) the ordinary surface wave magnitude value, M_s, for such events. We therefore seek to avoid making any measurement in this zone for the class of small earthquakes we intend to use for stress estimation, whether or not the effect occurs. We can also use spectral magnitudes for discrimination that are unlikely to be affected. This is

not difficult to do if the characteristic dimension of the uniformly high initial stress zone is of the order of 10 to 20 km and larger in the vicinity of earthquakes. In particular, Figure 3 shows theoretical spectra for earthquakes with small maximum dimensions (from 1 km up to 10 km) where the characteristic dimension for the stress concentration varies with the fault dimension from 10 km to 100 km. From this figure we see that for small earthquakes, if we use a low frequency magnitude estimate near .3 Hz and a high frequency magnitude estimate near 5 Hz, we can be quite confident that the low frequency estimate will lie on or near the broad maximum of the P wave spectrum while the high frequency estimate will be above the corner frequency on the declining high frequency slope. In this case, the only parameters controlling the spectrum in this range are the rupture dimensions, the stress drop and the rupture velocity and in terms of the measured spectral magnitudes used for discrimination and source parameter estimates the events appear as normal earthquakes. Normally for stress estimates the rupture velocity is assumed to be about .8 of the local shear velocity, so the remaining two parameters affecting the measured spectral magnitude are the rupture length and stress drop. These event parameters can then be determined using pairs of spectral magnitude estimates - as will be discussed in more detail in the following sections. Further use of the "high" frequency spectral magnitudes for discrimination avoids or minimizes the possible problem of a spectral minimum at low frequency causing a depression of the low frequency magnitude estimate (such as could occur for an M_s measurement). Such depression could, when low and high frequency magnitudes are used, cause merging of the earthquake population and the explosion population. Hence use of a high frequency body wave spectral magnitude discriminant appears to be better approach to explosion-earthquake discrimination then the

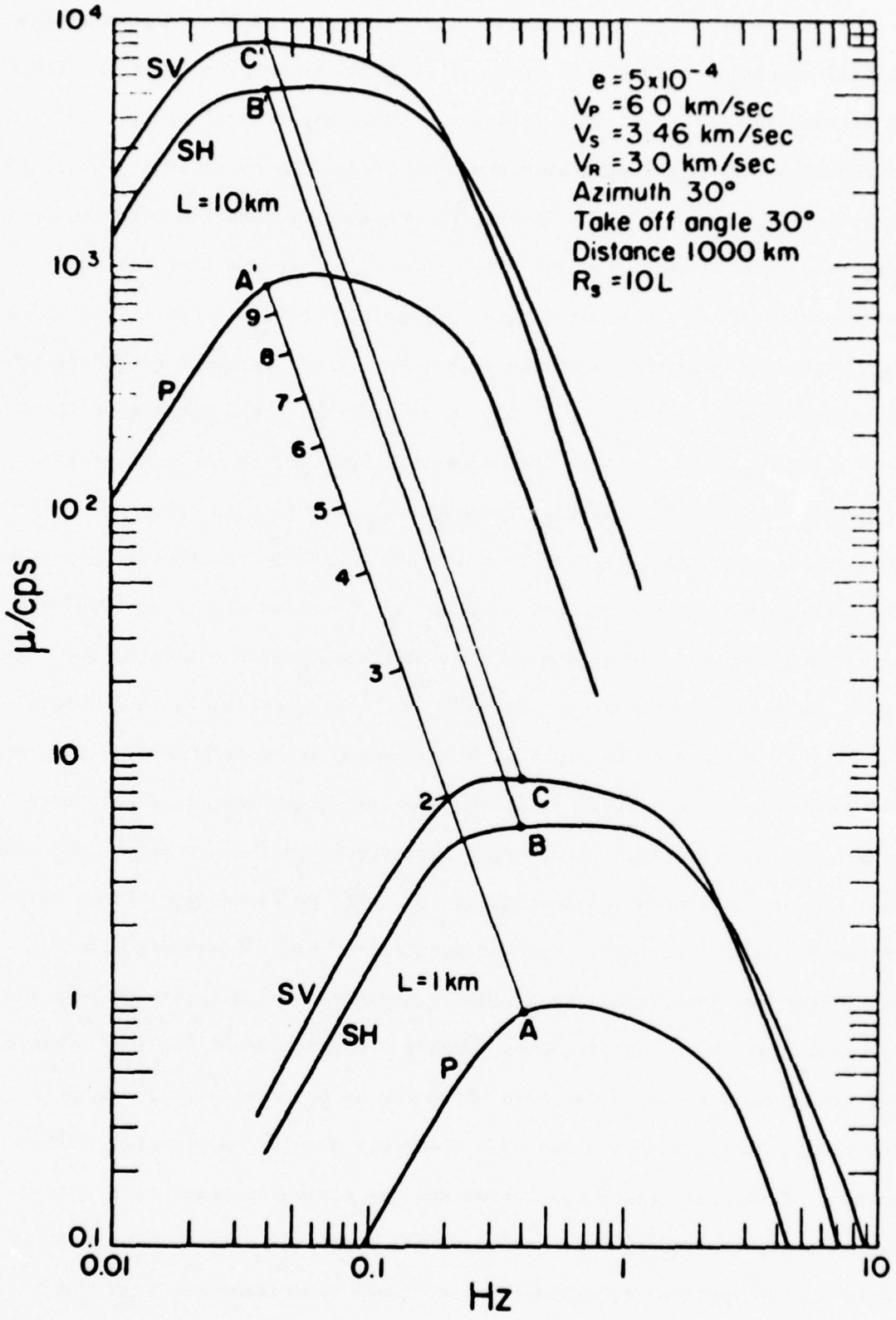

Figure 3. Scaling of the spectrum for different fault lengths, with the ratio of the semi-major axis length to major axis length of the fault held fixed.

$m_b - M_s$ method for this reason, as well as because it is simpler and has a greater magnitude range of applicability.

If the spatial stress concentration has a characteristic dimension of the order of or greater than 50 to 60 km for all events then M_s magnitudes would not be affected by any spectral minimum associated with the prestress. It may be the case that most events satisfy this condition, however it is quite possible that some small events are the result of failure within small zones of high stress concentration. In general then, it is safest to use as high a frequency as possible for the low frequency magnitude used in discrimination with the variable frequency magnitude approach.

The remaining theoretical problems relating to discrimination and source parameter estimates are largely connected with the stress concentration effects as has already been observed. There is still considerable controversy (see for example Archambeau, 1975) about the manifestations of variable stress drop and prestress in the radiated seismic field from an earthquake. It has therefore been our approach in this study to design methods of stress estimation and event discrimination that avoid use of data that may be effected by the stress spatial variability, while simultaneously attempting to resolve the theoretical questions in a rigorous fashion. The later effort seems to be quite close to a final solution, but will require somewhat more effort. We think, at the moment at least, that the approximate method involving the use of a characteristic dimension (R_s) for a stress concentration (E.g., Archambeau, 1968) is roughly correct in terms of the predicted effects on the radiation field, but of course, this cannot be rigorously supported now.

In applications of the theory to predictions of m_b and M_s for use in discrimination and stress estimates, we have assumed that the prestress zone is uniform over a region of 50-60 km, so that the M_s value is not affected by any stress concentration effects and also have confined ourselves to the analysis of moderate sized earthquakes where this is very like to be true.

A major part of our theoretical work has been directd to the formulation of relaxation source theory in a rigorous and general manner that explicitly accounts for the dynamical boundary conditions on an expanding failure boundary. We have also introduced the idea of a generalized phase change and an associated internal energy change in material parameters as a means of quantitatively describing the energetics of a failure process. This work is described in detail in the Appendix A of this report.

III. Summary of m_b-M_s and $m_b(f)$ Methods of Stress Estimation and Event Discrimination.

A basis for discrimination and identification of explosions and earthquakes, and estimation of source properties, in particular stress drop of earthquakes and energy yield of explosions, can be established through the use of:

(1) A realistic and accurate theoretical representation of the source radiation field.

(2) A reasonably accurate and detailed knowledge of the crust and upper mantle elastic and anelastic properties.

(3) The capability to generate theoretical spectra, and seismic time series for at least the major wave types comprising the seismic field observed.

(4) A large data base containing multiple seismic observations of small to moderate sized events.

(5) An efficient, fast and accurate process for estimating the important observational parameters to be used for event discrimination and in the estimation of source parameters - in particular stress for a large event set.

The first three of these elements are used to establish a theoretical basis for event discrimination and source parameter inversion and the final two are required to verify the theoretical approach and to implement it. In this section we will discuss the use of our theoretical modeling ability in establishing methods of event discrimination and event parameter determinations, in particular the stress level changes associated with earthquakes. In the previous section we have discussed the theoretical source models that will be used. In the following sections we will describe the signal analysis methods used in generating appropriate observational data and then illustrate the approach through applications giving source parameter estimates (section V) and event discrimination (section VI). The use of

the observed data is also, of course, designed to test the accuracy and reliability of the theoretical methods devised for discrimination and source parameter estimation. (Our verification criteria is based on the internal consistency of the source parameter estimates as well as upon the predictive reliability of the results.)

Theoretical m_b and M_s Magnitudes for Earthquakes.

The source models described and the ability to predict the teleseismic radiation from such models in the earth have been used to generate theoretical or "synthetic" seismograms for earthquakes of various types. In particular, theoretical seismograms have been generated for earthquakes at variable depths, in the range 0 - 50 km, with variable length, orientation (i.e., strike-slip, dip-slip, normal and thrust types) and with variable stress drops. The predicted radiation fields--consisting of compressional body waves and surface waves--from this variety of earthquakes have been computed over a range of teleseismic distances and at numerous azimuths. These detailed predictions have then been used to obtain m_b and M_s values--measured from the synthetic data and averaged by the identical procedures used in routine observational practice. The details of this computational program are described by Archambeau et al. 1974, Archambeau (1974, 1975b), Bache and Archambeau (1976) Savino and Archambeau (1976) and Archambeau (1976).

Figures (4) through (6) are examples of synthetic seismograms for a dip slip earthquake with hypocentral depth of 10 km and stress drop of 500 bars. The rupture velocity for the event was taken to be $.9v_s$, where v_s is the shear velocity at the 10 km depth in the earth model used for the structure at the source location. In this example, a continental tectonic model was used (CIT 109, Archambeau et al., 1969).

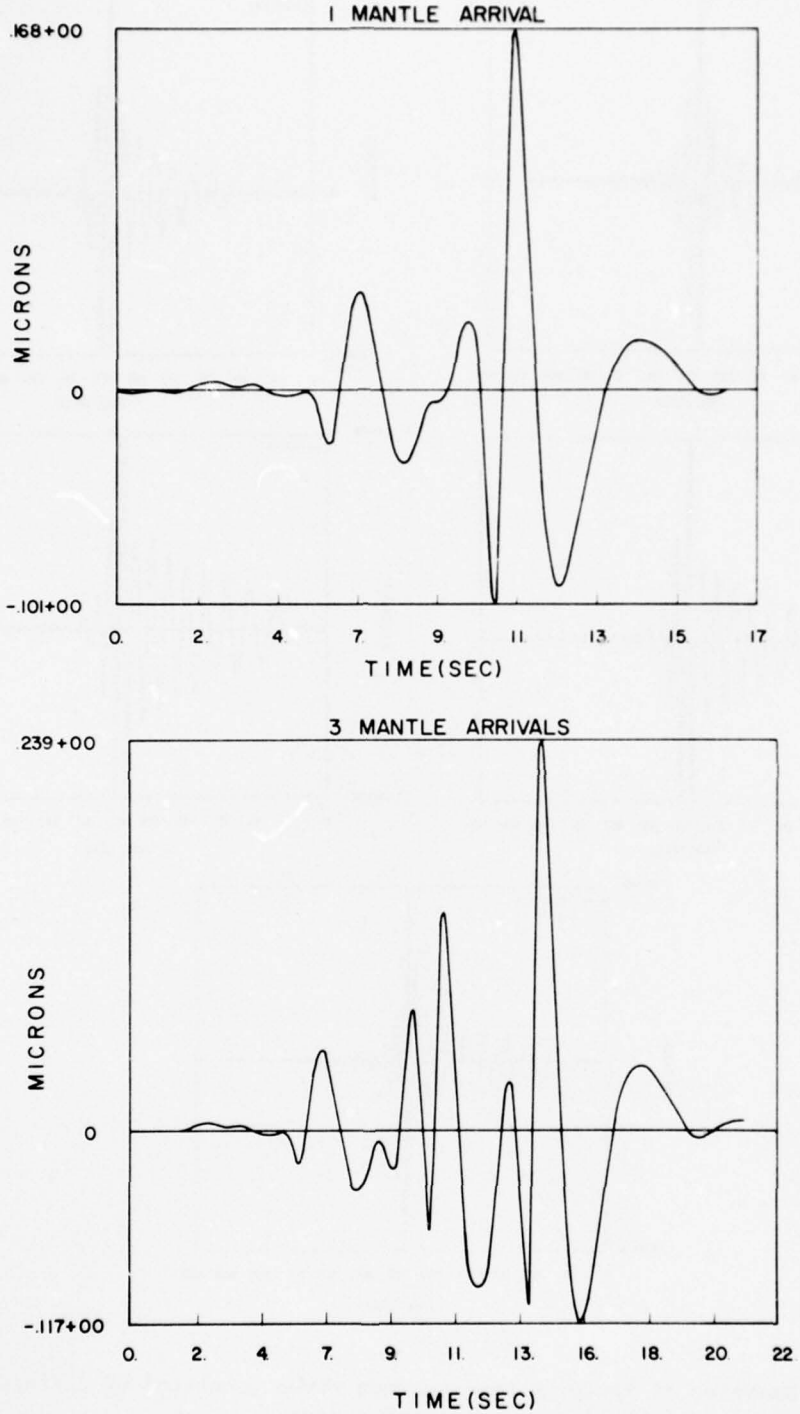

Figure 4: An example of the compressional (P) wave train predicted theoretically for a 10 km rupture in a prestressed medium. The upper figure shows the P wave part of the seismograph that would be observed at a distance of 3500 km (1 mantle arrival), the lower figure shows the P wave train that would be observed at about 2500 km (3 mantle arrivals).

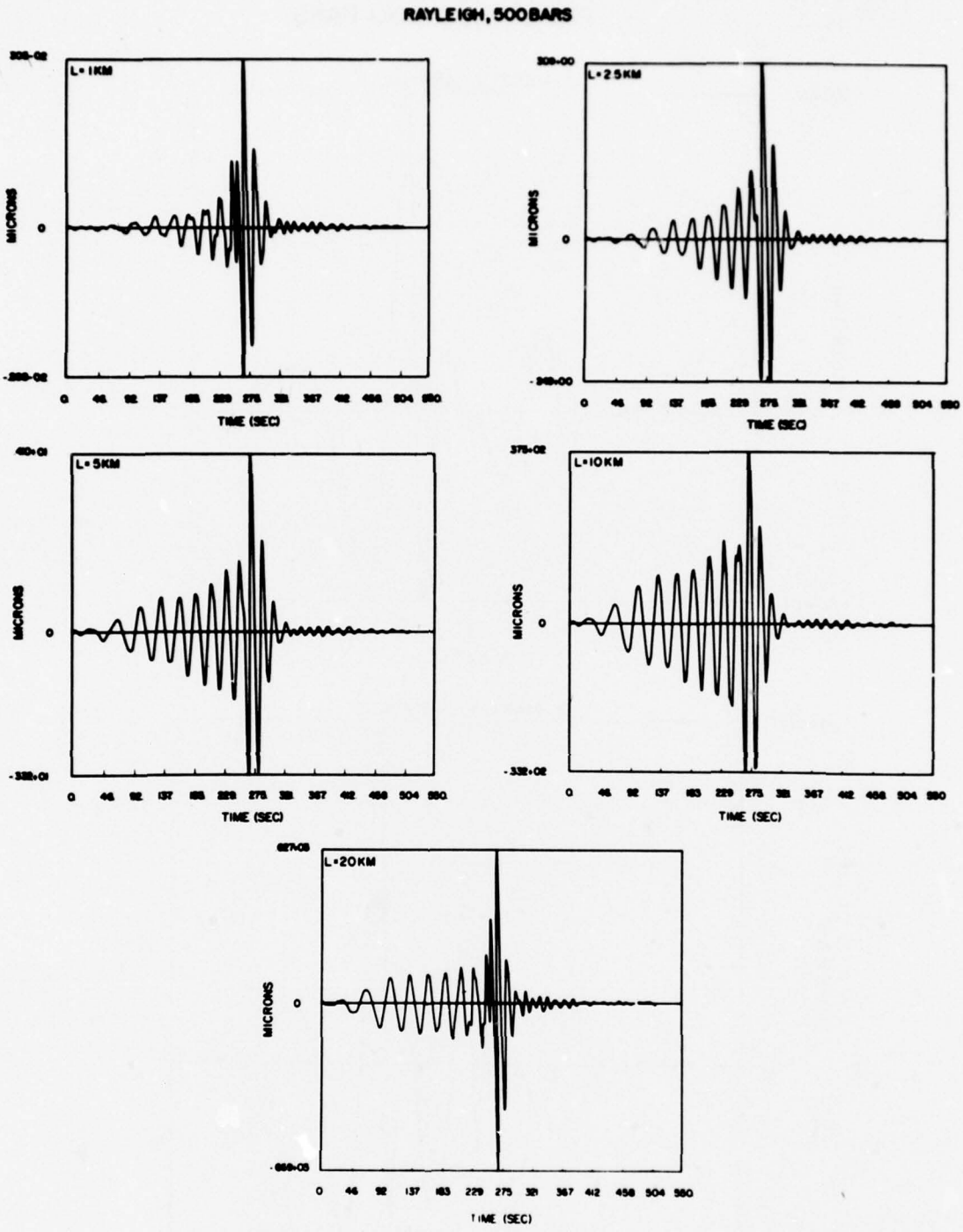

Fig. 5: Examples of Rayleigh type surface waves generated by different sized ruptures in a prestressed medium.

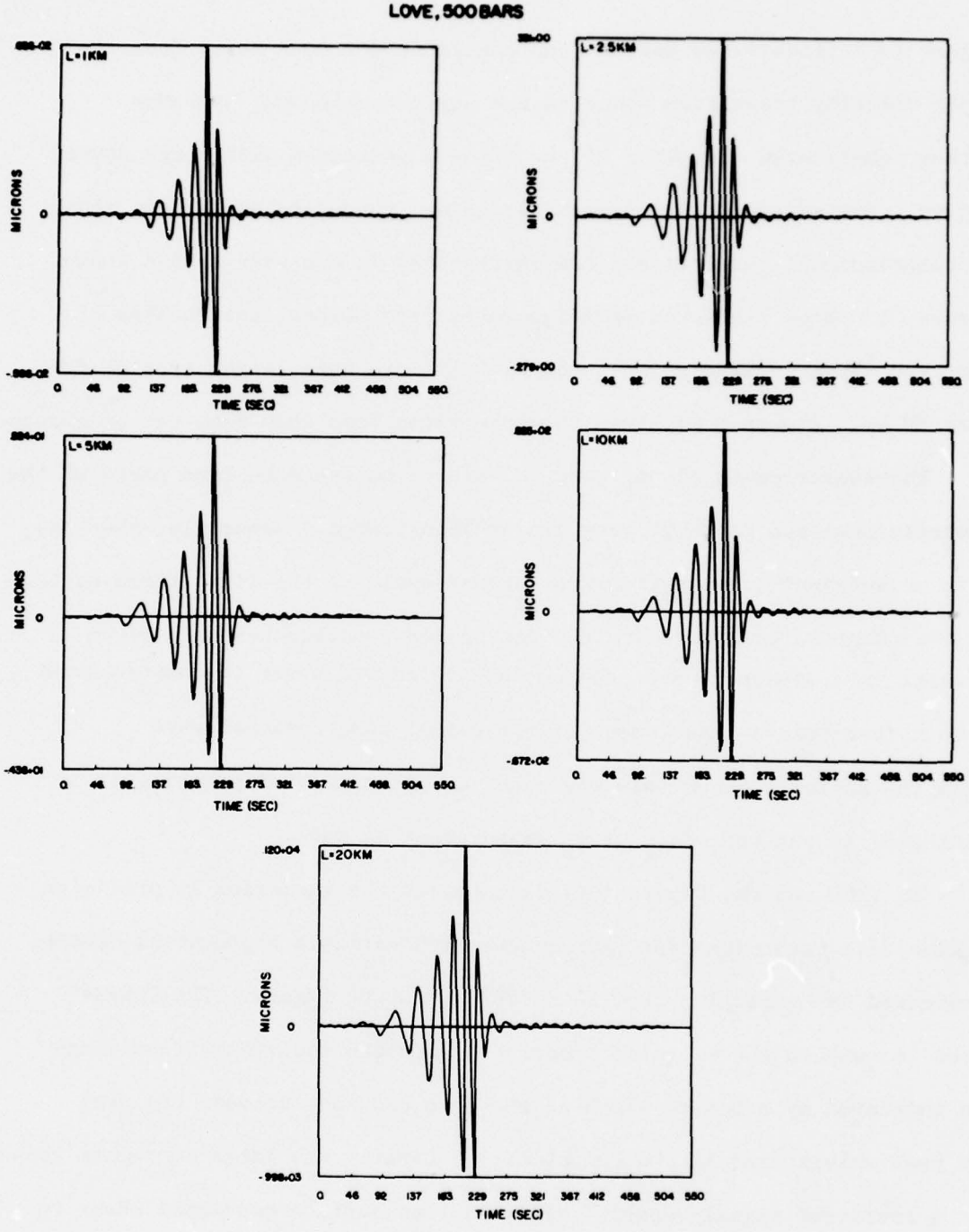

Figure 6. Examples of Love type (pure shear) surface waves generated by the same set of theoretical earthquake models used in Figure 5.

Figure (4) illustrates some of the complications that arise from the rapid velocity transition zones in the upper mantle and from the rather complicated character of the signals generated within the source region. Both direct compressional waves and converted waves (eg. shear to compressional reflections) are represented in the wave trains shown. Figure (5) shows predicted Rayleigh waves from several earthquakes of the type shown in Figure (4), but with failure zone length ranging from 1 to 20 km. Figure (6) shows the Love waves from this same set of events.

The measurements of m_b and M_s are of course made from parts of the compressional and Rayleigh wave trains illustrated. Generally, the body wave measurement is made from the largest cycle in the first three cycles of the compressional wave train. For shallow earthquakes this often results in a measurement of the surface reflected shear to compressional wave rather than a measurement of the direct compressional wave from the source. Since this may occur in observational practice it is reflected in our procedure of m_b measurement as well.

In this regard, Figure (7) illustrates the variation in predicted teleseismic recordings for earthquakes with variable hypocentral depths, indicated by H, ranging from 10 to 45 km, in the figure. The "phase" used to compute the m_b value associated with the individual recordings is indicated by a bar or slash at the zero crossing between the peak to peak values used in the computation. Clearly the large secondary phase is a converted signal--specifically the free surface converted shear to compressional wave--and for the event at H = 10 km, this phase would be used to compute the m_b value using the standard conventions applied to magnitude computations. This phase might also be used for the 15 km depth event as well.

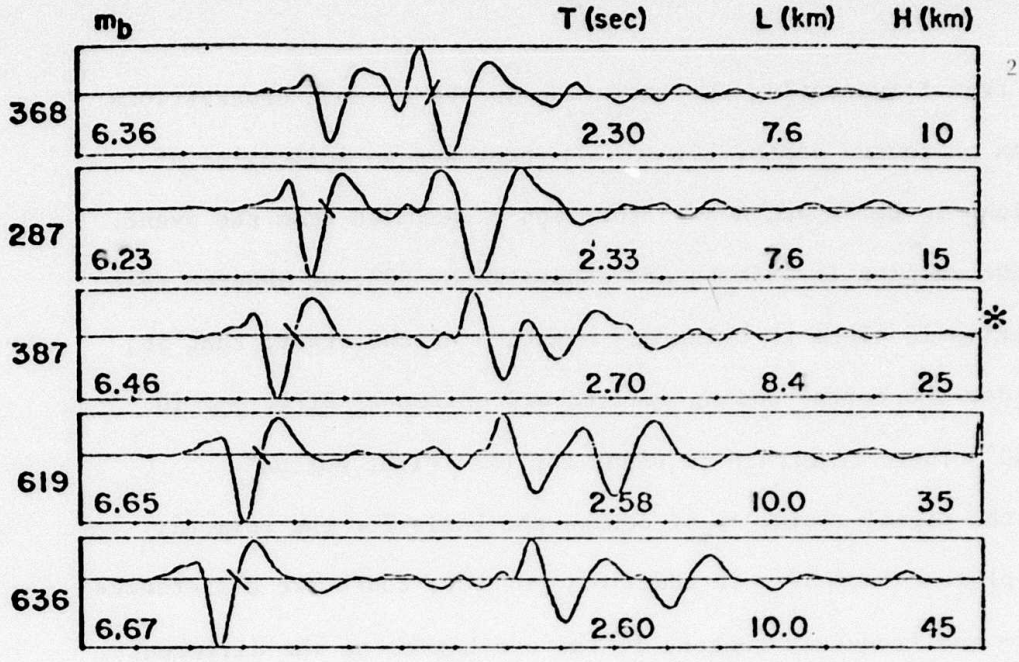

a. Azimuth, $\phi = 45°$

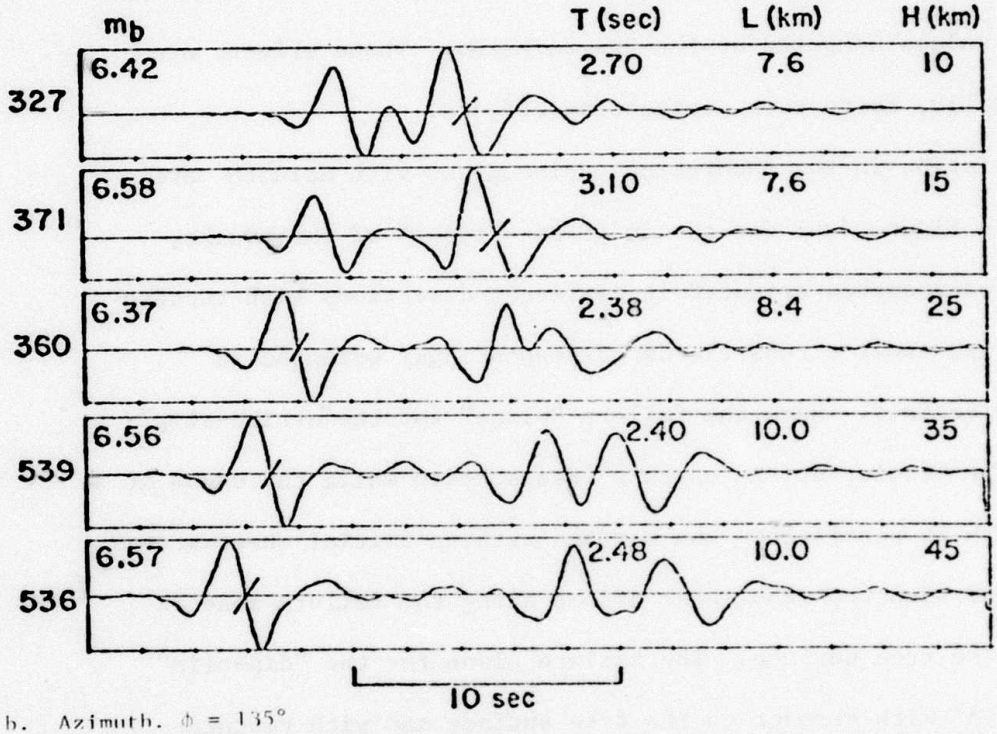

b. Azimuth, $\phi = 135°$

Figure 7: Theoretical seismograms at an epicentral distance of 4050 km and two azimuths with respect to the strike-slip earthquake sources. All records have been scaled to stress drop $\sigma^{(0)} = 100$ bars. The focal depth, fault length and m_b are indicated on each record. At left is the maximum peak-to-peak amplitude in millimicrons at 1 Hz. The bar indicates the phase at which the m_b measurement is made and T is the apparent period of this phase.

Aside from illustrating the variation in the seismic observations as functions of source depth, Figure (7) provides an indication of the variations to be expected as a function of azimuth from the event. Since the two samples in azimuth are separated by 90°, we observe that one time series is close to being the negative of the other; that is, to first order the corresponding spectra are uniformly different in phase by 180° These reversals in sign, for the "first motion" section of the signal train, is of course the basis for the commonly used fault plane solutions. In addition, however, there are differences in wave form and frequency content in the synthetics at the different azimuths, which result in variations in the effective period T measured for the so called "b phase" and its amplitude and consequently in the m_b values computed at the two azimuths. These effects are due, principally, to rupture propagation effects.

The variation in the theoretical seismograms with azimuth are also shown in Figure (8) for two different "types" of earthquake, that is for earthquakes oriented in different directions with rupture propagation and shear stress fields correspondingly oriented in different directions. Here the failure "plane" for the "strike-slip" event is perpendicular to the earth's free surface while the sense of rupture growth is parallel to the surface with an initial shear stress field oriented such that the shear offset along the failure zone is parallel to the free surface. The failure plane for the "dip-slip" event is at 45° with respect to the free surface and with rupture propagation down the plane away from the free surface , with an offset due to the prestress orientation which is at 45° to the surface.

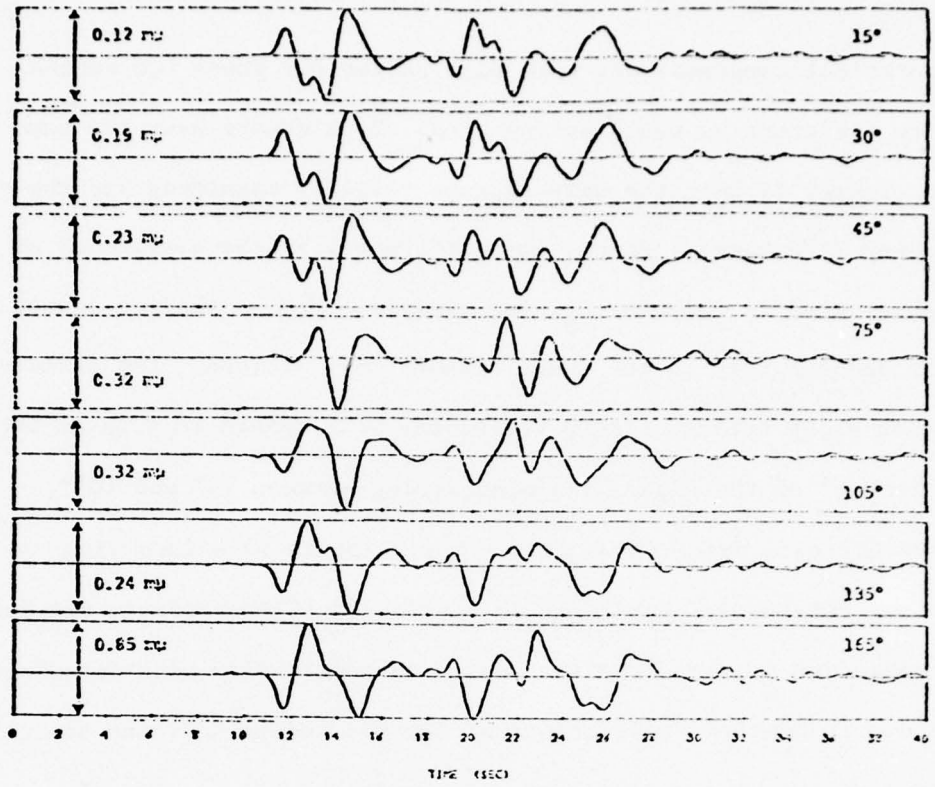

Strike-slip

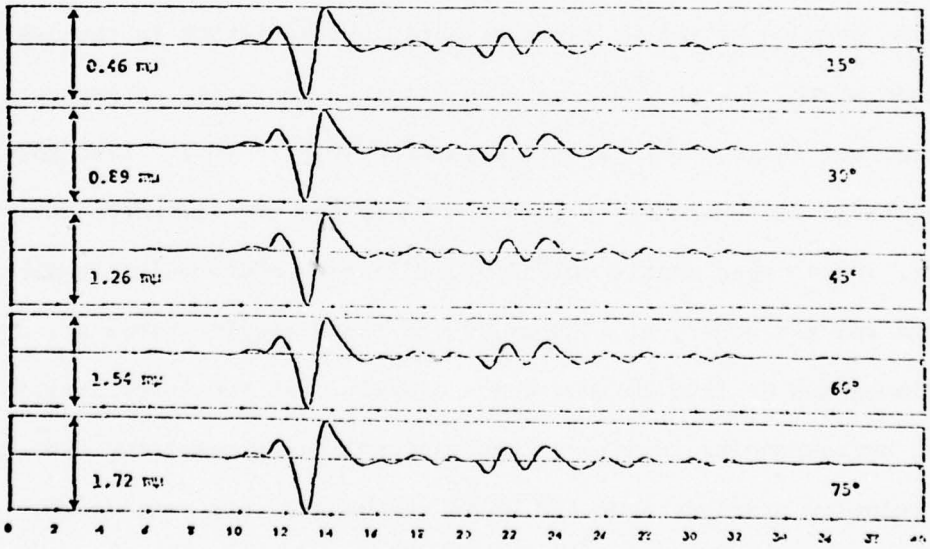

Dip-slip

Figure 8: Theoretical seismograms for several azimuths for an earthquake source at two orientations, strike-slip and dip-slip. The source depth is 25 km and the epicentral distance is 4000 km.

The theoretical compressional wave time series for these two events are quite different as would be expected. Both events have the same rupture length (1 km), the same rupture velocity magnitude and the same stress drop (100 bars). Hence, the differences in the amplitudes of the b phase used to compute m_b, for example, for the two source types is due entirely to the event orientation. Further, the strike-slip event shows strong azimuth variation, with change in sign of the "first motion" of the signal train occurring between 75° and 105°, while the dip-slip event shows little variation in wave form with azimuth but substantial variation in amplitude. These effects are due to the radiation pattern from the source in combination with interference effects due to multiple reflections within the medium near the source (principally) and at the receiver.

While the amplitude and wave form variations with azimuth and event type are seen to be rather large effects, the variation in the average amplitude of the P wave train as a function of depth is, as might be expected, not large. This is illustrated by Figure (9). Also shown is the change in character of the wave train for two distances, one at 2500 km, where upper mantle velocity gradients produce multiple direct arrivals and the other, at 4000 km, where these complications are absent. The seismograms at 2500 km show quite clearly that the later arriving energy, corresponding to direct compressional waves resulting from the sharp velocity gradient near 450 km in the mantle, are considerably larger than the first arriving compressional wave signal. In some cases at least, this signal would be used to compute the m_b magnitude.

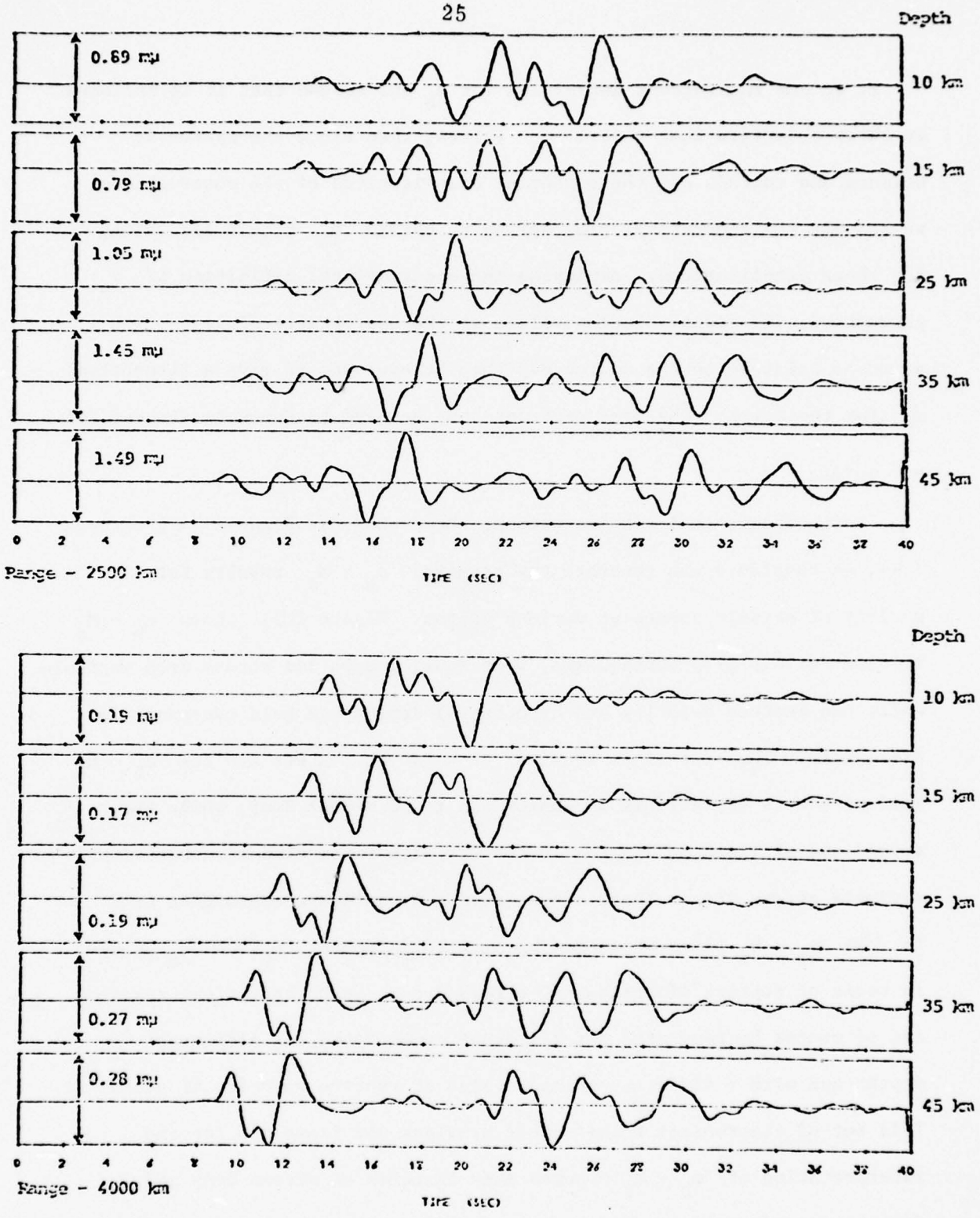

Figure 9: Theoretical seismograms for five depths and two epicentral distances for the relaxation source model of Archambeau (1968). The faulting is strike-slip and the azimuth is 30° from the strike.

If we use the current definition for m_b and assume that it is followed by those observers that report m_b values, then since the synthetic seismograms contain all the essential complications of the observations, we can use the theoretical time series to obtain m_b values accounting for these complications. Employing the observational definition of m_b throughout, individual station values at the appropriate distances and azimuths relative to the source may then be averaged to give a theoretical m_b for the event. The same procedure can be used to generate theoretical M_s values.

Using theoretical results such as those shown in Figures (4) through (9), we therefore can generate the required $m_b - M_s$ results for a variety of seismic events at various depths. Figure (10) shows $m_b - M_s$ results for dip-slip earthquakes, with fault length and stress drop variable while the rupture velocity and hypocentral depths are held constant for all events. Thus the lines labeled .01 k bar to 1 k bar are the $m_b - M_s$ loci of events of variable dimension and fixed stress drop, while the second set of lines define loci of events with fixed dimension but with variable stress drop. These curves obviously define a coordinate grid in the $m_b - M_s$ plane which can be used to interpret m_b and M_s values in terms of rupture dimension and stress drop. Such theoretical results can of course be generated for different event types, at different depths and with a different (fixed) value of rupture velocity if necessary. This set of theoretical results then provides the framework for the interpretation of $m_b - M_s$ observations in terms of stress drop and failure zone dimension. Further, if we assume that the largest stress drops observed for a region are "total" stress drops, corresponding to

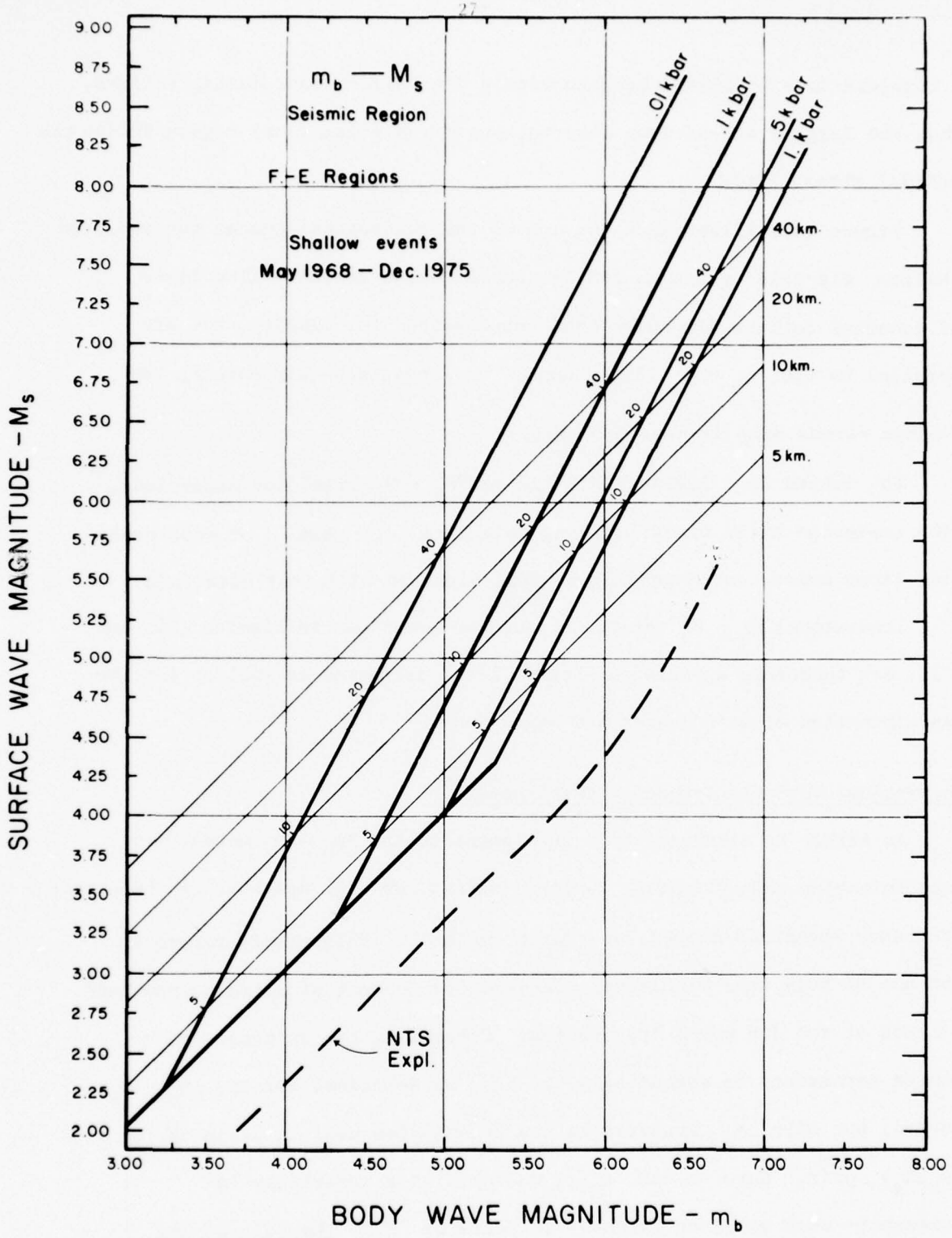

Figure 10: Theoretical m_b-M_s curves for dip-slip earthquakes at 10 km depths all with the same rupture velocity $v_R = .9v_s$, but having variable maximum dimension and stress drop.

a complete loss of shear strength within the failure zone during failure, then the largest stress drop observations for a given local region define the initial stress field.

Figure (11) illustrates the use of the theoretical curves for observed shallow, dip-slip events in the Alaskan-Aleutian region. (The lines of constant failure dimension have been omitted for clarity, but are parallel to the $m_b = M_s$ line shown.) For these dip-slip events, the average stress drop is near 100 bars.

The dotted line labeled "NTS" is an "$m_b - M_s$ line" for explosions, with explosion yield variable along this line. (A set of such explosion lines exist, corresponding to explosions in different materials.)

Theoretical $m_b - M_s$ relations, such as are shown in Figures (10) and (11), are therefore a basis for stress level estimates as well as for the discrimination of earthquakes and explosions.

Theoretical Variable Frequqncy Magnitudes.

As either an alternate or a supplement to the "$m_b - M_s$ method" for discrimination and estimating tectonic stress, we will use what can be termed a variable frequency magnitude method, or "$m_b(f)$ method". This simply refers to the use of body wave magnitudes measured from output of ultra narrow band filters at two (or more) frequencies. Otherwise, the inference of source parameters is essentially the same as described for the $m_b - M_s$ method, but with m_b measured at two frequencies used in place of the (m_b, M_s) pair. Here we use $m_b(f)$ measured at a moderately low frequency--such as .1 or .2 cps-- in place of M_s. The role of the traditional m_b measurement is replaced by $m_b(f)$ measured at a high frequency--in the range 1.0 to 3.0 cps. usually.

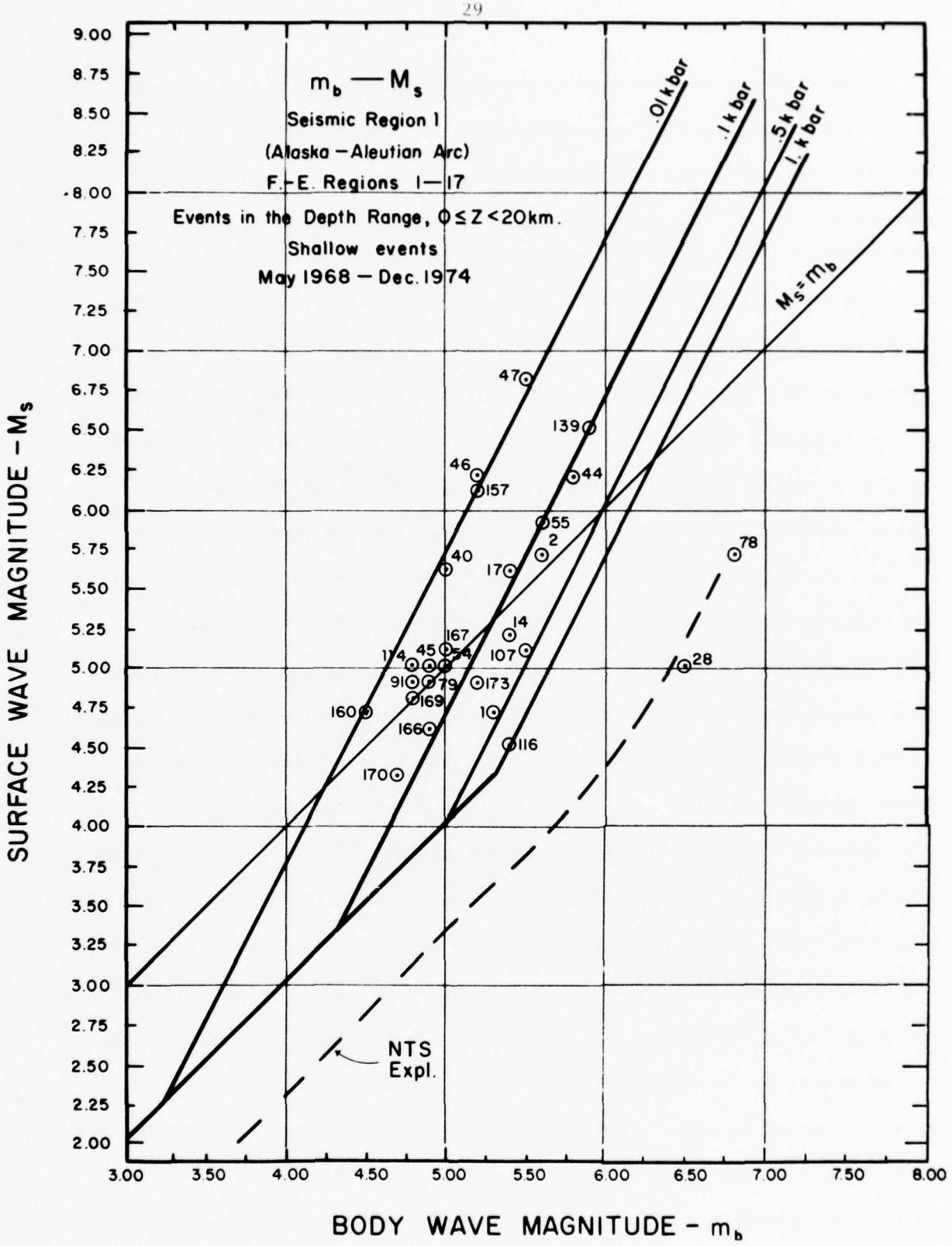

Figure 11: Theoretical and observed m_b-M_s data for Alaskan-Aleutian Arc region earthquakes in the depth range from 0 to 20 km. The curves shown on the figure are parameterized with respect to the stress drop with the rupture dimension variable along each of the curves.

This approach was designed by Archambeau et al. (1974) as a means of discriminating shallow earthquakes from explosions and has been applied extensively for this purpose. Savino and Archambeau (1976), Archambeau (1975b), Bache et al. (1975) and Cherry et al. (1974b), show numerous examples of the generation and use of $m_b(f)$ data.

Figure (12) shows an example of the narrow band filtering applied to an observed explosion and an earthquake. We observe that peaks in the narrow band filter output can be correlated in time with the onset of the original compressional wave signal. The amplitudes of these time correlated peaks in the filter output may be used to compute the $m_b(f)$ values, and give magnitudes to be associated with the frequency defined by the center frequency of the filter. Use of narrow band filter output amplitude data (as compared to spectral amplitudes from the complete Fourier spectrum analysis of the entire compressional wave train) is therefore advantageous in that time information is retained in the filter output, so that the amplitude measured can be related to a particular transient signal arrival. (This is not the case for a Fourier analysis of a large time segment containing several transient signals.) While the time information is retained, the amplitude measurement can still be related to a parti ular frequency component of the signal. Here, of course, there is a "trade-off" between time and frequency resolution, which may be stated as $\Delta f \Delta t > 1$, where Δt is the uncertainty in the time of the frequency arrival (arrival tin of the energy at the frequency f) and with Δf the uncertainty in the frequency determination. Nevertheless we can allow Δf for each amplitude estimate to be finite (it is proportional to the filter width at the half power points) and still obtain a very good estimate of spectral

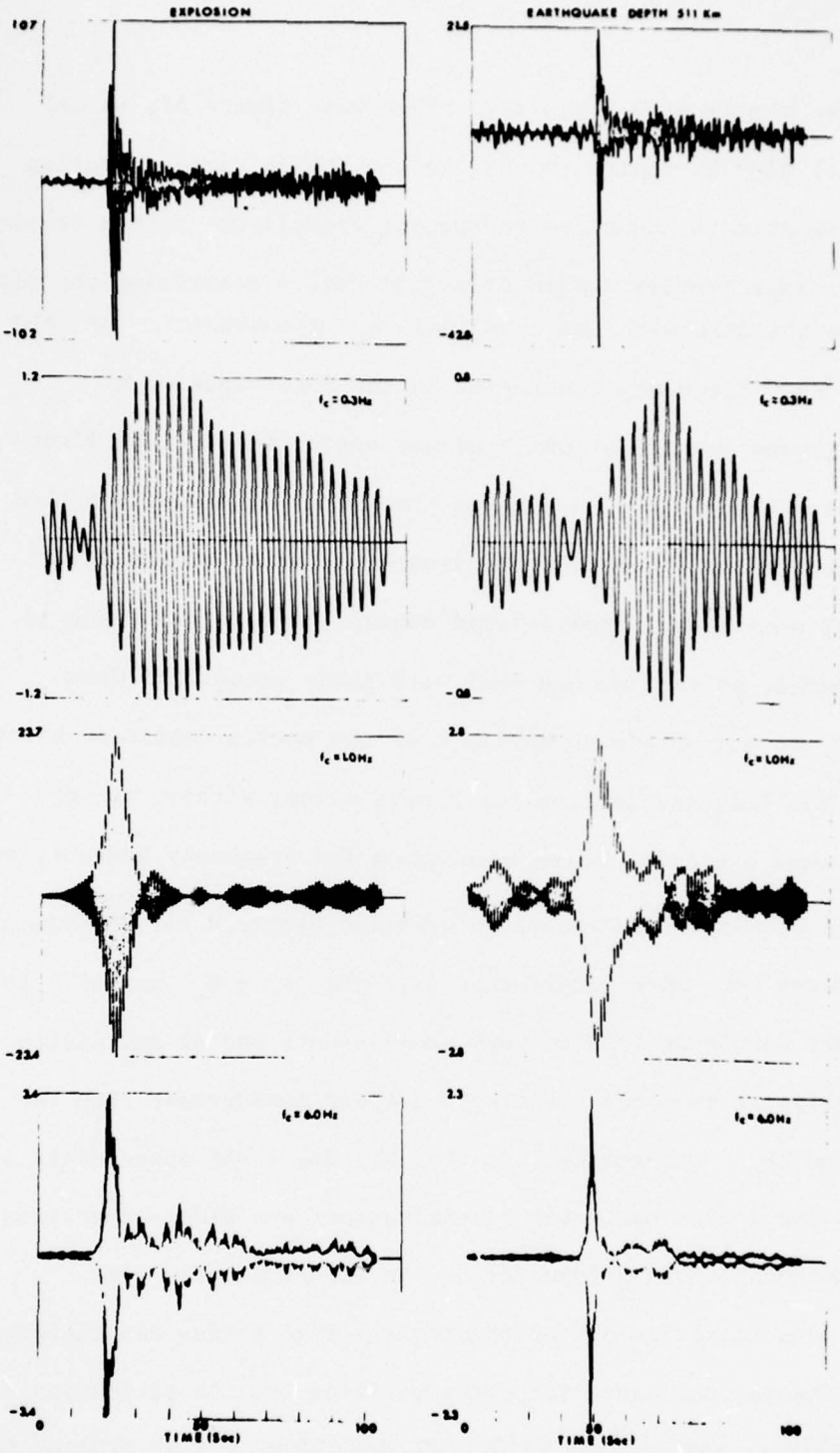

Figure 12: Application of a "comb" of narrow band filters to seismic events to obtain spectral amplitudes and time of energy arrival for several frequencies in the seismic band. An explosion and deep earthquake are illustrated. The amplitudes obtained are used to compute variable frequency magnitudes $\overline{m}_b(f)$ for P waves.

changes in the signal with frequency. Then with finite Δf, we see that Δt will also be finite so that we can retain time resolution and thereby be able to associate the measured amplitude with a particular part of the rather complex series of signal pulses comprising the wave train, as was the case with the classical m_b measurement. By this process, we "buy" frequency resolution in the determination of compressional wave magnitudes which we may associate with the first arriving P wave transient. In essence then, this is a simple method of obtaining spectral amplitude (or magnitude) estimates of the direct compressional wave signal from seismic events and a method which is easily automated, so that we may deal with large amounts of data. Consequently, we may obtain an estimate of the source amplitude spectrum at high and low frequencies from the P wave alone, without use of the surface wave magnitude measurement as a low frequency measure, and therefore can obtain the essential information required for discrimination and stress estimates much more simply than with the $m_b - M_s$ method. Further, this procedure can be applied to very small events and at any distance range. Finally, it is a more precisely defined measurement than the usual m_b and M_s measurements, so that it offers the opportunity of greater precision in the source parameter determinations and wider separation of explosion-earthquake populations for use in discrimination work.

Narrow band filtering of the theoretical time series can therefore be used to define a theoretical basis for discrimination and the estimation of seismic event parameters. Clearly the filtering operations can be applied to either the body or surface wave signals to generate spectral magnitudes $m_b(f)$ and $M_s(f)$. From these results, a variety of theoretical $M_s(f)$ versus $m_b(f)$ relationships can be generated. These relations are defined in

a space in which seismic events are coordinate points determined by their $m_b(f)$ and $M_s(f)$ values, or $m_b(f)$ values at two (widely) separated frequencies.

Figure (13) shows a number of possibilities for one type of event at fixed depths in the earth. In this figure, spectral surface wave magnitudes at .05 cps for both Rayleigh ($\bar{M}_s^R$) and Love waves (M_s^L) have been plotted against $m_b(f)$ at 1.5 cps and 2.5 cps, (labeled $\bar{M}_b$ (1.5) and $\bar{M}_b$ (2.5) in the plots). Theoretically predicted loci for earthquakes of variable fault dimension, fixed stress drop (500 bars) and fixed rupture velocity are shown. In the first figure at the upper left, loci for events with 100 bar stress drops are also shown and indicates the typical change in position of the event loci in these planes when the stress drop changes. The general character of the loci are quite similar to the "$m_b - M_s$ lines" previously described and and illustrated in Figures (10) and (11).

In addition to theoretical earthquake lines shown in Figure (13), theoretical points for explosions are also shown. They appear in such a plot as extremely high stress drop earthquakes, when viewed in terms of the theoretical earthquake loci. The situation is again similar to that for the $m_b - M_s$ relations. It is obvious from these plots how these magnitude measurements may be used to discriminate explosions and earthquakes, since the two types of events fall into separate populations in these "spaces".

The lower set of four plots are of greatest interest for applications and shown the loci of events of variable dimension and fixed 500 bar stress drop in the $m_b(f)$ plane. Essentially parallel curves in this plane result from these same sized events with different

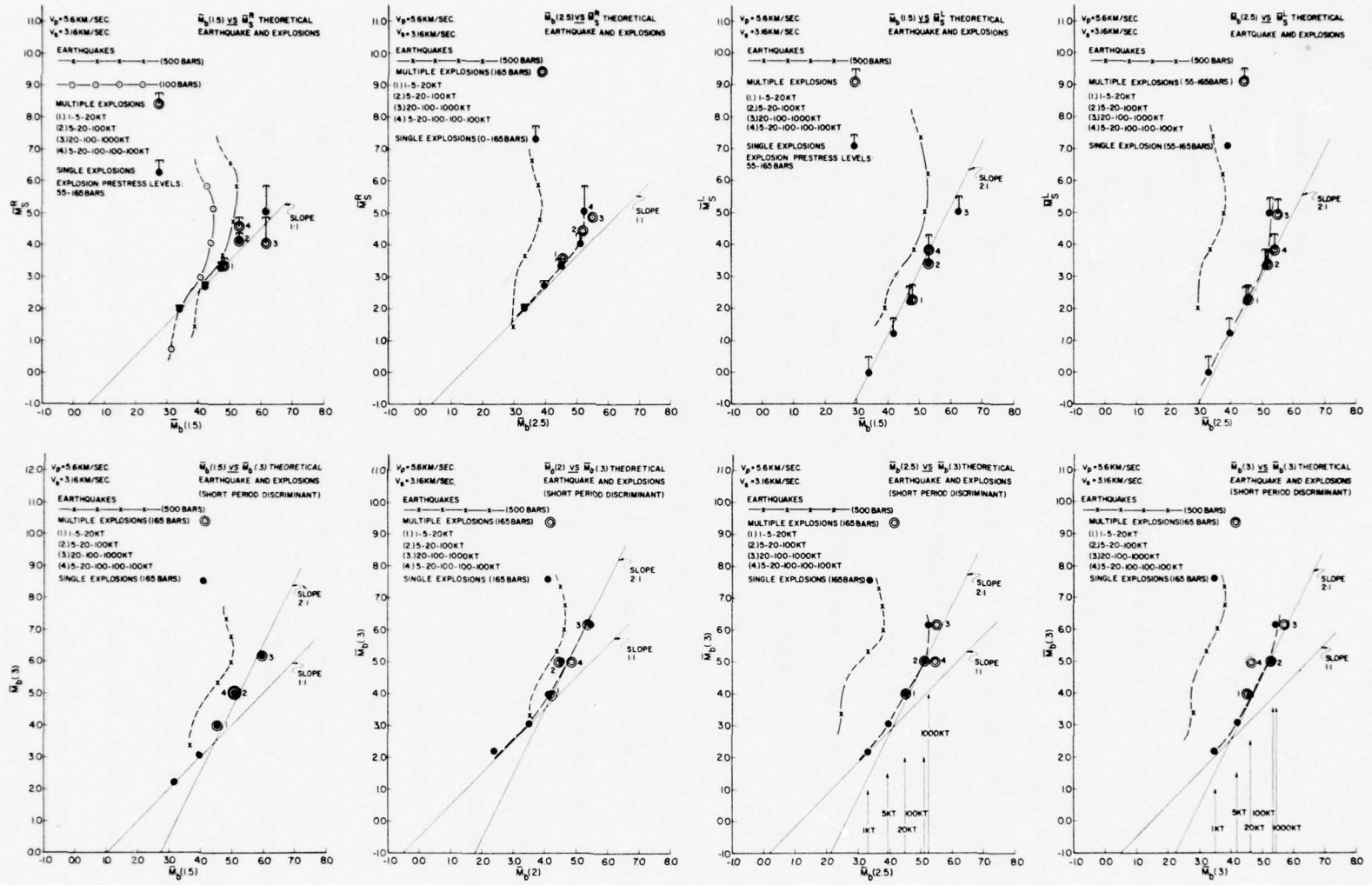

Figure 13: Theoretically predicted spectral body wave and surface wave magnitudes $\bar{m}_b(f)$ and $\bar{M}_s(f)$ for earthquakes and explosions illustrated by a series of plots of $\bar{m}_b$ vs $\bar{M}_s$ and $m_b(f_1)$ vs $m_b(f_2)$ with $f_2 > f_1$. The first plot, at the upper left, shows the typical variation of the $\bar{m}_b$ vs $\bar{M}_s$ curve for different prestress levels. Similar variations apply to all the plots.

stress drops. Those with higher stress drops lying to the right, closer to the explosion population, while those with lower stress drops define curves to the left. These stress variable "coordinate lines" are quite widely spaced and allow stress drop estimates to be obtained for all events down to those of very small size.

Essentially an unlimited number of such plots could be generated, since all possible frequencies can be used. However, they are to a large degree redundant in that only a few of them are needed to obtain the basic source property information sought--namely the stress level, the failure zone dimension and rupture velocity. If we assume that the rupture velocity is essentially the same for all the events to be observed, then this parameter is effectively eliminated from consideration and we need only one pair of variable frequency magnitudes to obtain the desired source properties. The magnitudes required are the largest low frequency $m_b(f)$ value, selected from several spanning the low frequency spectral range, and the spectral magnitude at the highest frequency that is well above the noise level. Because the spectrum is expected to be highly variable at high frequency, with numerous "peaks and holes", the high frequency magnitude value is to be obtained by using a straight line fit over several frequency separated estimates, so that a smoothed spectral value is obtained. In any case, these two magnitudes would normally correspond to spectral amplitude estimates on either side of the "corner frequency" the low frequency magnitude being obtained at the peak or flat spectral level (whichever occurs) and the high frequency estimate at a point on the rapidly decreasing high frequency spectral slope of the radiated

compressional wave spectrum from the source. For a fixed rupture velocity for all events, the spectral shape is invarient and then only these two values are needed to determine the stress and failure zone dimension.

In summary, these considerations show that the spectral magnitude estimates can be used with great flexibility in discrimination studies and to define source parameters. Further, in view of inherent redundancy, multiple estimates can provide several determinations of source parameters; with the variations in these estimates providing a check on the accuracy of the determinations. Similarly, more than a single discrimination criteria can be employed for identification of explosions from a set of events. Clearly this data can also be used to check the $m_b - M_s$ based soruce parameter estimates and discrimination as well as to extend the approach to the very numerous, small events. The latter capability is especially important for discrimination.

Finally and perhaps most important of all for the applications, is the fact that the $m_b(f)$ data is not strongly affected by source depth and source orientation since, in addition to weak or only moderate influence on individual spectral magnitudes, the magnitudes pairs at the two frequencies are both affected in the same way by source orientation and depth so that the effects essentially cancel out when the data is viewed in the "$m_b(f)$ plane" defined by a pair of spectral magnitudes. Thus, in addition to being only strongly influenced by the prestress and rupture dimension parameters so that more reliable and accurate estimates of these parameters are possible, this also means that it is not necessary to average over observations at different distances and azimuths and that single station observations can be used in either the near or far field distance ranges to effect discrimination of events and obtain source parameters estimates. It is therefore clear that the "$m_b(f)$ method" is by far the more flexible and accurate approach to general source studies, including discrimination.

IV. Signal Analysis for Discrimination and Stress Estimation.

This section is devoted to a description of seismic signal analysis methods and the operational signal analysis computer based on these methods. This program, specifically developed for seismic discrimination studies, is also directly applied in source parameter studies - in particular to stress estimation.

Depending upon the availability of one or more components of recorded ground motion (vertical and two orthogonal horizontal components) from seismic events, there are various types of filtering available in the signal analysis program. Since the majority of seismic stations operate with only a vertical component seismometer, the narrow band filtering operation to be described first will be most applicable for discrimination applications and for determination of earthquake source parameters based on spectral observations. Whenever three component data are available, both narrow band and polarization filtering techniques can be applied in order to isolate body phases for spectral computations and event location computations.

The central feature of the signal analysis program is the use of narrow band frequency filters to break up or decompose a time series consisting of signal plus noise into a set of quasi-harmonic modulated "signals". This set of filtered signals, one for each filter center frequency, can then be used to determine the energy arrival time (the group time, t_g) and amplitude of the signal for each center frequency by analysis of the time modulation of the filter outputs. Further, both the instantaneous phase and frequency of the individual filter outputs, that is the apparent phase and frequency of the quasi-harmonic filter output as a function of time, can be determined

quite simply. Thus, if two components of the same vector wave field are analyzed in this fasion, the difference in the instantaneous phase between the two components is a direct measure of the polarization of the wave field.

Thus, the decomposition of the signal wave train, possibly composed of many individual signal pulses, into quasi-harmonic signals provides the means of determining arrival time, amplitude and wave polarization, all as functions of frequency. This then is the basic signal information that can be used to detect a given type of signal in terms of its dispersion and polarization characteristics and to obtain its spectrum as well as its time and amplitude relation with respect to other signals present in a complex wave train.

Figures 14 and 15 are two different versions of the flow of operations in the existing computer program. Figure 14 provides a verbal outline, while Figure 15 summarizes the key mathematical operations performed in this program. More detailed developments of the theory and operation are given in Bache, et al. [1975b] and Savino, et al. [1975].

Seismic data are read into the program in the form of time series (Figures 14 and 15) generally of about 500-2000 points in length. The data are then optionally detrended, demeaned and tapered. The program then selects the smallest power of two which is greater than the number of points input and performs a discrete Fourier transform using the Cooley-Tukey [1965] algorithm. Both the original time series and the spectrum are then plotted.

Referring to Figures 14 and 15 , the signal is next filtered in the frequency domain by multiplication with a narrow band cusp-shaped filter. This particular filter form is selected to satisfy two goals: (1) minimum width in the frequency domain, and (2) maximum ripple suppression in the time

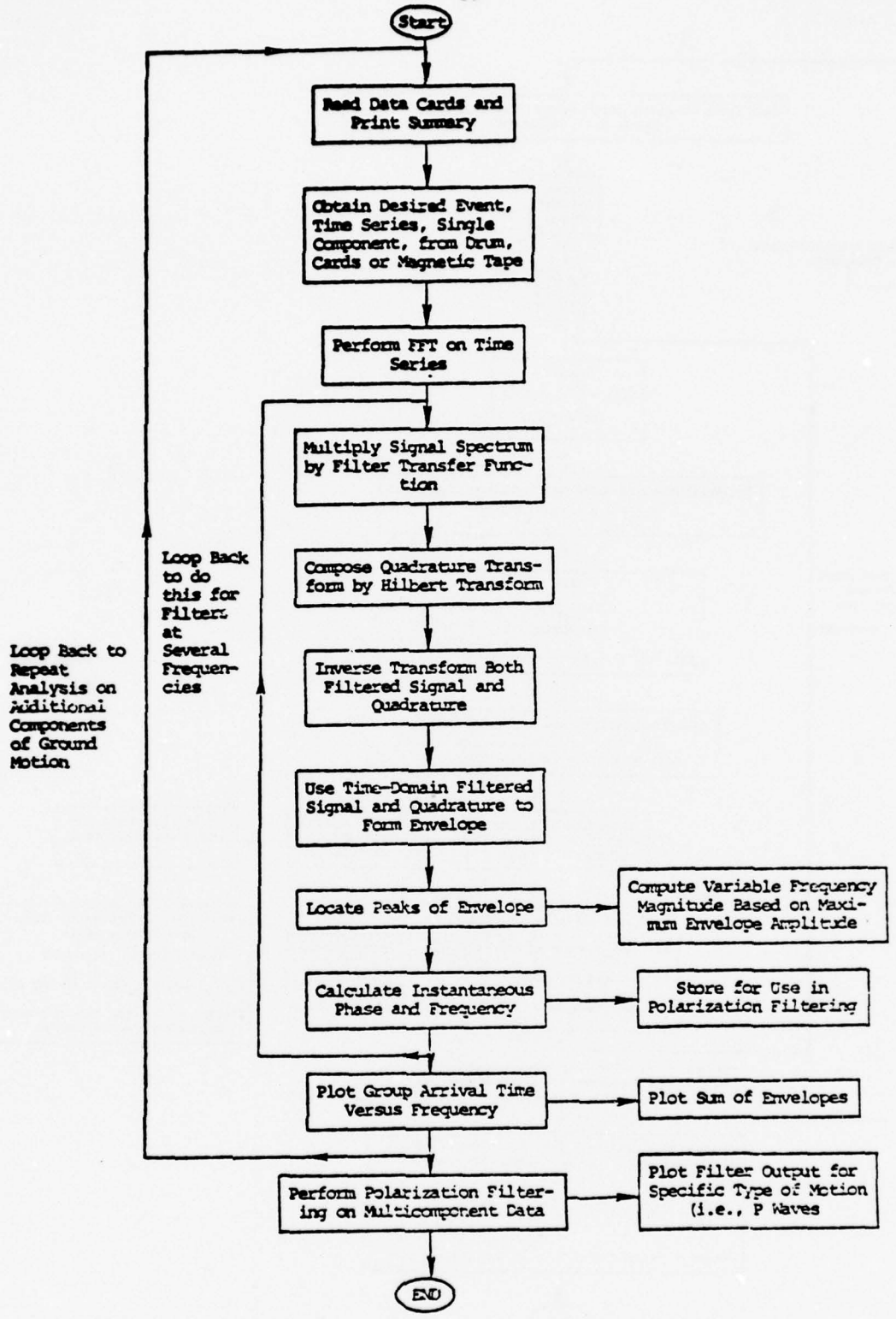

Figure 14 Signal Analysis Program Flowchart.

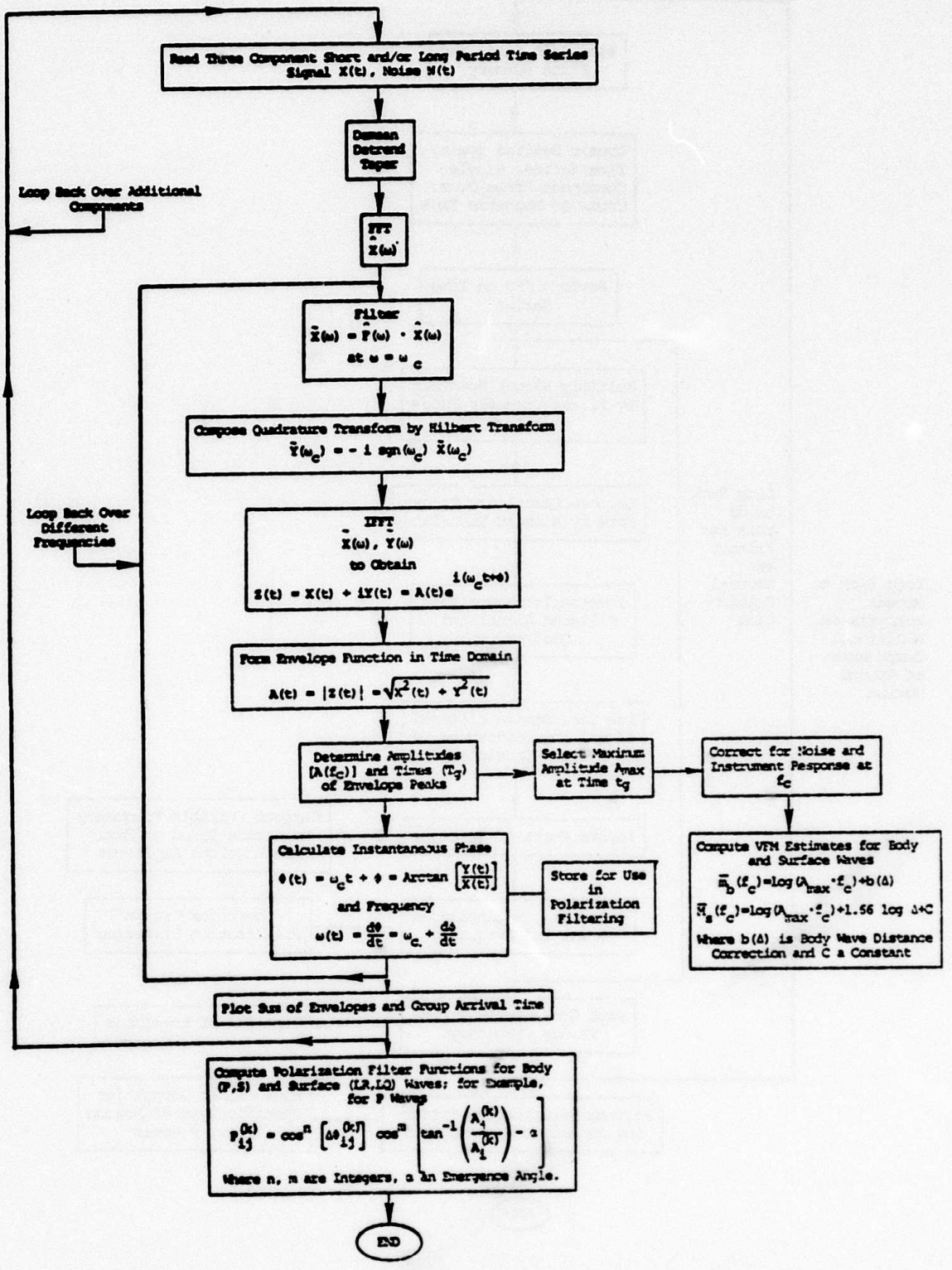

Figure 15 Flowchart indicating principal mathematical operations embodied in the signal analysis program.

domain. As a consequence of the sampling theorem, or uncertainty principle, one cannot simultaneously satisfy these two goals to arbitrary precision. The filter employed was selected for its optimal time and frequency domain characteristics within this basic limitation.

Once the signal has been narrow band filtered, it is corrected for the appropriate instrument response; the filtered signal transform is divided by the instrument transfer function. The resulting complex spectrum is then inverse Fourier transformed into the time domain, to produce what will hereafter be referred to as the filtered signal.

The narrow band filtered signal will appear as a quasi-sinusoidal carrier wave contained within a smooth envelope. The next step in the program (Figures 14 and 15) is to construct the envelope function by means of the Hilbert transform. In particular, a quadrature signal is formed by multiplying the transform of the filtered signal by $-i\ \mathrm{sgn}(\omega)$ and then inverting this to the time domain by an inverse transformation. The envelope function is then constructed by taking the square root of the sum of the squares of the filtered signal and its quadrature. The maximum of the envelope function occurs at the time of arrival of energy at the center frequency of the filter and the amplitude of the maximum is proportional to the spectral amplitude of the filtered signal at the center frequency of the filter. The instantaneous frequency and phase are computed from the filtered signal and its quadrature signal as well and are stored for subsequent use in polarization filtering with additional components of ground motion.

The narrow-band filtering procedure can be performed on a particular component seismogram at a number of different frequencies within some band of interest. Correlation of the resulting envelope functions indicates the

arrival times of the various frequency components.

The results of a close-in multiple explosion experiment can be used to desmontrate the ability of simple narrow band filtering to achieve a separation of distinct signal arrivals that overlap in time.

Specifically we use a vertical component recording from a surface explosion (Figure 16a) to simulate a multiple explosion scenario. This scenario is constructed to consist of a linear array of three equivalent yield events, equally spaced and detonated simultaneously. To simulate this explosion array we simply delay and sum the recording in Figure 16a. The delays are based on the spacings between shots, the propagation velocity assumed over this spacing and the azimuth to the recording station (here taken to be in line with the explosion array). The resulting composite seismogram is shown in Figure 16b and consists of three separate overlapping events, each consisting of a complex wave train.

Both the original and composite time series shown in Figures 16a and b were narrow band filtered with sixteen different filters with center frequencies varying from 25 cps up to 100 cps, since the basic data were digitally recorded at a rate of 500 samples/second.

Using the Hilbert transform procedure mentioned previously, envelope functions were constructed for each of the sixteen filtered outputs. The envelope functions at several frequencies are shown in Figure 16c and d for the original and composite signals, respectively. First we observe from this array of filter envelopes in Figure 16c that the original explosion has three separate arrivals, or phases, making up the signal wave train. Secondly, from Figure 16d we can see the triplication of each of these arrivals corresponding to the three explosions in the multiple event scenario.

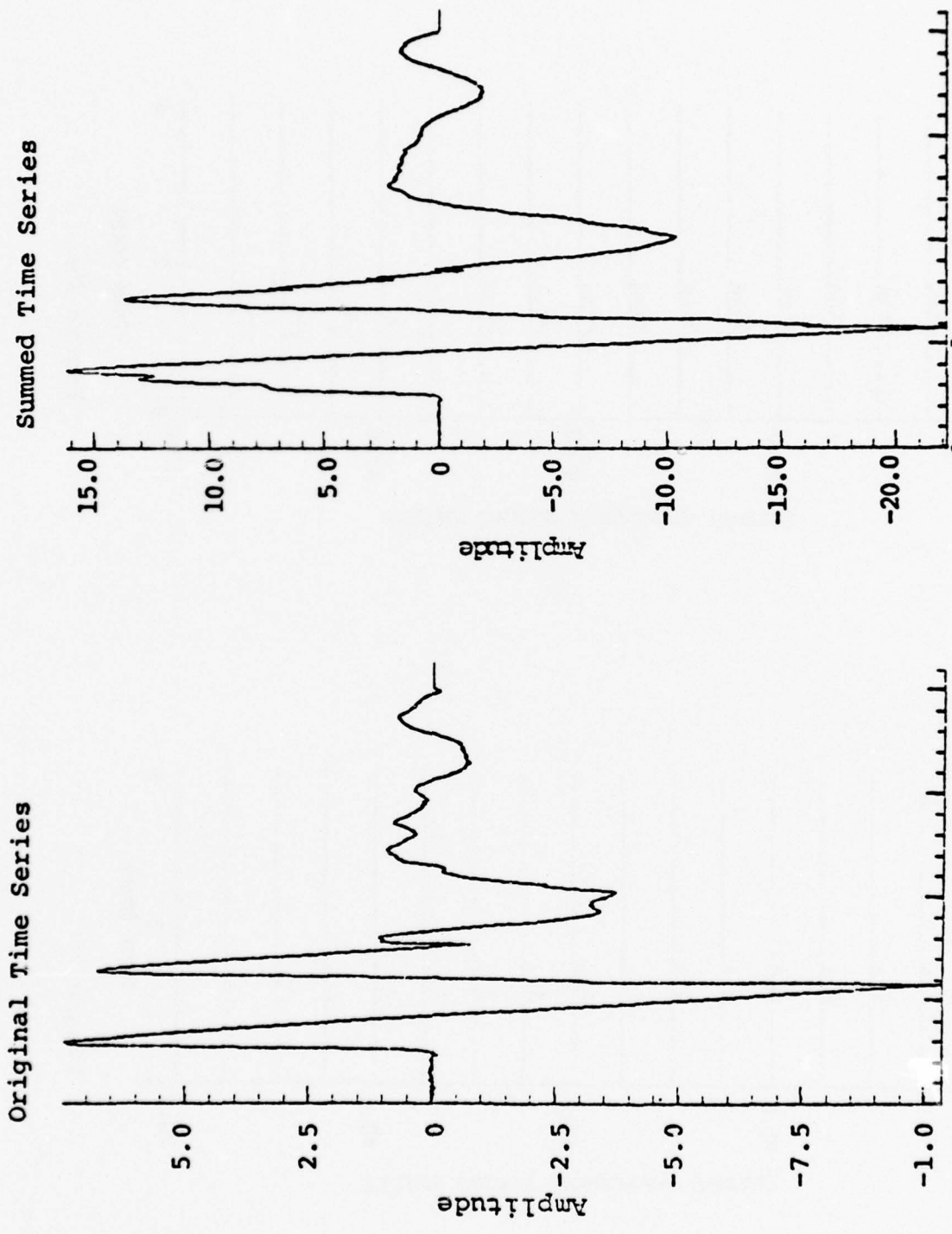

Figure 16a

Figure 16b

Filter Envelopes - Original Signal

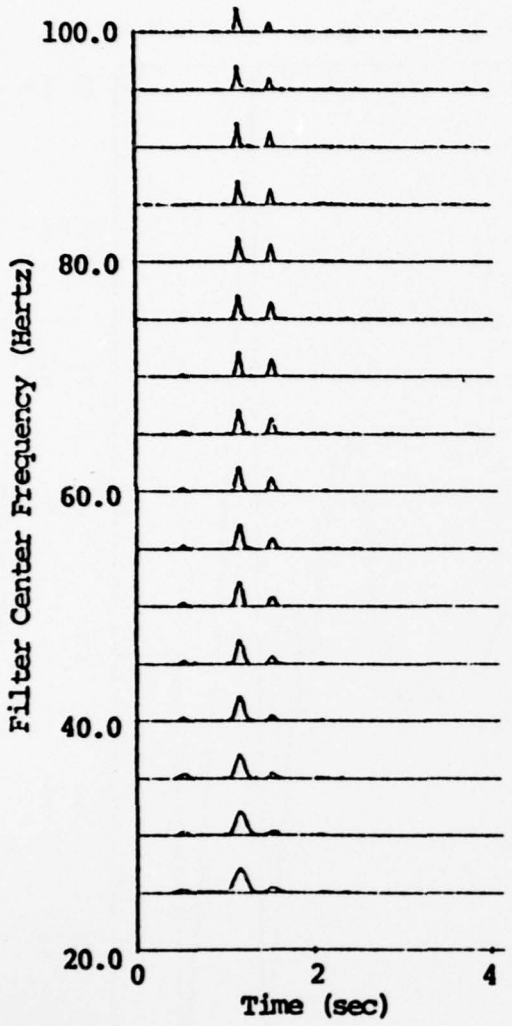

Figure 16c

Filter Envelopes - Composite Signal

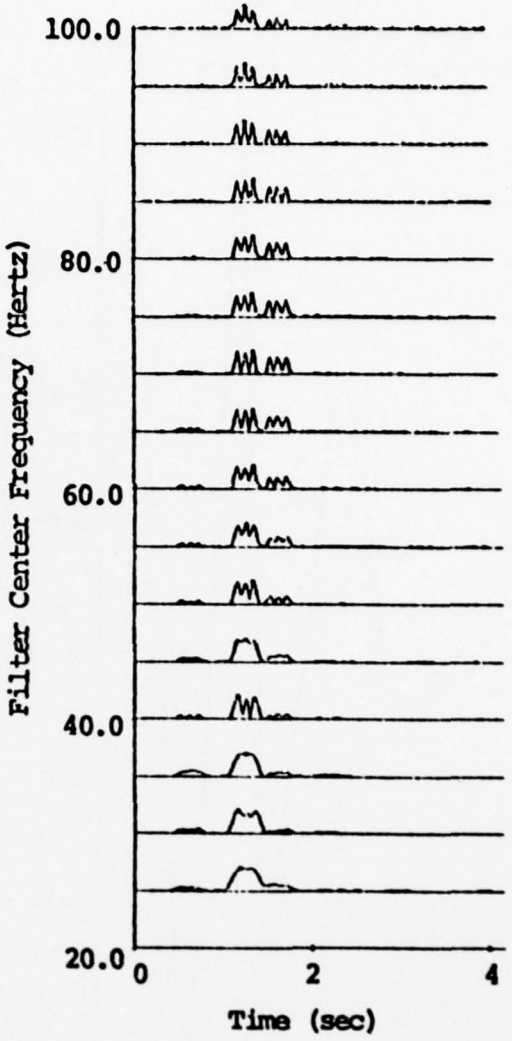

Figure 16d

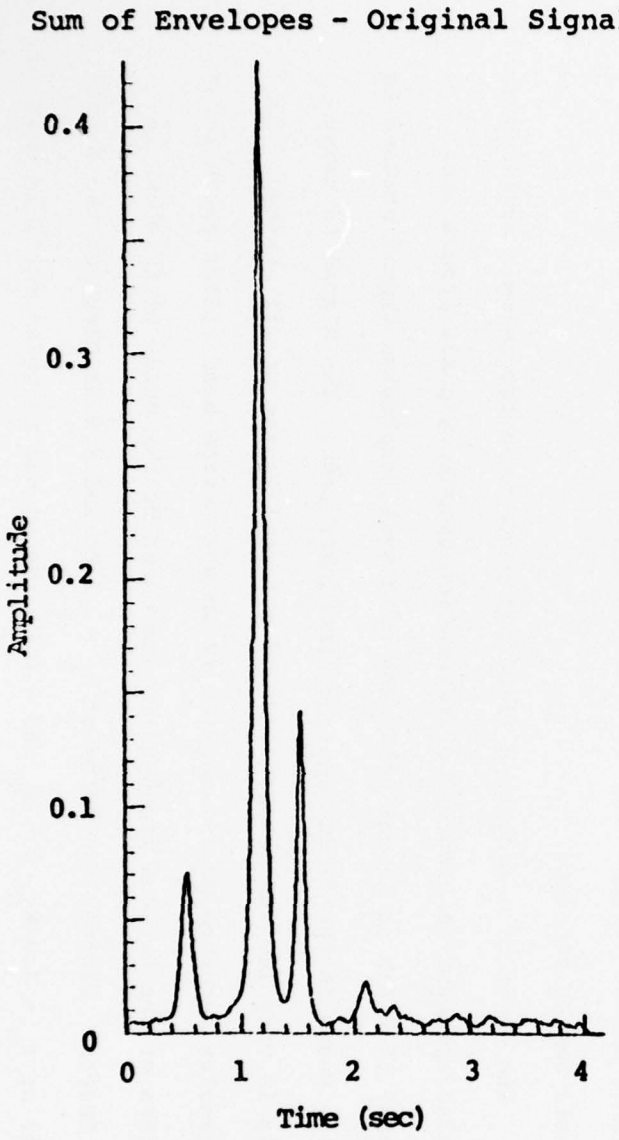

Figure 16e

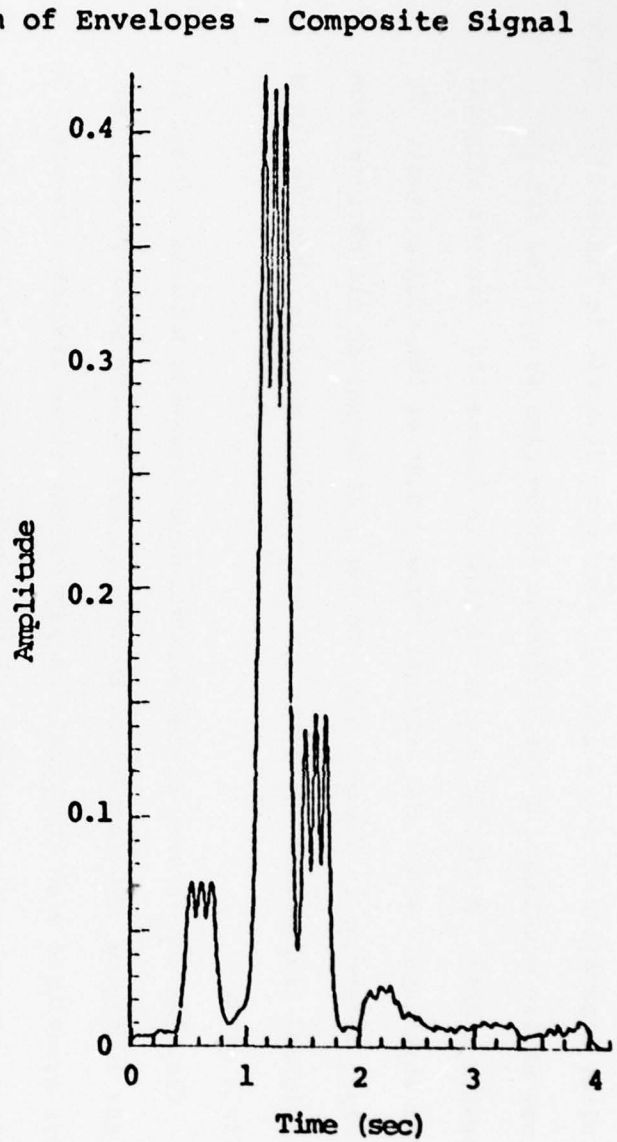

Figure 16f

The clear separation of the signals is even more dramatic in Figure 16f, where the sum of the envelopes at the different frequencies is plotted for the composite signal. A similar sum is plotted in Figure 16e for the original signal which again shows the original three phases of the single event. By contrast, referring to Figures 16a and 16b, it is not at all obvious from the original time series where the various arrivals occur or that 16b is a multiple event.

The time separations of the maximum power arrivals between 1.0 and 1.4 seconds in Figure 16f correspond as well as can be determined to the time delays associated with the equal spacings of the three simulated events. In addition, note that the amplitude of the composite signal in Figure 16b is more than twice the amplitude of the original signal in Figure 16a, but that each peak in the composite envelope sum is nearly equal to the peak for the original signal (Figure 16e). Hence the power in each of the three separate signals can be resolved.

The power of narrow band filtering procedures for seismic applications is also apparent in problems of separating seismic signals from noise. Figure 17 shows an actual recording of a small explosion signal emersed in noise, shown in the first figure at the upper left. The signal to noise ratio is very low and the presence of a signal is not at all obvious. The successive sequence of time series shown are narrow band filter outputs for filters at the various frequencies indicated by the value of f_c shown in the insets. Clearly the noise at f_c = .3 Hz and 1.0 Hz obscures the signal, while at f_c = 3.0 H_z, 4.5 H_z and 6.0 H_z the signal to noise ratio is near 10. This shows that for seismic signals and noise, narrow band filtering at high frequencies can be very effective for signal detection, isolation and

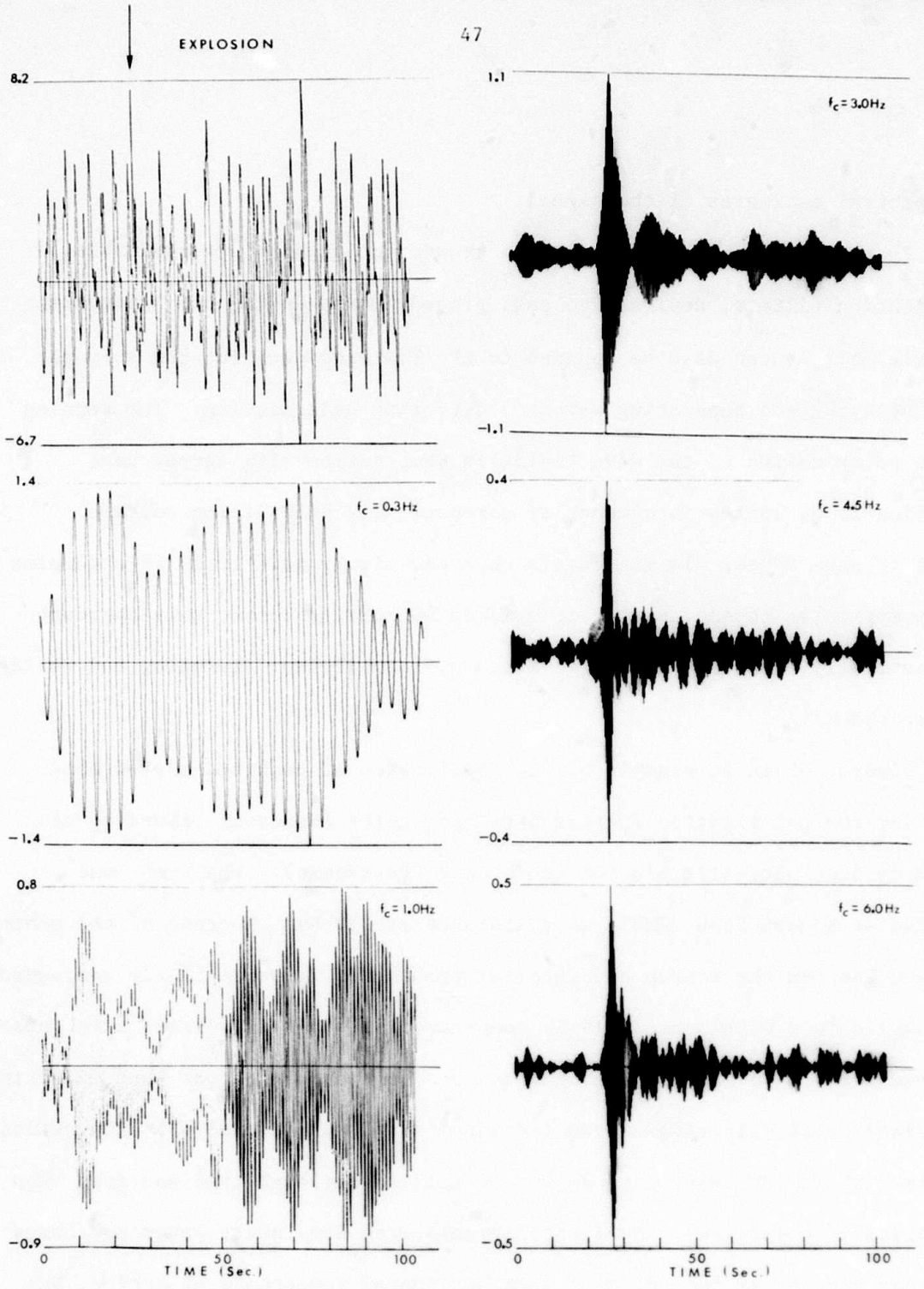

Figure 17: Examples of increasing signal-to-noise ratio for a presumed explosion (top left frame) recorded at Norway with successive application of high frequency narrow-band filters. Arrow at top denotes approximate arrival times of the P-wave on the unfiltered trace.

for spectral estimates of the signal.

In the event that multicomponent ground motion data are available, polarization filters, designed to pass ground motion having the appropriate particle motion, can also be applied to the filtered data for the purpose of identifying and separating waves of differing polarization. The sensing of the polarization of the wave field, in combination with narrow band filtering is an appropriate means of automatically identifying seismic phases or wave types. In many cases when the signal wave train is a complex superposition of phases emersed in seismic background noise, this approach is practically the only systematic means of identifying, isolating and timing seismic phases.

Figure 18 is an example of the application of combined narrow band filtering and polarization filtering using a three component recording of an underground nuclear explosion (code name Chartreuse). The event was recorded at Kanab, Utah (KNUT) at a distance of 312 km. Because of the short distance between the source and receiver the record is particularly compacted and complicated, with many arrivals compressed into a fairly brief time interval. The traces (B), (C) and (D) are examples of the combined narrow band filtering and polarization filtering at two frequencies. Compressional (P) and vertically polarized shear (SV) waves are shown, as well as Rayleigh type surface waves (elliptically polarized). Horizontally polarized body shear waves and Love waves can also be extracted using both horizontal components of motion, but are not shown here. The arrival times predicted on the basis of tabulations appropriate to the path (Gutenberg, 1944; Evernden, 1967; Herrin, 1968) are indicated on the filtered traces. There it should be noted that the filtering corresponds to "zero phase shift" filtering and consequently the body phase

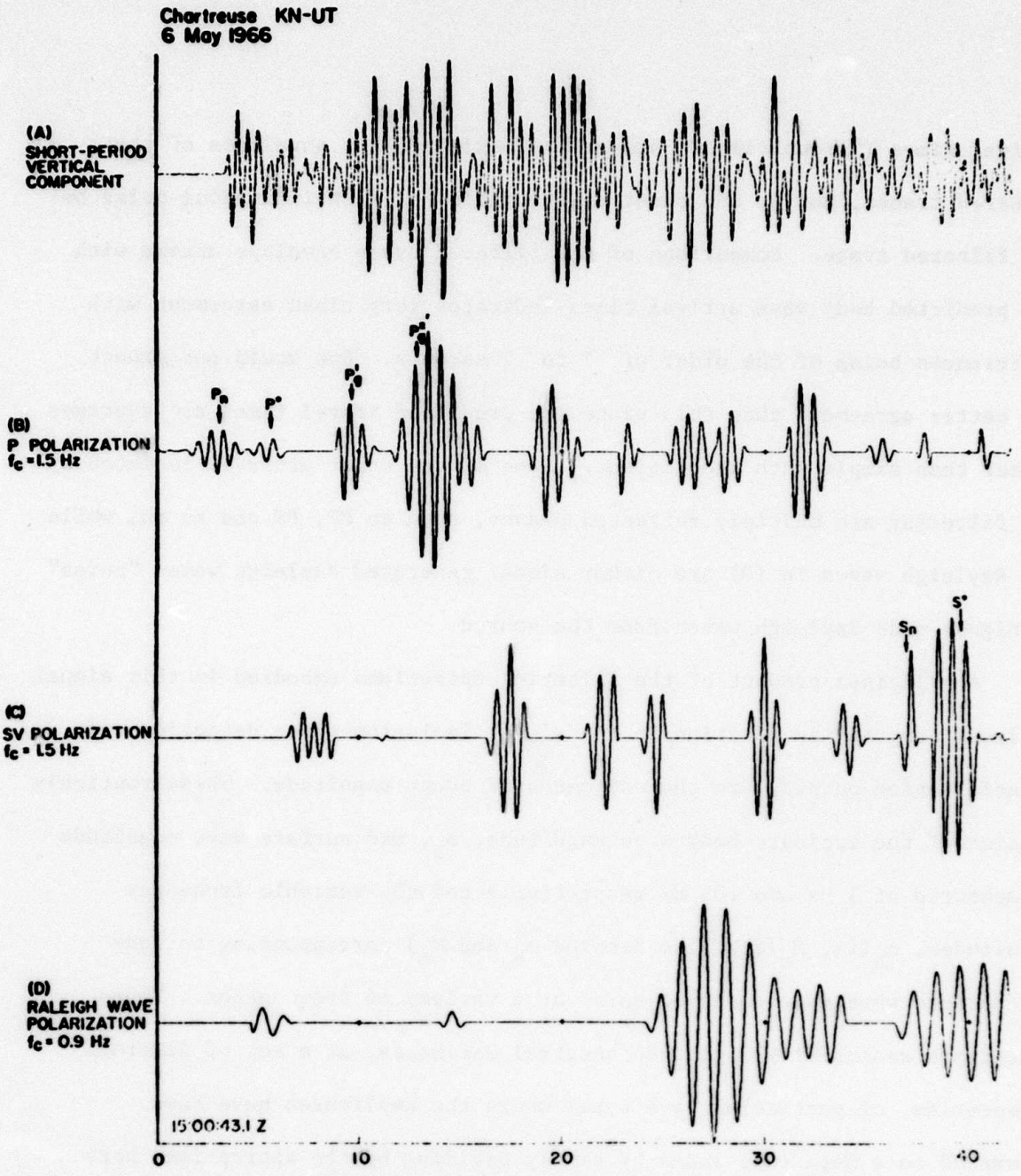

Figure 18 Polarization filtering of Chartreuse-KNUT record (Δ = 312 km) where indicated phase arrivals are predicted times for body phases.

arrival times ("group times") are at the maxima of the envelopes of the filtered traces, not at the onset of the motion of each individual pulse on the filtered trace. Comparison of the filtered trace envelope maxima with the predicted body wave arrival times indicates very close agreement with differences being of the order of .1 to .7 seconds. One would not expect any better agreement than this since the predicted travel times are averages rather than simple path predictions. Some of the other arrivals isolated by the filtering are multiply reflected phases, such as PP, PS and so on, while the Rayleigh waves in (D) are either signal generated Rayleigh wave "noise" or higher mode Rayleigh waves from the source.

A principal product of the filtering operations embodied in this signal analysis program, in addition to the signal isolation-phase detection and identification output, are the estimates of event magnitude. These routinely consist of the ordinary body wave magnitude, m_b, and surface wave magnitude M_s measured at 1 Hz and .05 Hz respectively and the variable frequency magnitudes, $m_b(f)$, $M_s(f)$ (also denoted $\overline{m}_b$ and $\overline{M}_s$) corresponding to body and surface wave magnitudes measured at a variety of frequencies. These latter are essentially amplitude spectral estimates, at a set of discreet frequencies, of particular wave types where the amplitudes have been converted to a magnitude index by simply dividing by the appropriate period T (i.e., the center period of the narrow band filter) and taking the base ten logarithm of the result. In addition, a constant distance correction factor is often also applied to give magnitude indices for the event that are comparable with the usual m_b and M_s magnitudes.

Thus magnitudes may be computed at a variety of frequencies from the narrow band filter output and since we may also associate a group time or energy arrival time with each amplitude measurement, we can identify the wave

type with which the magnitude measurement is associated.

Figure 19 is an example of the application of the $m_b(f)$ data, generated from a large number of events, to the discrimination of earthquakes and explosions. The event data shown are only two of the frequency dependent magnitudes that characterize the events, but for the teleseismic distances (Δ = 60-70°) and the type of receiver (LASA seismic array) the two frequency dependent magnitudes at .45 and 2.25 Hz provide the best separation of the explosion-earthquake populations in the $m_b(f)$ parameter space.

The large scatter of the earthquake population in the $m_b(f)$ space is due to variability of the stress drop, rupture dimensions and rupture rate among the events. The earthquakes nearest the explosion population have the highest stress drop and rupture rate. The events with the largest $\bar{m}_b$ values have the largest failure zone dimensions.

Some of the scatter in the event populations for both the earthquakes and explosions is due to background seismic noise. This, of course, is relatively more important for events of small magnitude, since the signal power will be low relative to the noise power, and causes some mixing of the populations at the very low magnitudes. (The smallest explosions shown have conventional magnitudes, m_b, of about 4).

In view of the desirability of estimating noise properties and then correcting for noise contamination, the signal analysis program normally obtains noise spectral estimates and uses these to obtain unbiased estimates of the signal spectral magnitudes. (In this case, the average noise spectral amplitude at the appropriate frequency is subtracted from the signal spectral

amplitude.) The nature of the noise has been investigated for each of the events making up the event set shown in Figure 19 using the signal analysis program and it was found that noise time series, when viewed in an $m_b(f)$ plane such as that in Figure 19, occupies the same region as do the small magnitude earthquakes. This means that when the noise contaminates a small explosion signal, the result will be such as to make the explosion appear to be more earthquake-like and for low signal to noise ratios to actually move the explosion point into, or very near, the earthquake population. Further the noise contamination will move the earthquake points, but always within the earthquake population and not outside of it.

This is illustrated in Figure 20 where a number of the small events observed at LASA and shown in Figure 19 have been detected at a Norway array and processed and plotted in the $m_b(f)$ plane for f = .6 Hz and f = 5. Hz. Only the smaller magnitude events are shown in Figure 20. Again, in this plane, we observe convergence of the populations. The arrows on the smallest explosion data points indicate the direction in which a noise correction will move these points in this magnitude plane. Figure 21 shows the effect of the noise correction applied to <u>all</u> the events, including earthquakes as well as explosions. (In this figure only the log of the amplitude is plotted, the $\overline{m}_b$ plot would be identical except for a scale change.) It is evident that the explosion population is now well separated from the earthquake population. The arrows on the two small explosions, both with regular m_b magnitudes somewhat less than 4.0, indicate that it is likely that the unbiased estimate of the noise contamination is lower than that actually present and that the true event points are still lower in the direction indicated.

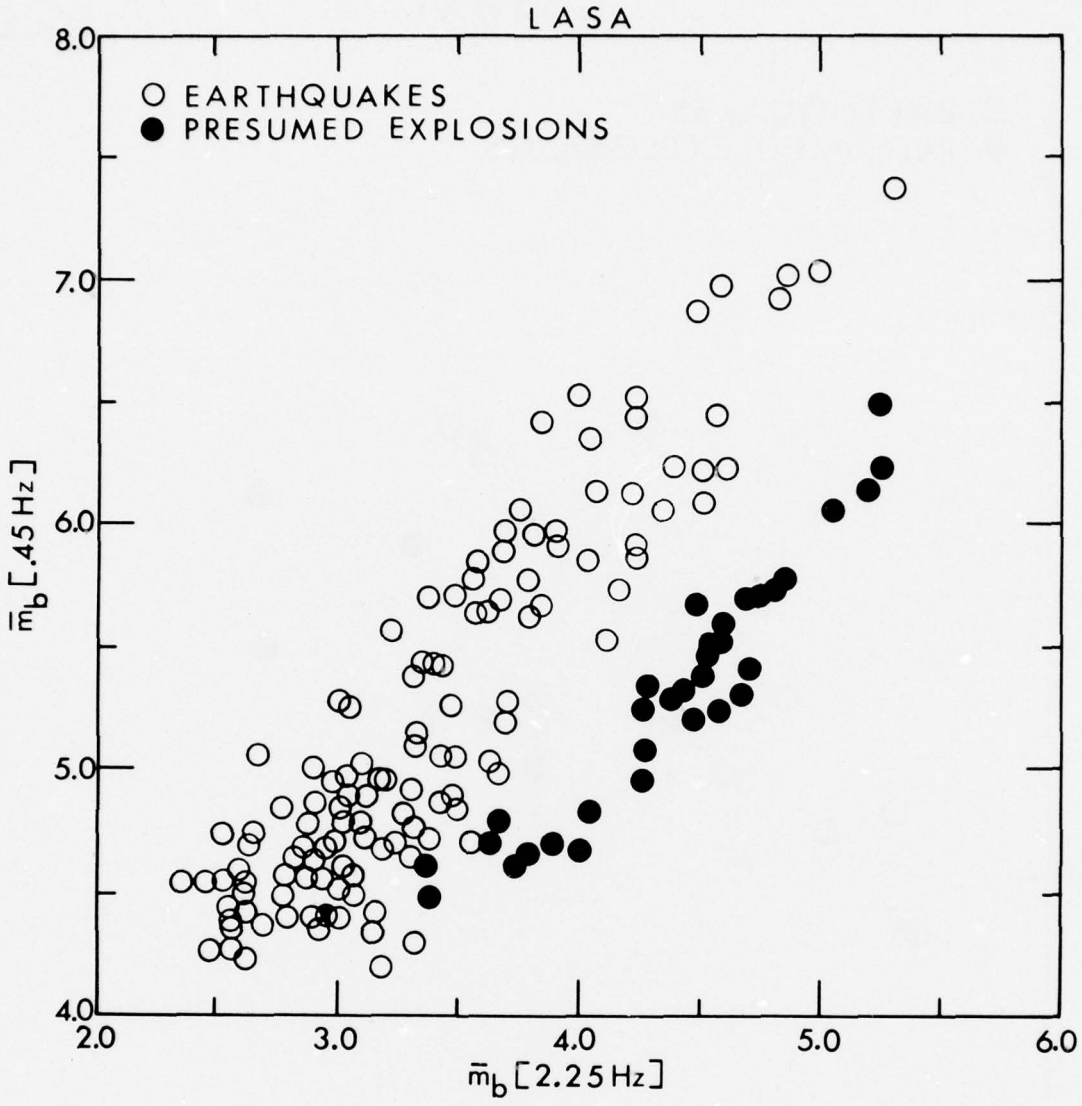

Figure 19: Spectral magnitudes, $\bar{m}_b$, computed at 0.45 Hz and 2.25 Hz.

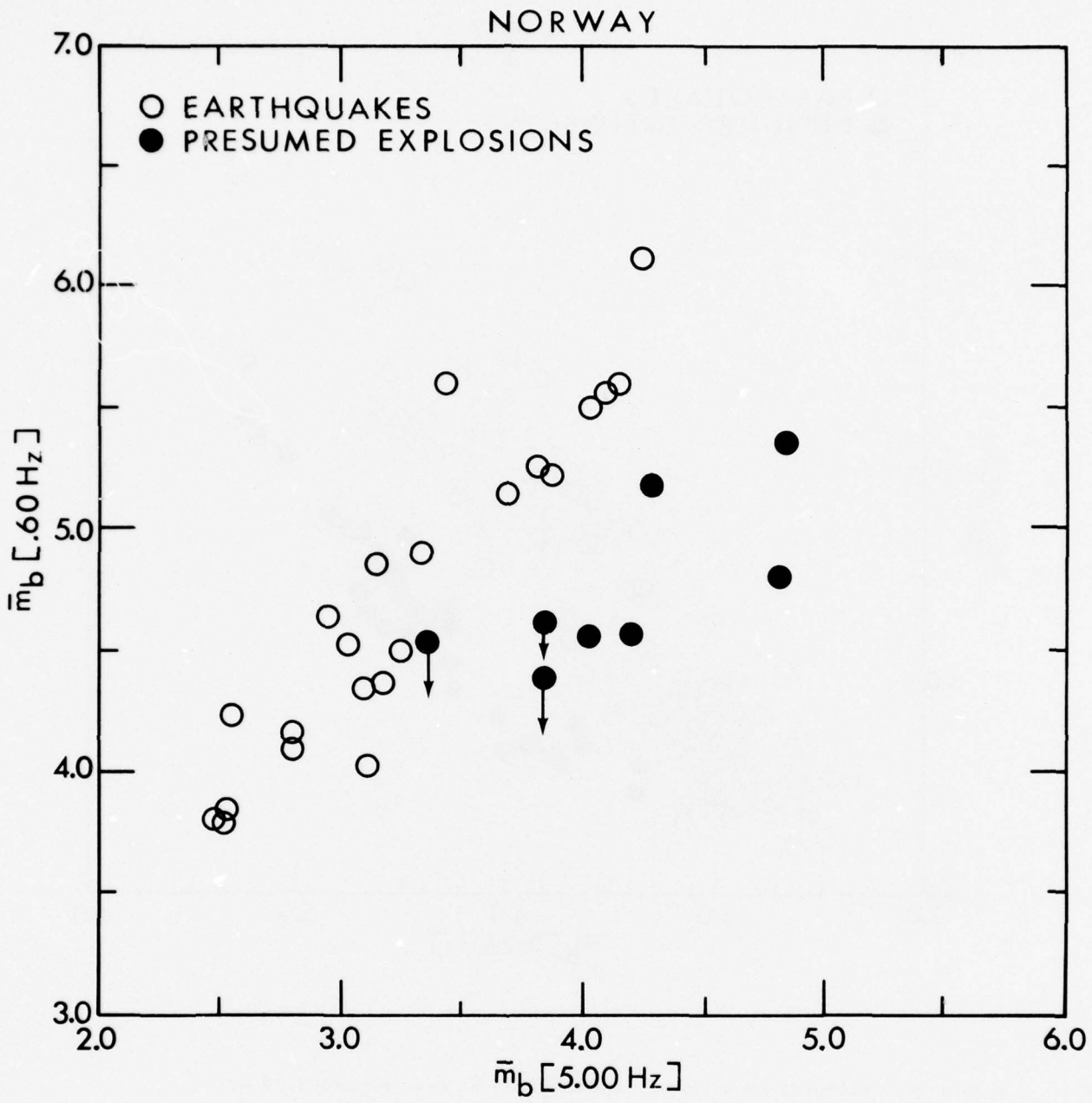

Figure 20: Spectral magnitude estimates at f_c = 0.6 Hz and f_c = 5.0 Hz for an event population recorded at the Oyer array in Norway.

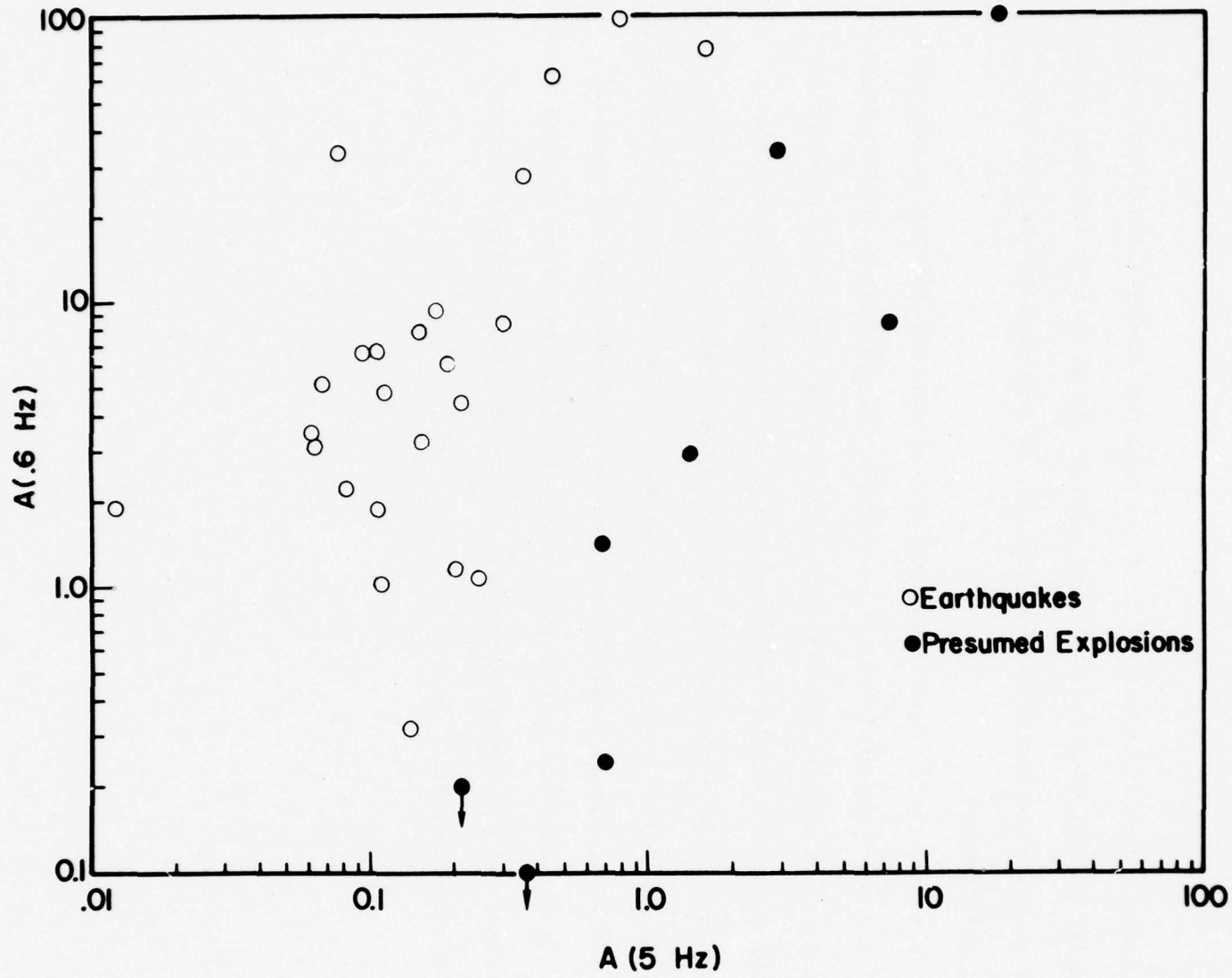

Figure 21: Maximum filter amplitudes with noise correction for the same event population plotted in Figure 20.

In any case, it is evident that the combined signal and noise analysis capability is important for the correction of signal data in order to obtain better estimates of source characteristics, as expressed by the observed signal information.

In total, the current signal analysis program constitutes an extremely useful and quite powerful tool to be used for the detection, identification and analysis of seismic signals. The output of this processor provides not only the required data for explosion-earthquake discrimination but also quantitative noise corrected data for analytically based determinations of source and medium properties, such as stress drop and rupture dimensions of earthquakes, energy yields for explosions and travel times and spectral amplitudes of body and surface waves for medium studies. Thus it constitutes a low cost, rapid, automated procedure for the detailed analysis of very large event data sets.

V. Stress Estimates Along the North Pacific Circumference.

Observational $m_b - M_s$ data has been used to infer stress levels in the Alaskan-Aleutian and Japan-Kuriles-Kamchatka regions using the "$m_b - M_s$ approach discussed in the previous sections. Figure 22 shows all the data available for the Alaskan region, plotted against theoretical curves for dip-slip events in the 0 - 20 km depth range. Only some of this shallow event data can be interpreted in terms of the theoretical curves shown of course, but the curves do indicate the stress range for the variety of events in the depth range from 0 to 50 km.

Similar data for the California-Nevada region is shown in Figure (23). Clearly, the amount of available data for this region is less than that for the very active Alaska-Aleutian region. Consequently, for stress estimates, the present data that we have must be supplemented by additional observations.

Figure (24) shows the currently available data for the Japan region, plotted in the same manner as the data for the other regions. This region is the most active in the world and provides an indication of the maximum amount of $m_b - M_s$ data that can be obtained over a five to six year period from the U.S.G.S. compilations. The data for the Japan and Alaskan regions are sufficient for an application of the approach outlined in our earlier discussions.

At this point it is evident that we can obtain stress drops and fault dimensions by direct comparison of theoretical predictions with the data, as indicated in Figures (22) to (24). The data must however be separated into groups, corresponding to activity in particular depth zones for earthquakes of a particular type, with these event subsets interpreted using comparable theoretical results.

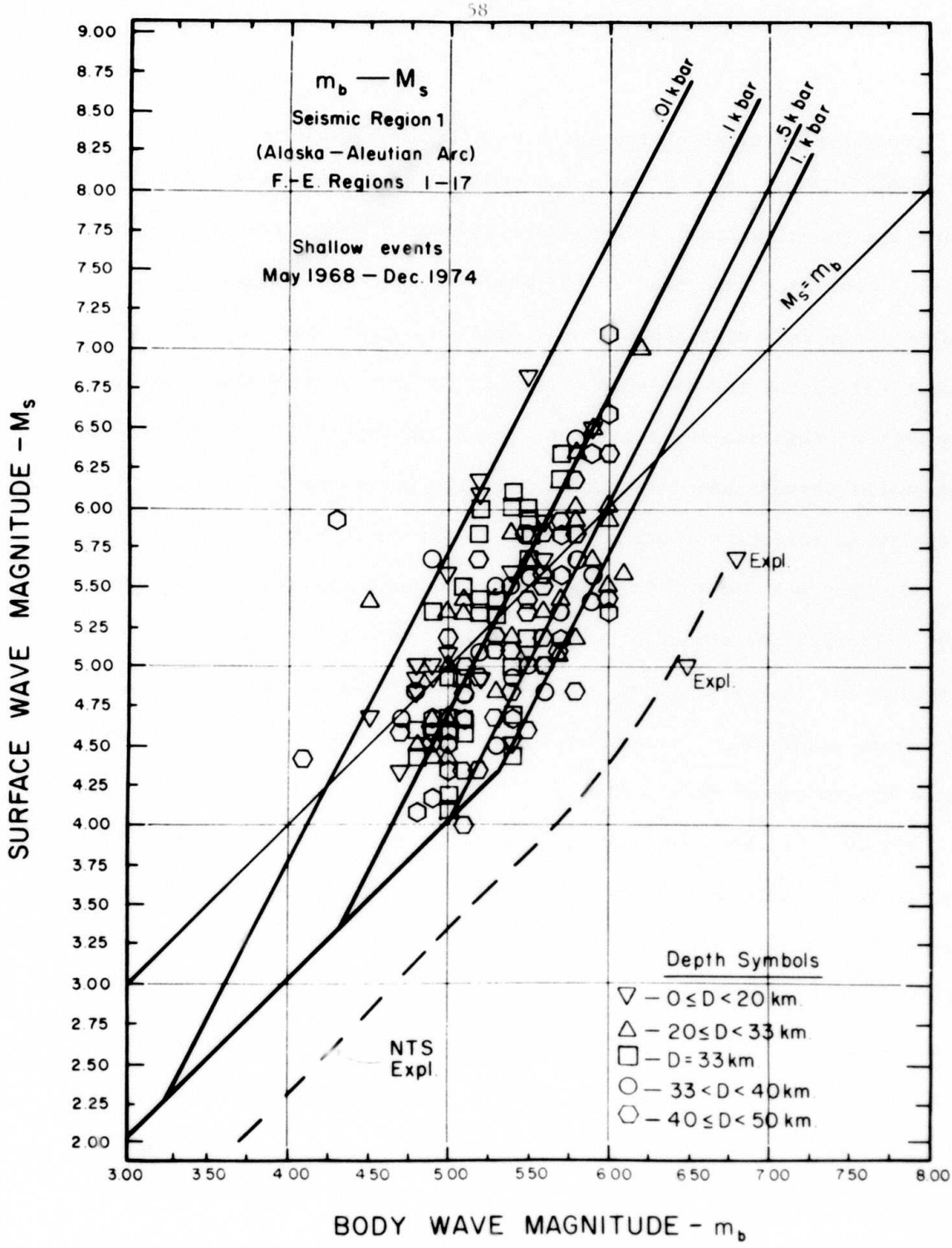

Figure 22: Observed m_b-M_s data for the Alaska-Aleutian Arc Seismic Region shown with theoretical m_b-M_s curves with prestress as a parameter for the curves and fault length variable along each curve. Theoretical curves and data are for dip slip and thrust events.

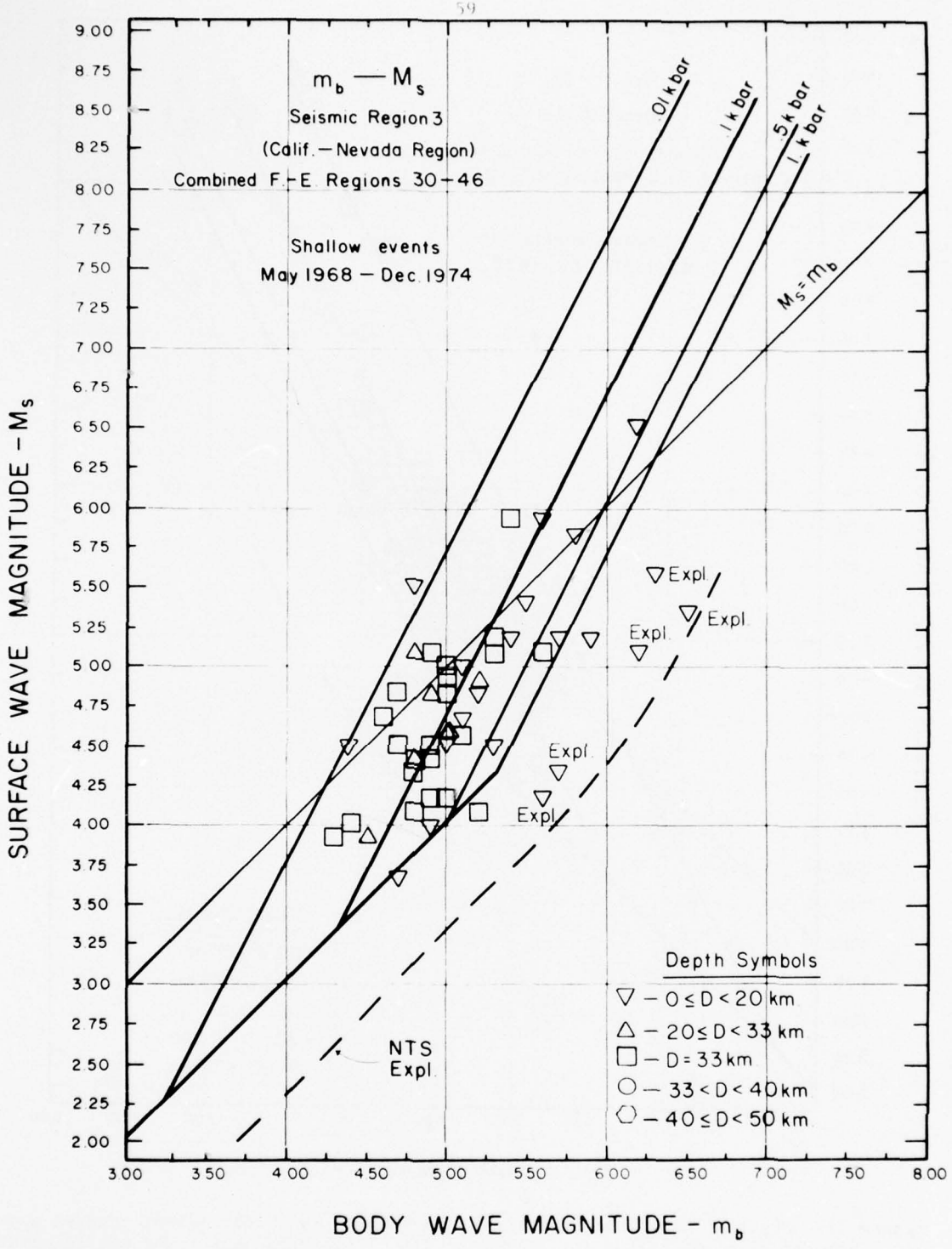

Figure 23: Observed m_b-M_s data for the California Nevada seismic region shown with theoretical m_b-M_s curves for thrust and dip slip type earthquakes.

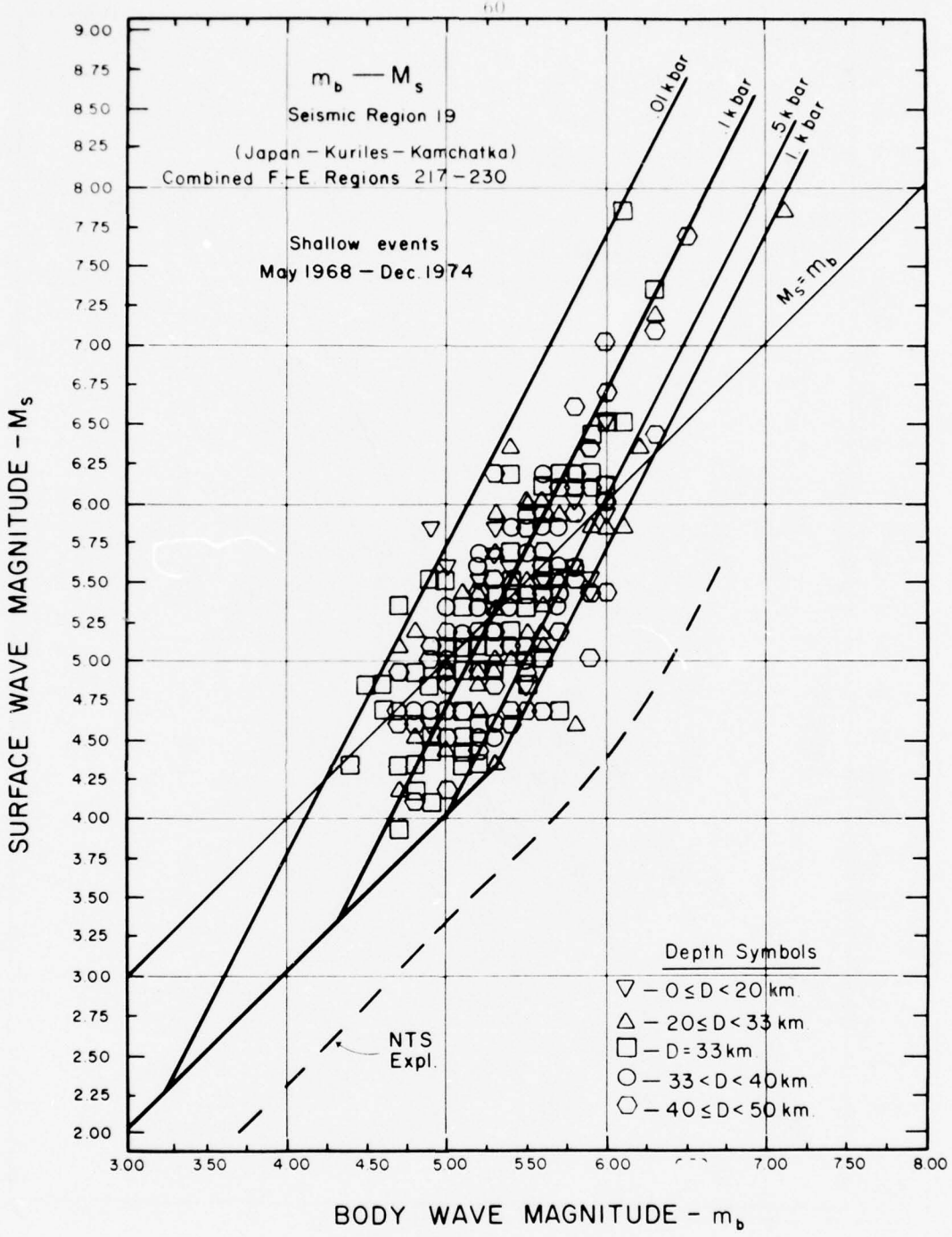

Figure 24: Observed m_b-M_s data for the Japan-Kuriles-Kamchatka seismic region shown with theoretical m_b-M_s curves for thrust or dip slip earthquakes. The events observed are essentially all thrust or dip slip type. The mean stress drop for the population is somewhat larger than 100 bars within any events having stress drops near 1 kilobar.

If we assume that melting occurs during or as a consequence of failure within the rupture zone, then the stress drop is in fact equivalent to the recoverable ambient stress level. We need not make this assumption however in that we can use the largest stress drop events to provide the estimate of the ambient stress, under the weaker assumption that at least some failure processes lead to partial melting (or similar process leading to a total lack of shear strength) and hence a "total stress drop" on the failure boundary. We can then use the event stress drop estimates from a large population of events to infer the ambient stress by plotting all the events in a restricted depth range on a map; and to then contour the stress sampling using the largest stress drop events to control the contours. Defining the ambient stress estimate in this way then allows us to determine whether the estimated stress from all the events conforms to the stress level pattern defined by the highest stress drop events. If all the stress drop estimates do in fact consistently conform in value with the contour levels, then we could reasonably infer that essentially all the events had stress drops from the ambient level to the same fixed level and that most likely this stress drop was total, with partial melting, or a similar weakening process, involved. This conclusion is of course predicated on there being a large data sample--a small sample would obviously disallow such a conclusion. In addition, it is required that no very large event take place in the time window of the data sample, since it would so strongly perturb the stress as to cause subsequent events in the vicinity to have much different stress drops.

Results from the Alaskan-Aleutian Region

Figures (25) through (28) show the results of applying this procedure to a fairly large total population of events from the Alaskan-Aleutian region. Here the events were separated into groups based on depth and type so that the stress estimates are plotted in particular depth ranges. These figures, taken together, present a picture of the stress level as a function of depth for the epicentral region covered by the zone outlined as "Seismic Region 1". The contouring was made using the highest stress drop events, as previously described. A close look at the individual stress drops for the whole population (see the figure legend for an explanation of the plotted numbers associated with each event) relative to the contours shows that with very few exceptions (i.e., two or three events) all the events are consistent with the contoured stress levels. This suggests (but does not necessarily require) that all the stress drops reduce the stress to a fixed level at the failure boundary or to a fixed fraction of the ambient level. In view of the wide variations in material properties to be expected both in depth and laterally along the plate boundary however, such consistency would strongly imply a total stress drop for the events.

Certainly one of the striking features of these results is the consistent variation of the stress with depth and along the plate boundary. In addition, the data give very high stresses in the region from Kodiak Island to the end of the Alaskan peninsula and this picture is consistent with the presence of a seismic gap in this region (eg. Sykes, 1971) and the fact that the recurrence data for large earthquakes in this region implies another large earthquake zone in the near future (eg. Shakal and Willis, 1972). Further we find that this stress estimation methods gives rather low stress levels for the zone of the 1964 Alaskan event, which would be expected.

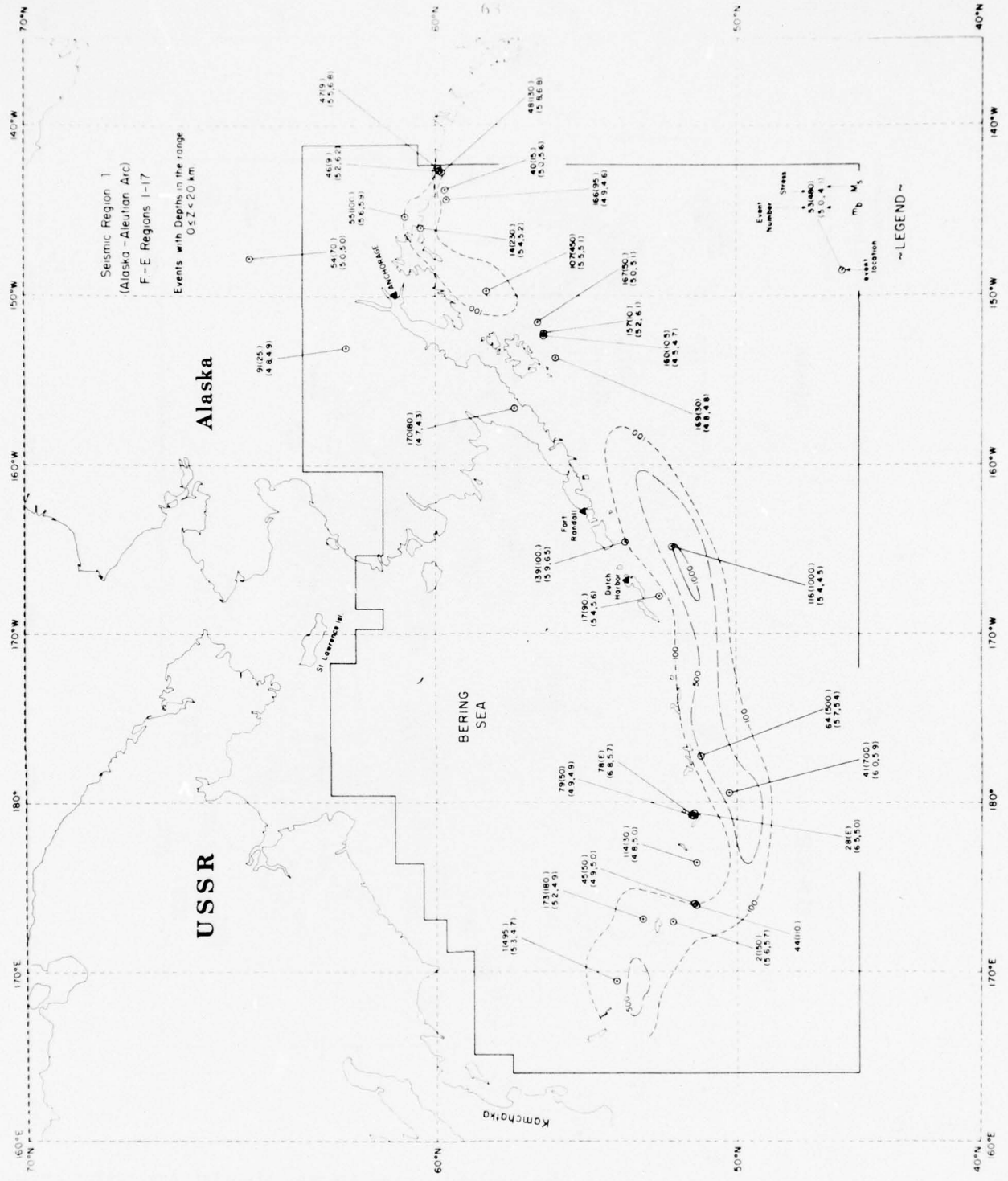

Figure 25: Epicenter stress map from events in the Alaskan-Aleutian Arc region having focal depths in the range from 0 to 20 km. Each event is denoted by a time sequenced event number, the stress drop and its m_b and M_s values as shown in the legend. The stress drop values are contoured to show the spatial stress pattern and provide a useful indication of the consistency of the results. The event numbers provide an indication of the time sequence of the sampling. If shear melting occurs in the failure zone (on the failure "plane"), then the stress levels shown are equal to the ambient prestress levels in the material.

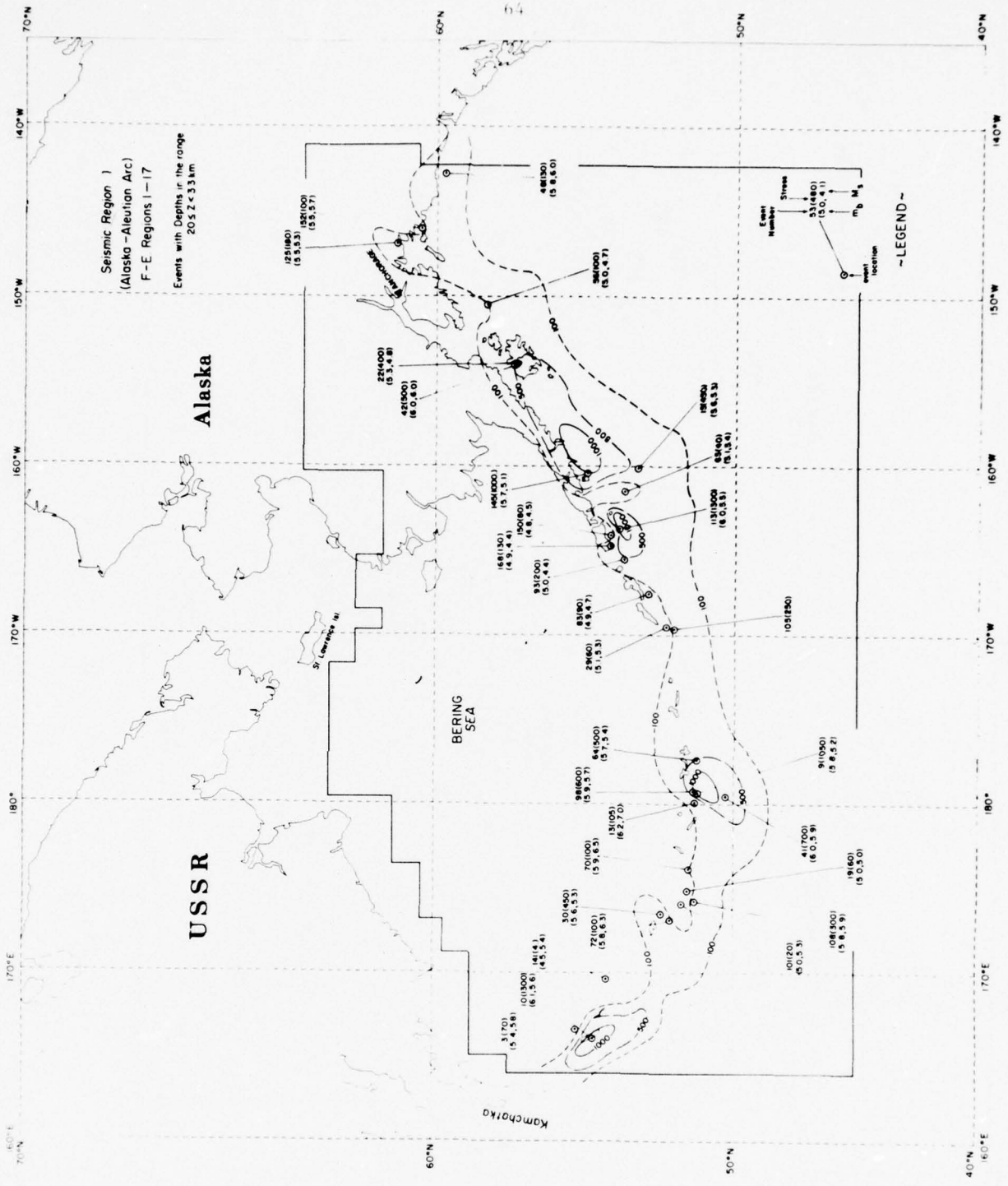

Figure 26: Epicentral stress map from events in the Alaskan-Aleutian Arc region having focal depths in the 20 to 33 km range. Events listed as being at a depth of 33 km are omitted from the data set shown and are treated separately since the assignment of a 33 km depth is the indication of unknown depth for an event. Note the high stress zones along the Alaskan peninsula in this depth range. This high stress zone appears to be correlated with the high stress region plunging downward and eastward along the Pacific plate boundary.

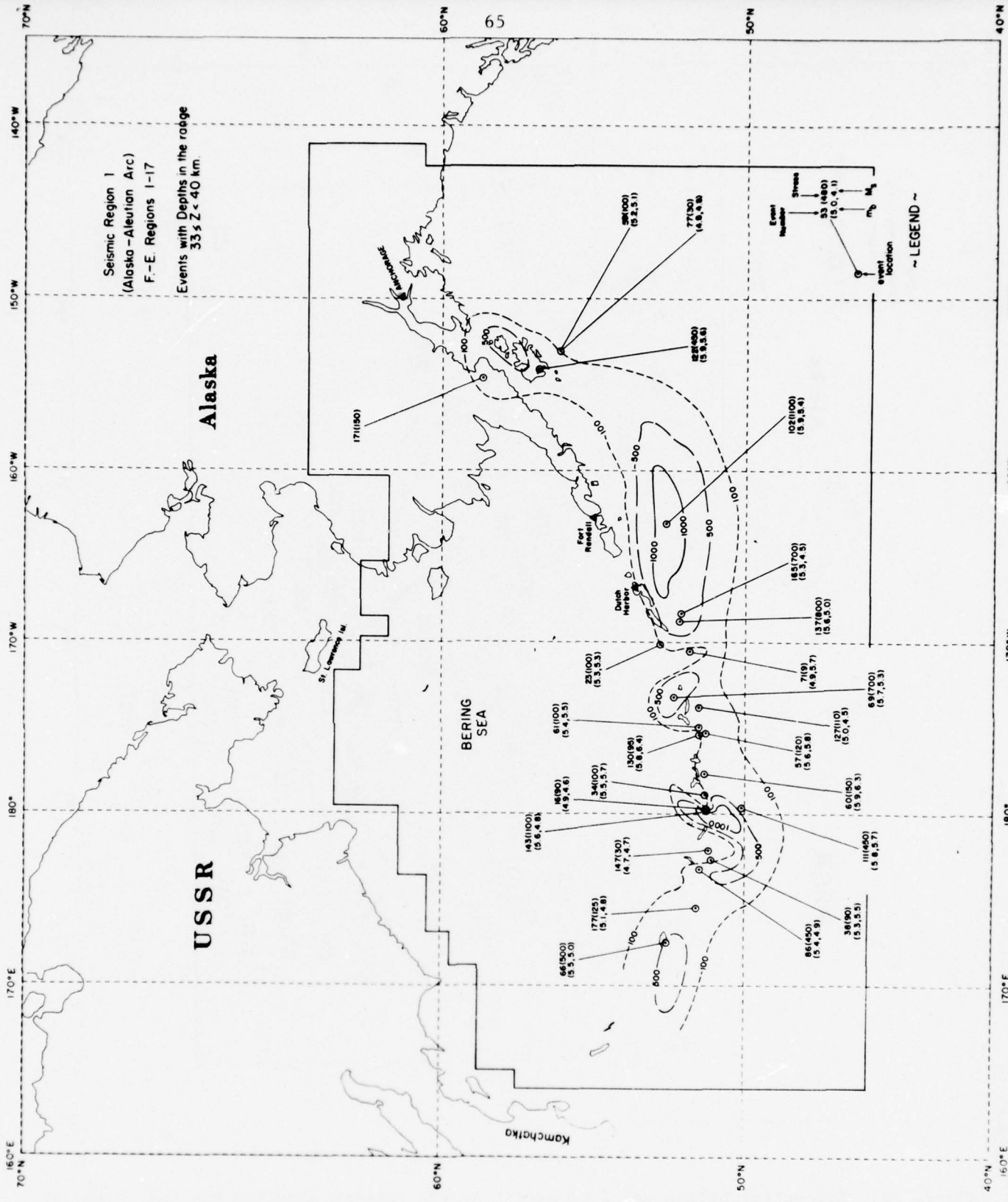

Figure 27: Epicentral stress map from events in the Alaskan-Aleutian Arc region having focal depths in the 33 to 40 km range. Events listed with hypocenters at 33 km are omitted. The high stress zone along the Alaska Peninsula is seen to persist through this depth interval, with the stress levels being, again, near the 1 kilobar level.

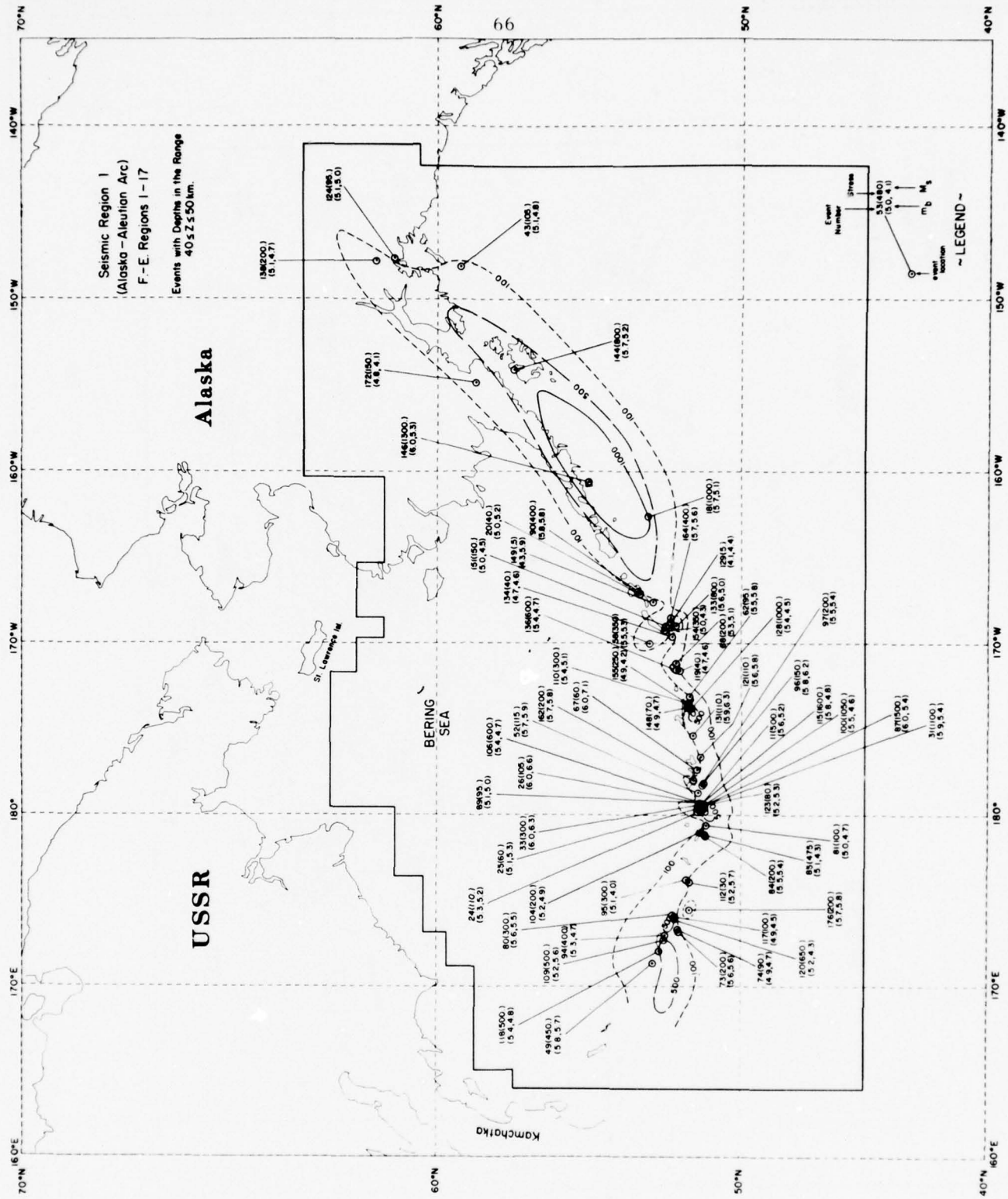

Figure 28: Epicentral stress map from events in the Alaskan-Aleutian Arc region having focal depths in the 40 to 50 km range. The high stress zone along the peninsula is larger and more extensive in this depth range than at the shallower depths. It is likely to be the depth range for nucleation of a very large earthquake as a result of failure along the plate boundary from just west of Kokiak Island to the end of the Alaskan Peninsula. For stress levels near 1 kbar, as shown, this event could occur at any time.

Results from the Japan-Kuriles-Kamchatka Region

Figures (29) through (32) show the inferred stress levels for the Japan region in the depth range from 0 to 50 km. Somewhat more data is available for this region than for the Alaskan zone and the stress estimates are correspondingly somewhat more detailed--and reliable. An outstanding feature of these results are delineated zones of very high stress, in the depth range 20 - 50 km, off the coasts of Kamchatka, Hokkaido and one off Honshu, near Tokyo. These patterns show some irregularity with depth but in general the high stress patterns are found to persist over a considerable range in depth. As with Alaska, the high stress zones are generally at depths greater than 20 km, with the stress levels near the surface more moderate. The one exception appears to be the very high stresses indicated in the Kuriles region in Figure (29). This stress zone appears to be located in the North American plate, northwest of the trench marking the plate boundary, rather than entirely in the narrow zone along the boundary itself.

A particularly critical test of the entire approach is available using the data set for this region. Specifically, we should obtain a high stress level in a concentrated zone before a large earthquake, while after the event we should obtain a stress pattern which is considerably changed. One would expect a general reduction in the stress with perhaps some high stress concentration levels at the ends of the failure zone. The Japan region data contained two large events with reasonably large numbers of small events occurring both before and after them, and consequently we can test the seismic stress estimates obtained against the criteria that the local stress level be generally lower after such a large event.

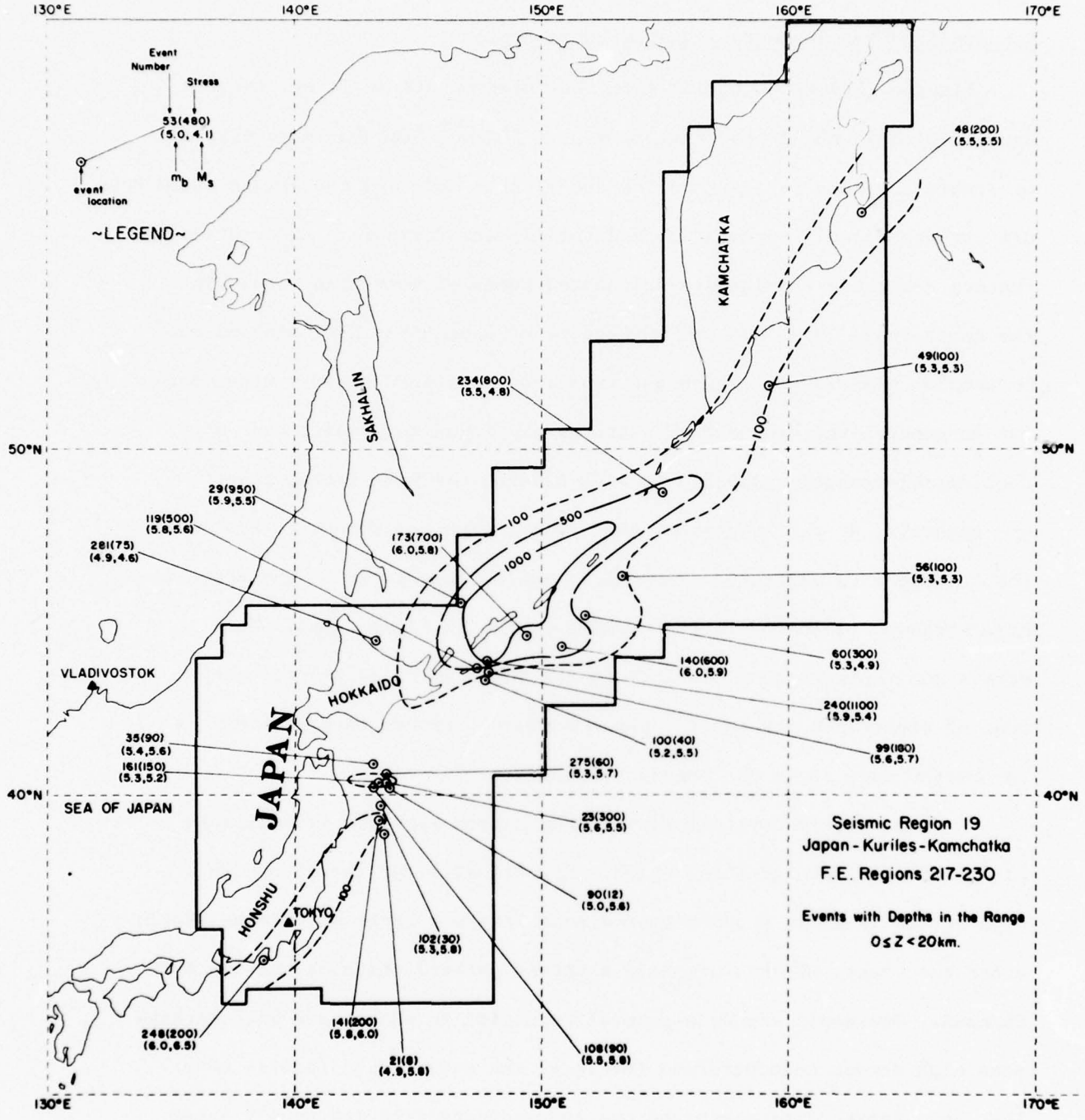

Figure 29: Epicentral stress map from events in the Japan-Kuriles-Kamchatka region for the depth range from 0 to 20 km. The high stress zone in the Kuriles region corresponds to a shallow stress concentration of apparently large dimension within the Asian plate, which is being underthrust by the Pacific plate.

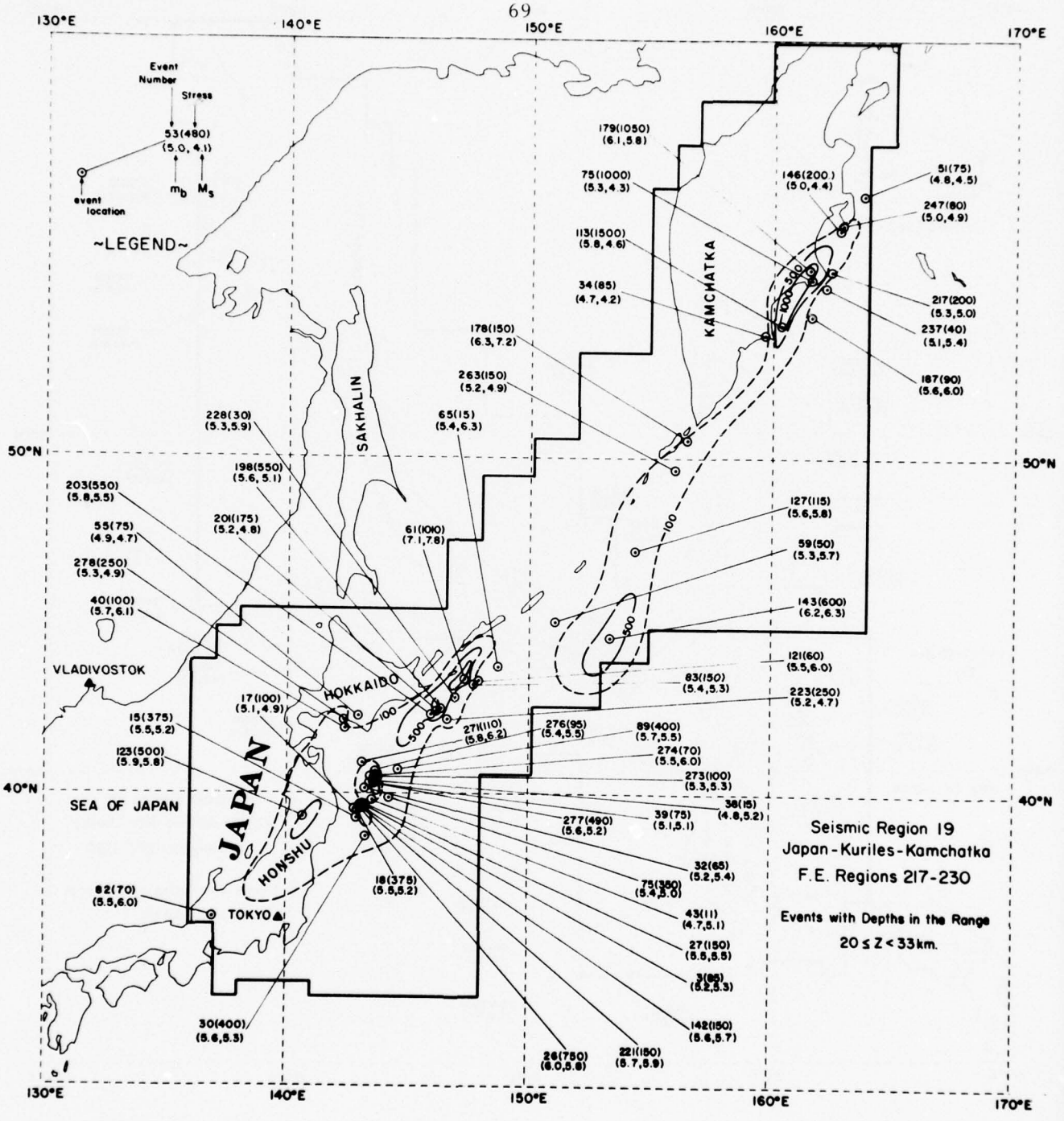

Figure 30: Epicentral stress map from events in the Japan-Kuriles-Kamchatka region for the depth range from 20 to 33 km. High stress zones occur along the Kamchatka and Hokkaido-Honshu coasts, with the latter zone showing a complex pattern of high and low stresses characteristic of zones of recent large earthquakes such as event no. 61.

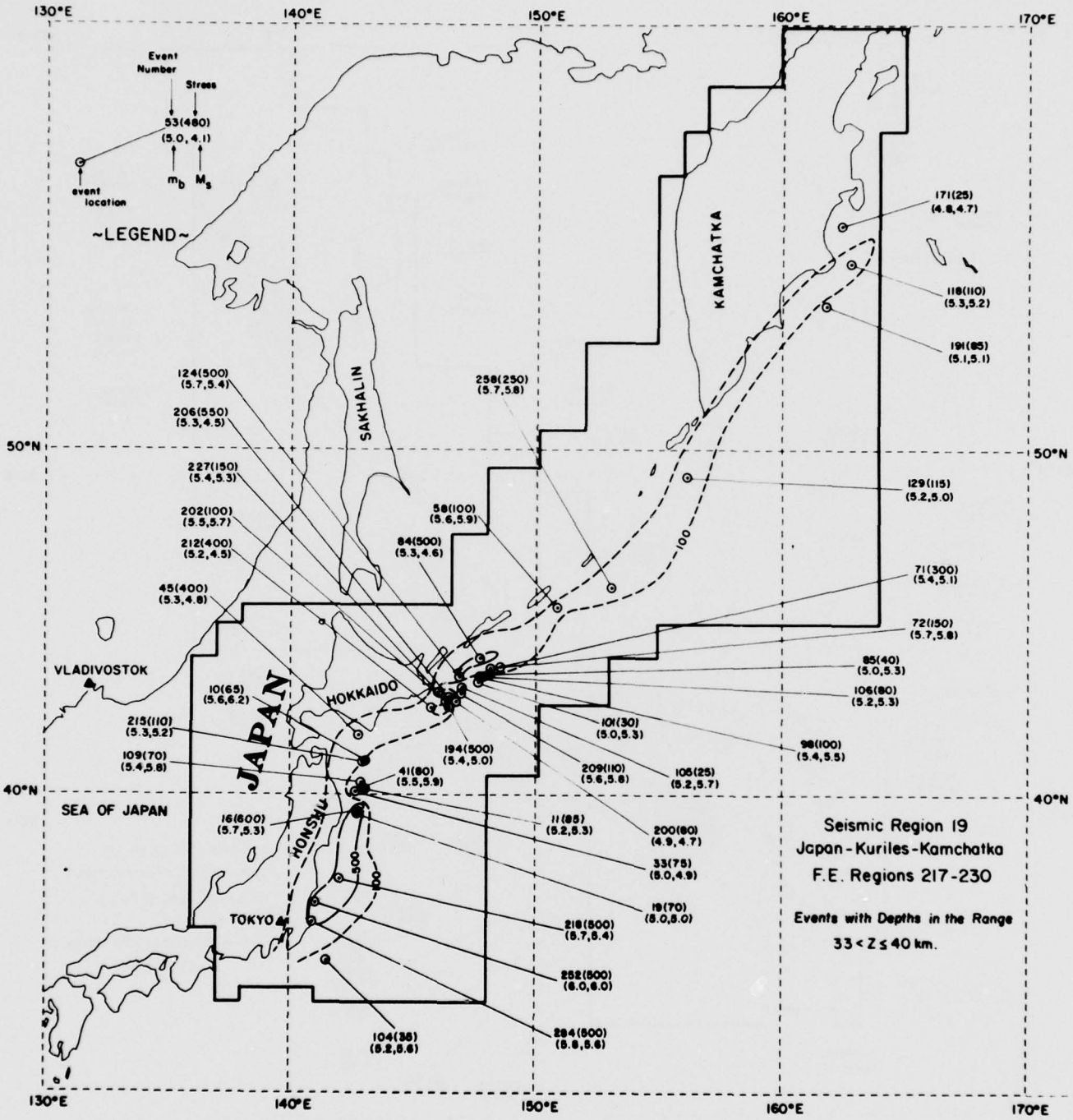

Figure 31: Epicentral stress map from events in the Japan-Kuriles-Kamchatka region for the depth range from 33 to 40 km. The high stress zone off the Honshu coast appears more regular and extensive in this depth range and constitutes a high risk zone-especially in view of its proximity to Tokyo.

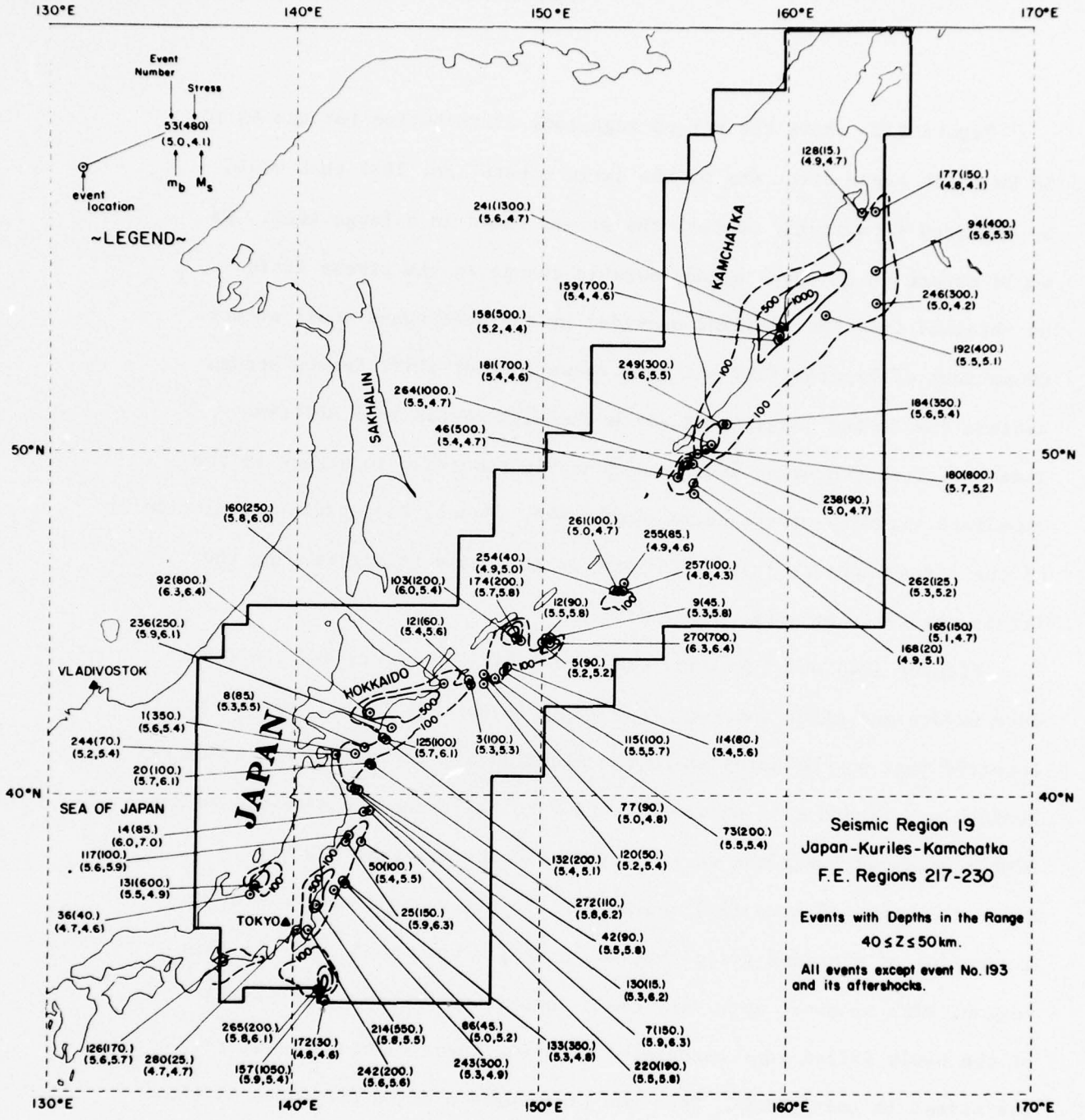

Figure 32: Epicentral stress map for the Japan-Kuriles-Kamchatka seismic region from events having focal depths in the depth range 40 to 50 km, with events occurring before the large event, No. 193, represented. This event and its aftershocks occurred within the moderately high stress zone off the northeast point of Hokkaido and results in a considerable change in the stress level and spatial pattern.

Figure (33) shows the stress magnitude distribution for the 40 to 50 km depth range after one of the large events (No. 193) that would be expected to strongly perturb the stress field in a large zone. We would expect to observe a considerable change in the stress field as obtained from the sampling provided by the subsequent small events. Comparison of Figures (32) and (33) shows a major shift in the stress pattern due to the large event, with the high stress zone shifting landward after the event and a considerable reduction in stress in the immediate vicinity of the large earthquake. Hence, our spatial resolution of the stress appears just sufficient in this case to verify that the stress change is as would be expected.

Figures (34) and (35) show the stress field contours and the event data before and after another large event (Event No. 144). This event occurred just at the point where the Aleutian arc intersects the Kamchatka Peninsula. Figure (34) shows that prior to the event the zone was rather highly stressed, with the stress level reaching at least 500 bars. After the event, Figure (35) shows that the later small events provide a sampling of a stress field that is generally very much lower in this region, with however, some very small zones--presumably near the ends of the newly failed zone associated with the large earthquake--where the stress is quite high. Thus the time-space picture presented by this event sequence again entirely conforms to what we know should occur.

Finally we also observe, as for the Alaska region, that the stress levels obtained by contouring on the basis of the largest stress drop values obtained at each point are consistent with (very nearly) all the observations. That is, when a high stress zone is delineated by a

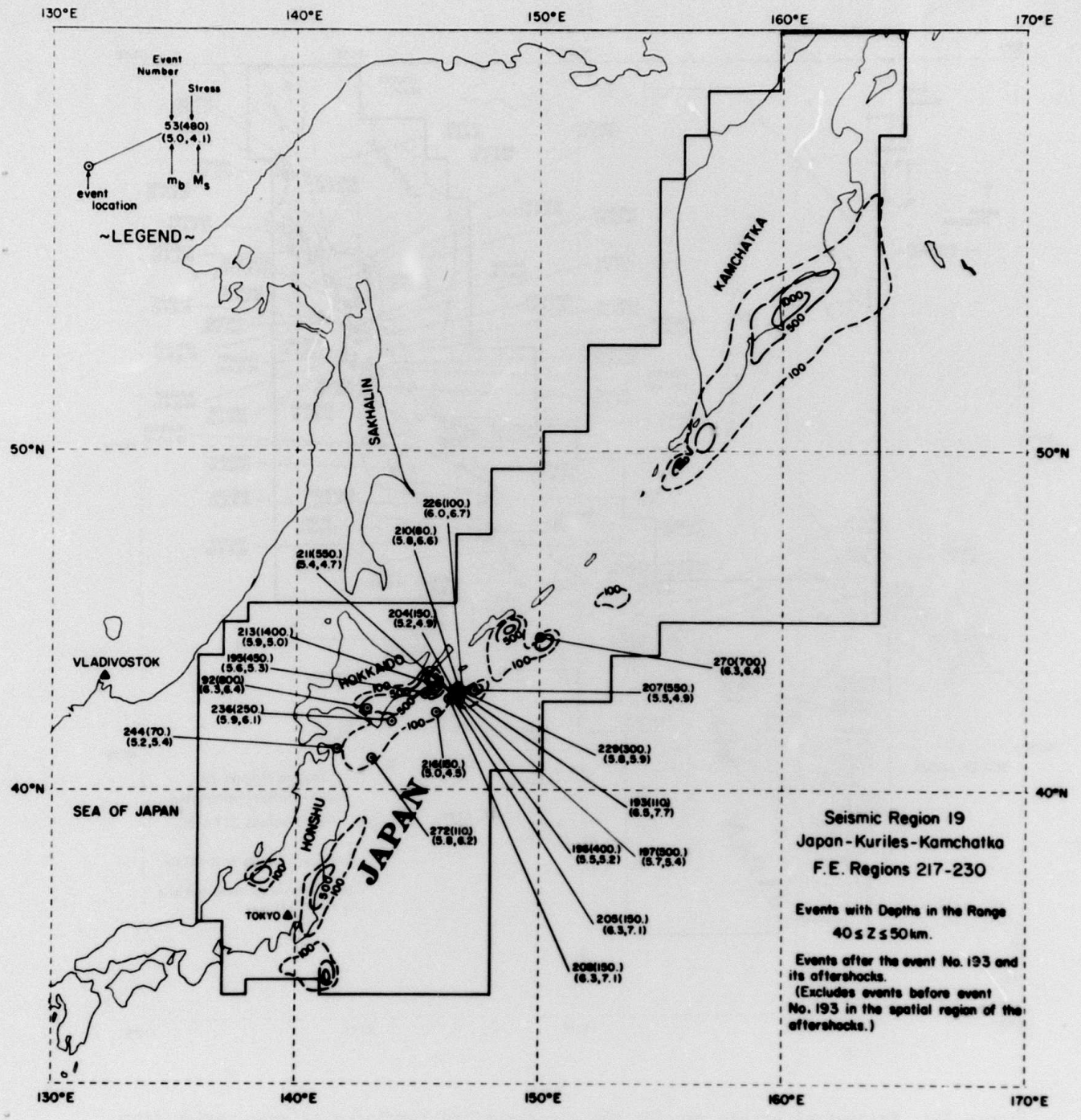

Figure 33: Epicentral stress map for the Japan-Kuriles-Kamchatka seismic region from events having focal depths in the depth range 40 to 50 km, with the events used including event No. 193 and its aftershocks, but excluding events before 193 in the Northern Hokkaido region. Comparison with Figure 40 shows a strong shift in the stress pattern with an increase in the stress level shoreward, to a level near 1 kbar, and a decrease of stress in the zone of faulting for this large event.

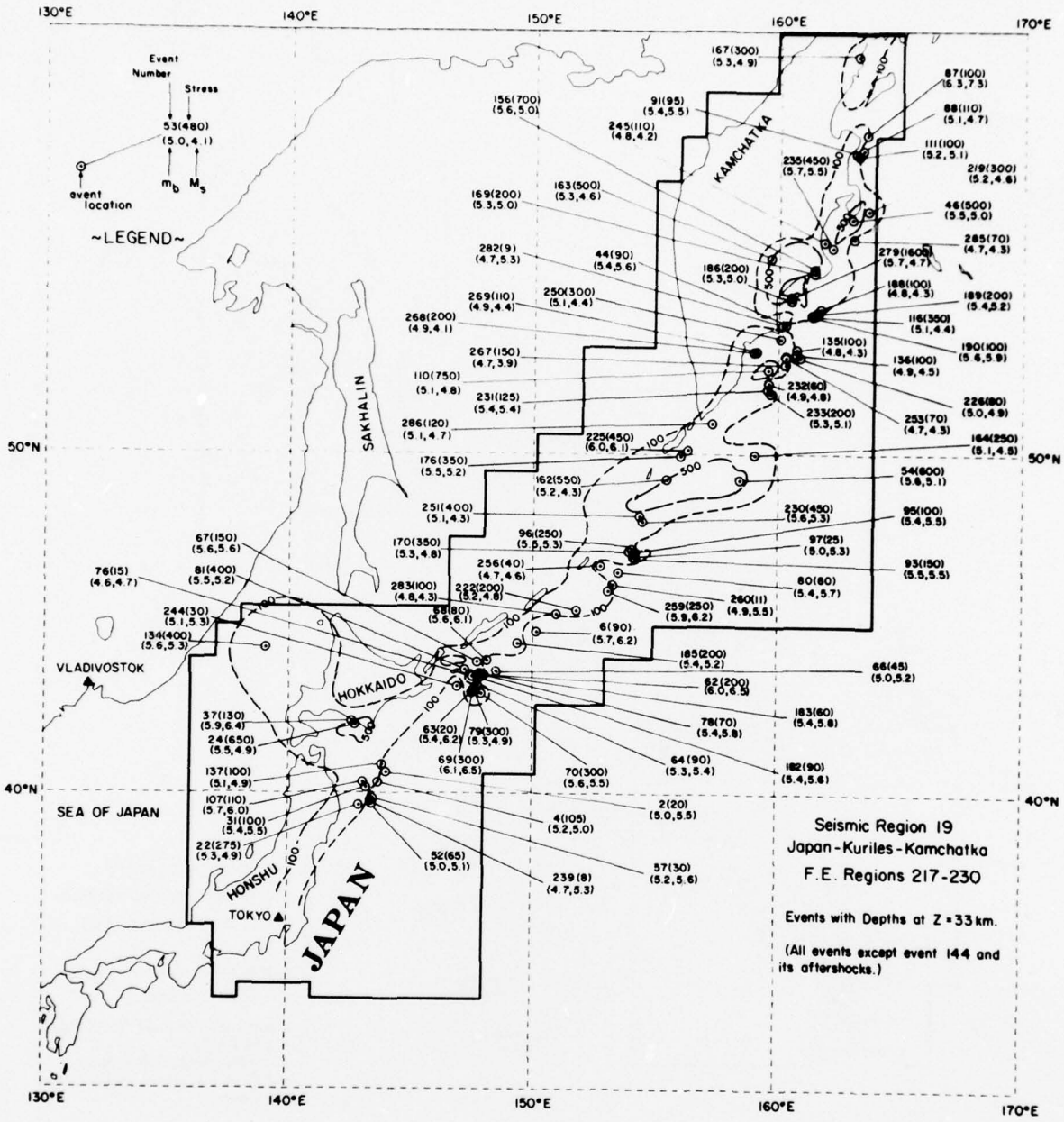

Figure 34: Epicentral stress map for the Japan-Kuriles-Kamchatka seismic region from events having focal depths given as 33 km, with only the events before the large event No. 144 represented. Event No. 144, which occurred off the coast of Kamchatka, and its aftershocks are not included so that the stress field prior to this event is shown. It corresponds to the northern-most high stress zone along the Kamchatka coast.

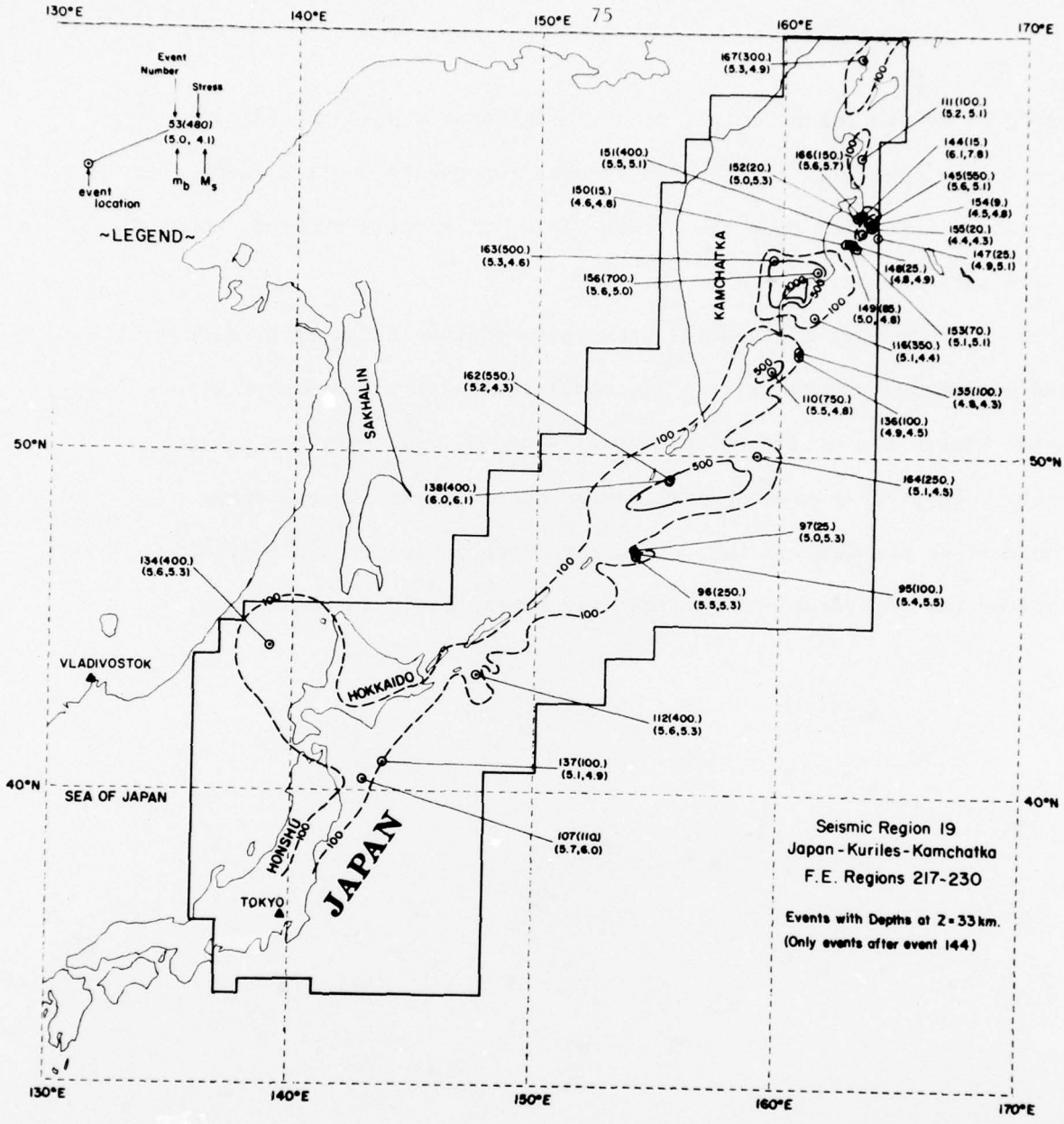

Figure 35: Epicentral stress map for the Japan-Kuriles-Kamchatka from events with focal depths at 33 km, with event No. 144 and its aftershocks included. The stress field in the northern high stress zone is now much reduced, with some high stress indicating events occurring near what appears to be the edges of the new failure zone. The stress level, as evidenced by the event sampling, therefore appears to be much lower, as would be expected, but with higher stress near the edges of the recent failure "plane" formed by the large event, as also would be expected.

sampling of events for a region, then we find that subsequent (small) events in the zone will all be high stress drop events until a large event occurs, at which time the stress field is greatly changed, usually over the entire zone.

We conclude that the general space-time picture obtained from this stress estimation procedure is quite consistent with the expected stress behavior within the active seismic zones studied. Further, the results strongly suggest that most events involve total (shear) stress drops on the failure boundary so that the stress drop estimates are a direct measure of the recoverable nonhydrostatic stress field in the medium.

VI. Summary and Conclusions.

Some conclusions that have been drawn that are of importance for the earthquake-explosion discrimination problem and for a general understanding of earthquake elastic wave radiation fields are:

(i) A relaxation source theory appears to provide predictions of the radiation field from earthquakes that are in good agreement with observations, specifically m_b-M_s and other magnitude data and spectra from near field observations of earthquake radiation.

(ii) The earthquake theory, combined with explosion source model theory, provides a coherent explanation of the m_b-M_s discriminent. It also provides a predictive basis for ascertaining when and under what circumstances this discriminent can fail. That is, it provides a basis of understanding of anomalous events.

(iii) Theoretical predictions of spectral magnitude discriminents indicate that a short period body wave magnitude discrimination can be at least as effective as m_b-M_s discrimination and in general provides a wider separation of explosion-earthquake populations to lower magnitudes ($m_b \sim 4.0$) with few if any anomalous shallow earthquakes appearing in the explosion population. Observational tests of the theoretical predictions using roughly 200 Eurasian events have confirmed these predictions. The only earthquakes within the explosion population were some very deep earthquakes. In addition, both single and multiple explosions (the latter designed to appear as earthquakes to all other discriminents, including m_b-M_s) were identified by this discriminent as explosions. This discriminate is easily implemented in the field and as an on-line processor to detect and identify event signals.

Other spectral magnitude measurements employing surface waves were also shown to be discriminatory, but the theoretical predictions have not been observationally verified in detail.

(iv) Analysis of several hundred events in the North Pacific region shows that the stress environment surrounding a failure zone and leading to failure can in many cases be highly inhomogeneous with local nonhydrostatic stress concentrations, of relatively small spatial extent, of the order of 1.0 kb. Most moderate sized earthquakes, however, appear to occur in zones with average prestress at the 100 bar level, with the stress quite uniform over regions of the order of 100 km in radius.

(v) Near field spectra observations and m_b-M_s data for small earthquakes ($m_b \leq 5$), suggest strongly peaked far field spectra for at least some earthquakes. A conclusion to this effect is compatible with the deduced strong spatial variations in stress (indeed it would logically follow) provided that the R_S factor approximation used in the relaxation source theory is a reasonably accurate means of representing the radiation from relaxation of spatially variable prestress. A consequence of strongly peaked far field radiation is a reduction in the observed M_s value, with the event appearing explosion-like in the m_b-M_s plane.

(vi) Comparisons of theoretical predictions from the analytical relaxation source theory models and complex purely numerical, two and three dimensional earthquake models employing failure criteria, including plasticity, are in substantial agreement. This agreement lends strong support to the reliability of the "first order" relaxation theory models of earthquakes.

(vii) A general Green's function representation of the radiation field produced by rapid material failure in a generally prestressed medium has been obtained. The theory includes the complex dynamical

boundary conditions for an expanding failure. It is shown that the theory is amenable to approximations allowing reliable and quite general models to be constructured and for which analytical results can be obtained. Development of these higher order models was initiated during the period of this study with some preliminary results obtained by the end of the contract period.

Anderson, D. L. 1967, Latest Information from Seismic Observations, Chapter XII in The Earth's Mantle, edited by T. F. Gaskell, 355-420.

Anderson, D. L. and C. B. Archambeau, 1964, The Anelasticity of the Earth J. Geophys. Res., 69, 2071-2084.

Anderson, D. L., A. Ben-Menahem and C. B. Archambeau, 1965, Attenuation of Seismic Energy in the Upper Mantle, J. Geophys. Res., 70, 1441-1448.

Archambeau, C. B., 1968. General Theory of Elastodynamic Source Fields Rev. Geophys., 6, 241-288.

Archambeau, C. B., 1974., Investigations of Tectonic Stress. Semi-Annual Technical Report, Contract F19628-74-C-0087, ARPA Order No. 1795, Report No. AFCRL-TR-0424.

Archambeau, C. B., 1975a. Developments in seismic source theory, Rev. Geophys. Space Physics, 13, 3, 304-3-6.

Archambeau, C. B., 1975b. Investigations of tectonic stress, Final Report ARPA Order No. 1795, Contract No. F19628-74-C-0087, August 1975.

Archambeau, C. B., 1975a, Studies of Tectonic Processes Associated with Fluid Injection and Surface Loading, Final Report, ARPA-USGS Fluid Injection/Waste Disposal Research Program, Contract No. 14-08-0001-12716, February 1975.

Archambeau, C. B., 1975b, Investigations of Tectonic Stress, Final Report ARPA Order No. 1795, Contract No. F19628-74-C-0087, August 1975.

Archambeau, C. B., 1976, Earthquake Prediction Based on Tectonic Stress Determinations, Abstract Am. Geophys. Union (EOS) April 1976 Meeting.

Archambeau, C. B., E. A. Flinn, and D. G. Lambert, 1969, Fine Structure of the Upper Mantle, J. Geophys. Res., 74, 5825-5865.

Archambeau, C. B., D. G. Harkrider and D. V. Helmberger, 1974, Studies of Multiple Seismic Events, Final Report to U.S. Arms Control and Disarmament Agency, Contract ACDA/ST-220.

Archambeau, C. B., and J. B. Minster, 1976a, Dynamics in prestressed media with moving phase boundaries: A continuum theory of failure in solids, submitted to Geophys. J. Roy. astr. Soc.

Archambeau, C. B., and J. B. Minster, 1976b, Elastodynamic representation theorems for prestressed media with moving phase boundaries, submitted to J. Geophys. Res.

Bache, T. C., J. T. Cherry, K. G. Hamilton, J. F. Masso and J. M. Savino 1975, Application of Advanced Methods for Identification and Detection of Nuclear Explosions from the Asian Continent, Semi-Annual Technical Report, Systems, Science and Software, SSS-R-75-2646.

Bache, T. C., J. T. Cherry, N. Rimer, J. M. Savino, T. R. Blake, T. G. Barker, and D. G. Lambert, 1975, An Explanation of the Relative Amplitudes of the Teleseismic Body Waves Generated by Explosions in Different Test Areas at NTS Systems, Science and Software Final Report DNA Contract No. DNA001-75-C-0222, Report No. SSS-R-76-2746.

Bache, T. C., and C. B. Archambeau 1976, Comparisons of Observations with Predicted Teleseismic Signals from Relaxation Theory Models of Earthquakes, to be submitted to J. Geophys. Res.

Bache, T. C. and D. G. Harkrider, 1976, The Body Waves due to a general seismic source in a layered earth model: (1.) Formulation of the Theory, submitted to Bull. Seism. Soc. Am.

Bache, T. C., J. T. Cherry, D. G. Lambert, J. F. Masso and J. M. Savino, 1976. A deterministic methodology for discriminating between earthquakes and underground nuclear explosions, Systems, Science and Software Semi-Annual Report, SSS-R-76-2925.

Barker, T. G., 1976. Calculations of the effects of layered geology on near-field ground motion using a hybrid finite difference/linear elastic code for the NTS event MIGHTY EPIC, Systems, Science and Software Topical Report, SSS-R-76-2914.

Barr, K. G., 1967, Upper Mantle Structure in Canada from Seismic Observations using Chemical Explosions, Can. J. Earth Sci., 4, 961-975.

Brune, J. N., 1969, Surface Waves and Crustal Structure, in The Earth's Crust and Upper Mantle, Geophys. Monograph 13, Am. Geophys. Union, Washington, D. C.

Brune, J. N., 1970, Tectonic stress and the spectra of seismic shear waves from earthquakes, J. Geophys. Res., 75, 4997. Corrected 1971, J. Geophys. Res., 76, 5002.

Brune, J. N. and J. Dorman, 1963, Seismic Waves and Earth Structure in the Canadian Shield, Bull. Seism. Soc. Am., 53, 167-209.

Cherry, J. T., 1973, Calculation of near-field earthquake ground motion, SSS-R-73-1759, Systems, Science and Software, Annual Report, A.R.P.A. Order No. 2134.

Cherry, T., C. B. Archambeau, G. A. Frazier, A. J. Good, K. G. Hamilton and D. G. Harkrider, 1972, The teleseismic radiation field from explosions, SSS-R-72-1193, Systems, Science and Software, Final Report, Contract nb. DADA-01-71-C-0156.

Cherry, J. T., C. B. Archambeau, G. A. Frazier, A. J. Good, K. G. Hamilton, and D. J. Harkrider 1973, The teleseismic radiation field from explosions: Dependence of Seismic amplitudes upon Properties of Materials in the source region, Systems, Science, and Software Final Report, DNA 3113Z.

Cherry, T., T. C. Bache, C. B. Archambeau and D. G. Harkrider, 1974a, A deterministic approach to the prediction of teleseismic ground motion from nuclear explosions, Systems, Science and Software, Final Contract Report, DNA 2231 F.

Cherry, J. T., T. C. Bache, C. B. Archambeau, and J. M. Savino, 1974b Explosion Yield Estimates Based on Seismic Magnitude Observations: Dependence on Yield, Near Source Material Properties, Depth of Burial and Earth Structure Topical Report No. SSS-R-74-2400, Systems, Science and Software Contract No. F-44620.

Cherry, J. T., T. C. Bache, and J. F. Masso, 1976, A Three Dimensional Finite Difference Simulation of Earthquake Faulting, Abstract; Am. Geophys. Union (EOS), April 1976 Meeting.

Cherry, J. T., E. J. Halda and K. G. Hamilton, 1976, A Deterministic Approach to the Prediction of Free Field Ground Motion and Response Spectra from Stick-slip Earthquakes Earthquake Engineering and Structural Dynamics, Vol. 4, 315-332.

Engdahl, E. R., 1973, Location of Intermediate Depth Earthquakes in the Central Aleutians by Seismic Ray Tracing, Nature, Phys. Sci., 245, 23-25.

Engdahl, E. R., 1975, Effects of Plate Structure and Dilatancy on Relative Teleseismic P-wave Residuals, Geophys. Res. Let., 2, 420-422.

Engdahl, E. R., and W. H. K. Lee, 1975, Relocation of Local Earthquakes by Seismic Ray Tracing, in press, J. Geophys. Res.

Evernden, J. F., 1967. Magnitude determination at regional and near regional distances in the United States, Bull. Seism. Soc. Am., 57, 591-639.

Evernden, J. F., R. R. Hibbard and J. F. Schneider, 1973. Interpretation of seismic intensity data, Bull. Seism. Soc. Am., 63, 399-422.

Gilbert, F., and D. V. Helmberger, 1972. Generalized ray theory for a layered sphere, Geophys. J., 27, 57-80.

Gutenberg, B., 1944. Travel times of principal P and S waves over small distances in Southern California, Bull. Seism. Soc. Am., 34, 13.

Hanks, T. C., 1974. The faulting mechanism of the San Fernando earthquake, J. Geophys. Res., 79, 1215.

Hanks, T. C., 1974, The faulting mechanism of the San Fernando earthquake, J. Geophys. Res., 79, 1215.

Harkrider, D. G., 1964, Surface Waves in Multilayered media, I. Rayleigh and Love Waves from Sources in a Multilayered Half-Space, Bull. Seism. Soc. Am., 54, 627-679.

Harkrider, D. G., and C. B. Archambeau, 1976, Theoretical Rayleigh and Love Waves from seismic Sources in Prestressed Media, to be submitted to Bull. Seism. Soc. Am.

Helmberger, D. V., 1971, Upper Mantle Structure of the Midwestern United States, J. Geophys. Res., 76, 3229.

Helmberger, D. V., 1974, Generalized Ray Theory for Shear Dislocations, Bull. Seism. Soc. Am., 64, 45-64.

Herrin, E., 1968. Introduction to 1968 Seismological Tables for P phases, Bull. Seism. Soc. Am., 58, 1193-1242.

Hileman, J. A., C. R. Allen and J. M. Nordquist, 1973. Seismicity of the Southern California Region 1 January 1932 to 31 December 1972, Seismological Laboratory, California Institute of Technology, p. 83.

Johnson, L. R. and T. V. McEvilly, 1974, Near-field observations and source parameters of central California earthquakes, Bull. Seism. Soc. Am., 64, 1855-1886.

Johnson, T. L., and C. H. Scholz, 1976, Dynamic Properties of Stick-Slip Friction of Rock, J. Geophys. Res., 81, 881-888.

Jordan, T., and D. L. Anderson, 1974, Earth Structure from Free Oscillations and Travel Times, Geophys. J. Roy. astr. Soc., 36, 411.

Julian, B. R., and D. L. Anderson, 1968, Travel Times, Apparent Velocities and Amplitudes of Body Waves, Bull. Seism. Soc. Am., 58, 339-366.

Jungels, P. H., 1973, Modeling of Tectonic Processes Associated with Earthquakes, Thesis, California Institute of Technology, Pasadena, Ca.

Jungels, P. H., and G. A. Frazier, 1973, Finite element analysis of the residual displacements for an earthquake rupture: Source parameters for the San Fernando earthquake, J. Geophys. Res., 89, 5062.

Kelleher, J. A., 1970. Space-time seismicity of the Alask-Aleutian seismic zone, J. Geophys. Res., 75, p. 5745.

Kelleher, J. and J. Savino, 1975. Distribution of seismicity before large strike slip and thrust-type earthquakes, J. Geophys. Res., 80, 260-271.

Kisslinger, C., and E. R. Engdahl, 1973, The Interpretation of the Wadati Diagram with Relaxed Assumptions, Bull. Seism. Soc. Am., 63, 1723-1736.

Madariaga, R., 1976. Dynamics of an expanding circular fault, Bull. Seism. Soc. Am., 66, 639-666.

Minster, J. B., 1973. Elastodynamics of Failure in a Continuum, Ph.D. Thesis, California Institute of Technology, Pasadena, CA.

Minster, J. B., and C. B. Archambeau, 1976, Seismic radiation fields from relaxation source theory models of earthquakes, to be submitted to Geophys. J. Roy. astr. Soc.

Molnar, P. and M. Wyss, 1972, Moments, Source Dimensions and Stress Drops' of Shallow Focus Earthquakes in the Tonga-Kermadec Arc, Phys. Earth and Planet. Int., 6, 263-278.

Savino, J. M., T. C. Bache, J. T. Cherry, K. G. Hamilton, D. G. Lambert and J. F. Masso, 1975. Application of advanced methods for identification and detection of nuclear explosions from the Asian Continent, Systems Science and Software Semi-Annual Technical Report, SSS-R-2792.

Savino, J. M., and C. B. Archambeau, 1976, Discrimination of Earthquakes from Single and Multiple Explosions Using Spectrally Defined Event Magnitudes, to be submitted to J. Geophys. Res., abstract AGU, 56, 1148, 1974.

Shakal, A. F., and D. E. Willis, 1972, Estimated Earthquake Probabilities in the North Circum-Pacific Area, Bull. Seism. Soc. Am., 62, 1397-1410.

Solomon, S. C., 1972, Seismic Wave Attenuation and Partial Melting in the Upper Mantle of North America, J. Geophys. Res., 77, 1483-1502.

Sykes, L. R., 1971, Aftershock Zones of Great Earthquakes, Seismicity Gaps and Earthquake Prediction for Alaska and the Aleutians, J. Geophys. Res., 76, 8021, 8041.

Thatcher, W., and T. C. Hanks, 1973. Source parameters of Southern California earthquakes, J. Geophys. Res., 78, 8547-8576.

Toksoz, M. N., and D. L. Anderson, 1966, Phase Velocities of Long-Period Surface Waves and Structure of the Upper Mantle, 1. Great Circle Love Rayleigh Wave Data, J. Geophys. Res., 71, 1649-1658.

Trifunac, M. D., 1972, Stress estimates for the San Fernando, California earthquake of February 9, 1971; Main event and thirteen aftershocks, Bull. Seism. Soc. Amer., 62, 721.

Tucker, B. E., and J. N. Brune, 1973. Seismograms, S-wave spectra and source parameters for aftershocks of the San Fernando earthquake of February 9, 1971, in Geological and Geophysical Studies, Vol. 3, San Fernando Earthquake of February 9, 1971, NOAA, U. S. Department of Commerce, Washington, D. C.

Wiggins, R. A., and D. V. Helmberger, 1973, Upper Mantle Structure of the Western United States, J. Geophys. Res., 78, 1870-1888.

Wiggins, R. A., and D. V. Helmberger, 1974, Synthetic Seismogram Computation by Expansion in Generalized Rays, Geophys. J. Roy. astr. Soc., 37, 73-90.

Wyss, M., 1970a, Stress estimates of South American shallow and deep earthquakes, J. Geophys. Res., 75, 1529-1544.

Wyss, M., 1970b, A comparison of apparent stresses of earthquakes on ridges with earthquakes in trenches, Geophys. J. Roy. astr. Soc., 19, 479.

Wyss, M. and J. N. Brune, 1968, Seismic moment, stress and source dimensions for earthquakes in the California-Nevada region, J. Geophys. Res., 73, 4681.

Wyss, M. and J. N. Brune, 1971, Regional variations of source parameters in Southern California estimated from the ratio of short to long period amplitudes, Bull. Seism. Soc. Amer., 61, 1153-1167.

Wyss, M. and T. C. Hanks, 1972a, Source parameters of the Borrego Mountain, California, earthquake, U.S. Geol. Survey Prof. Paper, 787, 24-30.

Wyss, M. and T. C. Hanks, 1972b, The source parameters of the San Fernando Earthquake inferred from Body Waves, Bull. Seism. Soc. Amer., 62, 591.

Appendix A

Dynamics in Prestressed Media with Moving Phase Boundaries: A Continuum Theory of Failure in Solids

by

C. B. Archambeau[1]

and

J. B. Minster[2]

---

[1]CIRES, University of Colorado/NOAA, Boulder, Colorado 80309

[2]California Institute of Technology, Pasadena, California 91125

Abstract

Spontaneous failure in a solid medium is described as a localized transition of the material from one physical state to another, characterized in part by contrasting rheological properties and density. Such a process is viewed as a local disordering of the relatively ordered structure of the solid due to any variety of causes, such as massive microfracturing or shear melting, and can be confined to a very thin zone, but nevertheless of finite volume such that a volumetric transition energy can be defined. This leads to the description of failure as a generalized phase transition in a prestressed continuum, with instability and transition zone growth being driven by the energy contributions from the relaxation of stress in the surrounding medium. Direct application of mass, momentum and energy conservation to such a generalized phase transition leads to "jump" conditions specified on the growing boundary surface of the transition zone, that relate the rupture growth to discontinuous changes in the dynamic field variables across the failure zone boundary. These field discontinuities are, in turn, related to the localized changes in physical properties induced by failure. Dynamical conditions for rapid spontaneous failure growth in a stressed medium are investigated in some detail, and we find that the failure boundary growth can be simply expressed in terms of energy "failure condition" and a dynamic growth condition specifying the rupture velocity. These results imply that the internal energy change associated with earthquakes is in the range 10^4-10^6 ergs/gm. Further the failure growth rate is shown to be expressible in terms of the rheological properties of the material before and after failure. For shear melting resulting in a low viscosity fluid, for example, the rupture velocity will be near the shear velocity of the original material. A general Green's function solution for the radiation due to stress relaxation in the medium surrounding the growing failure zone is given and provides the basis for detailed computations of the strain or displacement field changes due to spontaneous failure processes. In particular, it is shown that the jump conditions for the growing transition zone boundary appear naturally as surface integral terms over the boundary. Since these boundary conditions contain the failure rate explicitly, then these terms include effects that have not been represented in previous integral representations of the radiation field resulting from failure. Further, we show that the formal Green's integral representation for the dynamical wave field can be used with known, simple Green's functions to generate approximate solutions for complex failure processes occurring in media with inhomogeneous material properties and prestress.

1. Introduction

A general description of material failure under stress loading is obtained within the frame of continuum mechanics by considering the failure process to be a generalized phase transition (Archambeau, 1969). In this description the failure zone occupies a finite volume, the boundary of which corresponds to a moving phase boundary in a prestressed medium. The growth of the failure zone is then controlled by the energy balance at the "phase transition". That is, we can define, as a macroscopic equivalent, a "latent heat" of transition, associated with the energy required for microfracture and/or partial melting along grain boundaries or fracture surfaces. This energy term can be used as an intrinsic characteristic of the material, and describes the energetics of the irreversible processes of failure.

From this point of view it is not necessary to specify the microscopic details of the failure process, which may involve brittle fracture, plastic flow, melting, etc. ..., but only the composite irreversible energy required for these processes, as a function of temperature, pressure and material type.

The dynamical evolution of the failure zone is then controlled by the laws of conservation of mass, momentum, and energy, in a continuum including a moving phase boundary. Because of the discontinuous behavior of the medium at the failure boundary, the momentum and energy equations are coupled through boundary conditions at the failure surface. However, one can still construct a Green's tensor representation theorem for the radiated field, in

which the coupling appears as a term involving rupture velocity in the boundary surface integral over the failure surface. Since the radiation field arises from the relaxation of stress in the surrounding medium, the elastic field representation corresponds to that for relaxation source theory (e.g., Archambeau, 1968, 1972; Minster, 1973).

In this paper we shall give a concise account of the theoretical development of the basic conservation conditions that must hold in a continuum with localized discontinuous properties. We shall then focus on the case where the dynamical deformation of the surrounding medium induces rapid growth of a failure zone, since it corresponds to observed tectonic failure resulting in earthquakes. (The theory is, of course, also applicable to a variety of physical processes, including shock waves in solids and ordinary phase changes.) In this regard we will investigate the constraints placed on the rate of failure by the conservation relations ("jump conditions") that must hold on the rupture boundary.

Finally, the representation of the radiation field which arises from stress relaxation around the failure zone is expressed in terms of a general Green's function solution. In order to obtain such a solution, the usual linearizing approximations are needed (e.g., the assumption of infinitesimal strains in the medium exterior to the failure zone), as well as some approximations that are unique to this problem. We will, however, develop an integral representation of the radiated field with the minimum number of assumptions in order to obtain general results.

2. Transport theorems and conservation equations

In a general continuum representation of material flow the conservation of a function of the flow F may be expressed as

$$\frac{dF}{dt} = \frac{d}{dt} \int_{V(t)} F(\underline{x},t)\, d^3x = \int_{V(t)} k(\underline{x},t)\, d^3x \quad , \tag{1}$$

where the source density has the general form

$$k(\underline{x},t) = K(\underline{x},t) + \nabla\cdot\ \underline{J}(\underline{x},t) \quad . \tag{2}$$

with $\underline{J}$ the flux of interacting fields and K corresponding to the intrinsic production of F in the volume $V(t)$.

Let $S(t)$ be the boundary of the material volume $V(t)$, let $\underline{V}(\underline{x},t)$ be the material velocity field, and assume that $V(t)$ is cut by a surface of discontinuity $\Sigma(t)$; moving with the velocity $\underline{U}(\underline{x},t)$, as illustrated in Figure 1. Let $[\![G]\!]_\Sigma$ denote the jump of a quantity G across Σ . Then the Reynolds transport theorem takes the form

$$\frac{d}{dt} \int_{V(t)} F(\underline{x},t)\, d^3x = \int_{V(t)\ominus\{V(t)\cap\Sigma(t)\}} \left[\!\!\left[\frac{\partial F}{\partial t} + \nabla_x\cdot(F\underline{V})\right]\!\!\right] d^3x$$

$$- \int_{V(t)\cap\Sigma(t)} [\![F(\ \underline{U}-\underline{V}\ )\cdot\ \hat{n}]\!]\, d\alpha \tag{3}$$

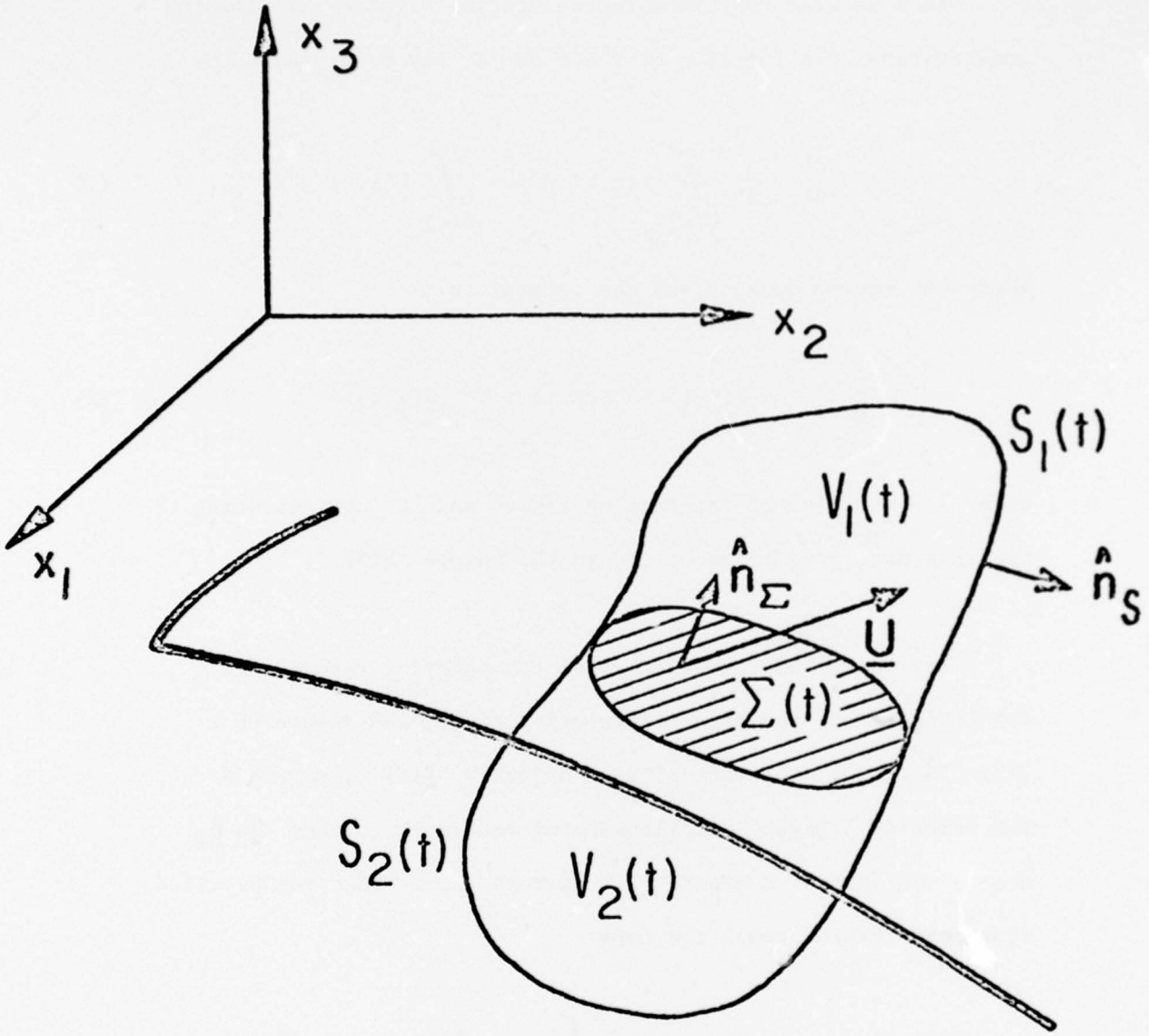

Figure 1. Case of a propagating discontinuity. $\Sigma(t)$ is the surface of discontinuity moving with velocity $\mathbf{U}$.

$S_1(t) + S_2(t)$ is a material surface, moving with the medium.

and Gauss's theorem takes the form

$$\int_{V\Theta\{\Sigma\cap V\}} \nabla\cdot\underline{J}\, d^3x + \int_{\Sigma\cap V} [\![\underline{J}\cdot\hat{n}]\!]\, da = \int_{S\Theta\{S\cap\Sigma\}} \underline{J}\cdot\hat{n}\, da \quad , \tag{4}$$

where Θ and $\cap$ denote the set theoretic difference and intersection respectively. A simplified proof of these results can be found, for example, in Eringen (1975). Edelen (1962) states a similar result to (4), but neglects to exclude the points of Σ from the volume integral, so that the term in $\underline{J}\cdot\hat{n}$ is effectively included twice in his result. Note that (3) and (4) hold only as long as none of the functions F, $\underline{v}$, $\underline{J}$ has a singularity on Σ stronger than a mere discontinuity (Minster, 1973). A detailed proof of these results can be obtained using the theory of distributions.

If generalized functions are used,

it is easy to see that (4) may, in fact, be written in the usual form

$$\int_V \nabla\cdot\underline{J}\, d^3x = \int_S \underline{J}\cdot\hat{n}\, da \quad . \tag{5}$$

Using (3), (4) in (1), (2), and noting that (1) holds for any volume $V(t)$, we have away from discontinuities

$$\frac{\partial F}{\partial t} + \nabla_x\cdot(F\underline{v}-\underline{J}) = K \quad , \tag{6}$$

which is the differential conservation equation. Since this has to hold at all points away from Σ, (1) reduces to

$$\int_{V(t)\cap\Sigma(t)} [\![F(\underline{V}-\underline{U})\cdot\hat{n}]\!]\, da = \int_{V(t)\cap\Sigma(t)} [\![\underline{J}\cdot\hat{n}]\!]\, da \tag{7}$$

so that, since $V(t)$ is arbitrary, we must have at all points on Σ

$$[\![F(\underline{V}-\underline{U})\cdot\hat{n}]\!]_{\Sigma} = [\![\underline{J}\cdot\hat{n}]\!]_{\Sigma} \quad , \tag{8}$$

which is the boundary condition to be satisfied on Σ for conservation of F.

A result of similar form has also been given by Freund (1970) in a somewhat different context. In a study by Snoke (1976), motivated by results equivalent to (8) given by Minster (1973), an attempt was made to obtain general "jump conditions" such as (8) by a method of transformation of the equation of motion to a moving coordinate frame. The approach does not contain the essence of the "moving boundary problem", however, namely the discontinuous behavior of the field variables, and yields results which are not conservation relations on the moving boundary surface. Burridge (1976), however, employs boundary conditions that are approximately the same as those given here for the special problem he considers.

If we define $\underline{V}^* = \underline{V}-\underline{U}$ as the velocity of the material, relative to the boundary Σ, and introduce the current density of F per unit time per unit area (flux vector): $\underline{F} = F\,\underline{V} - \underline{J}$, and the relative flux vector through Σ : $\underline{F}^* = F\,\underline{V}^* - \underline{J}$; then the conservation laws have the form

$$\frac{\partial F}{\partial t} + \frac{\partial F_\ell}{\partial x_\ell} = K \tag{9}$$

$$\left[\!\left[F^*_\ell \, n_\ell \right]\!\right]_\Sigma = 0 \tag{10}$$

where K is, as before, the rate of production of F per unit time per unit volume.

We observe that if the boundary Σ is a material surface, or if $\underline{V}^* \cdot \hat{n} = 0$, then (10) becomes

$$\left[\!\left[\underline{J} \cdot \hat{n} \right]\!\right]_\Sigma = 0 \tag{11}$$

which is the usual boundary condition when the boundaries move with material flow or deformation.

Conservation equations apply in general to tensor components, and it is straightforward to show that the general forms for (9) and (10) are

$$\left.\begin{aligned} &\frac{\partial F_{i\ldots j}}{\partial t} + \frac{\partial}{\partial x_m}\left[F_{i\ldots jm}\right] = K_{i\ldots j} \\ &\left[\!\left[F^*_{i\ldots jm}\, n_m \right]\!\right]_\Sigma = 0 \end{aligned}\right\} \tag{12}$$

Table 1 furnishes a summary of the most common conservation equations. Additional conservation equations are also possible, such as those investigated by Fletcher (1974) for hyperelastic media using Noether's theorem. The additional relations involve internal angular momentum for polar media, and since we are only concerned with nonpolar media, conservation of angular momentum only requires that the stress tensor T_{ij} be symmetric. Thus, equations (12), together with Table 1, provide the complete set of conservation relations for the media of importance in this study.

An alternative expression of the conservation equations in four dimensional form is also possible. We find such a compact representation to be useful when we consider integral representations of the linearized equations of motion for the continuum in a following section. Here we simply display the forms for the general (nonlinear) case.

In particular, the conservation relations can be put in a compact explicit form that expresses conservation of mass and momentum by introducing fields $F_{\alpha\beta}$ and K_{β} with the Greek indices running over the range 1 to 4. Thus, with space-time coordinates represented by x_{α} we have[†] for the momentum equation

---

[†]Here we retain a non-relativistic description, and merely consider time t as a fourth coordinate x_4 in the Newtonian sense. The summation convention over all repeated indices applies to both Greek and Roman indices.

TABLE 1

Conservation law	F	$\underline{F}$	$\underline{F}^*$	K
Mass	ρ	$\rho\underline{V}$	$\rho\underline{V}^*$	0
Momentum	ρV_i	$\rho V_i V_j - T_{ij}$	$\rho V_i V_j^* - T_{ij}$	ρb_i
Energy	$\rho E = \rho u + \rho/2\ V_\ell V_\ell$	$\rho E V_i - V_k T_{ki} + q_i$	$\rho E V_i^* - V_k T_{ki} + q_i$	$\rho b_k V_k + \rho h$
Total energy	$\rho \mathcal{E} = \rho E + \rho\phi$	$\rho \mathcal{E} V_i - V_k T_{ki} + q_i$	$\rho \mathcal{E} V_i^* - V_k T_{ki} + q_i$	ρh

where ρ = density

b_i = body force density

q_i = heat flux vector

ϕ = body force potential : $\underline{b} = -\nabla\phi$

T_{ij} = Cauchy stress tensor

u = internal energy density

h = heat source density

$$\frac{\partial F_{\alpha\beta}}{\partial x_\alpha} = K_\beta \qquad ; \qquad \alpha,\beta = 1,2,3,4 \tag{13a}$$

$$\left[\!\left[F^*_{\alpha\beta}\, n_\alpha \right]\!\right]_\Sigma = 0 \tag{13b}$$

where K_β and n_α are the "space-like" variables given by

$$K_\beta = (\rho b_1,\ \rho b_2,\ \rho b_3,\ 0) \equiv (\rho b_j\ ,\ 0)$$

$$n_\alpha = (n_1,\ n_2,\ n_3,\ 0) \equiv (n_j,\ 0) \tag{13c}$$

with Latin indices, such as j , running over the (space) indices 1, 2, 3 only. The vector $\underline{b}$ denotes the body force density, ρ the medium density, and the n_j are the components of the normal to any spatial surface in the medium. The fields $F_{\alpha\beta}$ and $F^*_{\alpha\beta}$ are given by:

$$F_{\alpha\beta} : \begin{cases} F_{ij} = \rho V_i V_j - T_{ij} & ; \quad i,j = 1,2,3 \\ F_{4j} = F_{j4} = \rho V_j & ; \quad j = 1,2,3 \\ F_{44} = \rho \end{cases} \tag{13d}$$

and

$$F^*_{\alpha\beta} : \begin{cases} F^*_{ij} = \rho V_i V^*_j - T_{ij} & ; \quad i,j = 1,2,3 \\ F^*_{4j} = F^*_{j4} = \rho V^*_j & ; \quad j = 1,2,3 \\ F^*_{44} = \rho \end{cases} \tag{13e}$$

Similarly, the energy conservation equation, defined in terms of $\mathcal{E}$ the total energy density function for the medium may be expressed as

$$\frac{\partial E_{\alpha\beta}}{\partial x_{\alpha}} = H_{\beta} \tag{14a}$$

where

$$E_{\alpha\beta}: \begin{cases} E_{ij} = 0 \quad , \quad i,j = 1,2,3 \\ E_{4j} = 0 \quad ; \quad j = 1,2,3 \\ E_{i4} = \rho \mathcal{E} V_i - V_j T_{ij} + q_i \quad ; \quad 1 = 1,2,3 \\ E_{44} = \rho \mathcal{E} \end{cases} \tag{14b}$$

and

$$H_{\beta} = (0, 0, 0, \rho h) \tag{14c}$$

The associated condition on Σ is:

$$\left[\left[E^{*}_{\alpha\beta} \, n_{\alpha} \right]\right]_{\Sigma} = 0 \tag{14d}$$

with

$$E^*_{\alpha\beta} : \begin{cases} E^*_{ij} = 0 \quad ; \quad i,j = 1,2,3 \\ E^*_{4j} = 0 \quad ; \quad j = 1,2,3 \\ E^*_{i4} = \rho \mathcal{E} v^*_i - V_j \, T_{ij} + q_i \quad ; \quad i = 1,2,3 \\ E^*_{44} = \rho \mathcal{E} \end{cases} \tag{14e}$$

It is easy to verify that the conservation relations given by (13) and (14) are the same as those obtained from equation (12) and Table 1.

3. Conservation Relations on Σ : Consequences for Failure Growth

The boundary conditions to be satisfied on Σ , which may be any boundary surface, are:

$$\left[\!\left[\rho \, V_i^* \, n_i \right]\!\right]_\Sigma = 0 \tag{15}$$

$$\left[\!\left[(\rho \, V_k \, V_i^* - T_{ki}) \, n_i \right]\!\right]_\Sigma = 0 \tag{16}$$

$$\left[\!\left[(\rho \, \mathcal{E} \, V_i^* - V_k \, T_{ki} + q_i) \, n_i \right]\!\right]_\Sigma = 0 \tag{17}$$

where the last equation can be trivially modified to include non-conservative body force fields using the results given in Table 1 along with equations (10) or (12).

These conditions may be recast in a more useful general form if one notes that $\left[\!\left[U_i \, n_i \right]\!\right]_\Sigma = 0$ and uses it in (10) to obtain

$$\left[\!\left[F \right]\!\right]_\Sigma U_i \, n_i = \left[\!\left[F_i \, n_i \right]\!\right]_\Sigma$$

From this equation we obtain, provided F has a nonzero jump across Σ :

$$U_i \, n_i = \frac{\left[\!\left[F \, V_i \, n_i \right]\!\right]_\Sigma - \left[\!\left[J_i \, n_i \right]\!\right]_\Sigma}{\left[\!\left[F \right]\!\right]_\Sigma} \tag{18}$$

The special condition of no growth of the failure zone is that no material transport occurs across Σ, in which case $\underset{\sim}{V}^{*} \cdot \hat{n} = 0$. We have seen earlier that this leads to equation (11). In this case (15) is satisfied identically, while from (16) and (17) we obtain, respectively

$$\left[\!\left[T_{ki}\, n_i \right]\!\right]_{\Sigma} = \left[\!\left[t_k \right]\!\right]_{\Sigma} = 0$$

$$\left[\!\left[V_k\, T_{ki}\, n_i \right]\!\right]_{\Sigma} = \left[\!\left[V_k \right]\!\right]_{\Sigma} t_k = \left[\!\left[q_i\, n_i \right]\!\right]_{\Sigma}$$

which are the well known boundary conditions at (ordinary) material boundaries. Note that the tangential velocity may be discontinuous on Σ inasmuch as slip along Σ is allowable.

More generally, investigation of (19) shows that slow boundary propagation is characterized by low values of the fluxes $\left[\!\left[J_i\, n_i \right]\!\right]_{\Sigma}$ and/or large values of $\left[\!\left[F \right]\!\right]_{\Sigma}$.

We are, however, most interested in "fast" processes. From the conservation of mass (15), we have[†]

$$U_i\, n_i = \frac{\left[\!\left[\rho\, V_i\, n_i \right]\!\right]}{\left[\!\left[\rho \right]\!\right]} \tag{19}$$

[†] In the following we will often simply write $[\![\ ]\!]$ for $[\![\ ]\!]_{\Sigma}$, where it is understood that the jump notation always applies to a surface Σ.

Let the unit normal to Σ point away from the failure zone, and, with reference to figure 1, let

$$\rho^{(1)} \equiv \rho(\Sigma^{(1)}) \quad , \quad \rho^{(2)} \equiv \rho(\Sigma^{(2)}) \quad , \quad [\![\rho]\!] \equiv \rho^{(1)} - \rho^{(2)}$$

where $\Sigma^{(1)}$ and $\Sigma^{(2)}$ denote Σ approached, in the limit, from region 1 and 2 respectively. With similar definitions for the other field variables, then (19) may be written as

$$U_R \equiv \left(U_i - V_i^{(1)}\right) n_i = \frac{\rho^{(2)}}{[\![\rho]\!]} \left[\!\left[V_i \; n_i\right]\!\right] \tag{20}$$

where U_R is the failure propagation velocity relative to the untransformed material. A large class of rapid processes of interest to us can be characterized by small fractional density jumps, since we expect material failure, involving macroscopic and microscopic fracture and cracking, plastic flow, grain boundary melting, etc ... to result in very small change in the average density. This kind of transition is precisely of greatest geophysical interest and in this case $[\![\rho]\!]$ is very small and U_R may be very large as a consequence.

We also observe that the momentum equation (16) may be written in the form

$$- U_R \left[\!\left[\rho \; V_k\right]\!\right] + \rho^{(1)} \; V_k^{(1)} \left[\!\left[V_i \; n_i\right]\!\right] - \left[\!\left[\rho \; V_k\right]\!\right] \left[\!\left[V_i \; n_i\right]\!\right] = \left[\!\left[T_{ki} \; n_i\right]\!\right]$$

Eliminating the jump $[\![V_i\ n_i]\!]$ by use of (20), we have

$$\rho^{(1)}\ [\![V_k]\!]\ U_R = -\ [\![t_k]\!] \tag{21}$$

and this relation is exact. When the density jump $[\![\rho]\!]$ is small, then we have $\rho^{(1)} \simeq \rho^{(2)}$ and so, as an approximation

$$[\![\rho\ V_k]\!]\ U_R = -\ [\![t_k]\!] \tag{22}$$

Precisely the same approximate result is obtained from (16) if we consider $U_i\ n_i >> V_i\ n_i$, which serves as the definition of a fast transition process. Then $V_i\ n_i$ can be neglected in (16), and we get (22) directly, with $U_R \simeq U_i\ n_i$. Equation (22) will be used extensively in later sections where we consider a "representation theorem" for the radiated elastic field associated with a growing failure zone.

We note that typical inferred values for (shear) stress drops and rupture velocities for earthquakes are of the order 10^8 dynes/cm^2 and 3×10^5 cm/sec respectively. With a density near 3.5 gm/cm^3, then (21) gives $[\![V_k]\!] \sim 10^2$ cm/sec. Thus, (21) implies tangential particle velocity jumps near 1 m/sec across the failure boundary.

The energy equation (17) can also be put into a more appropriate form for the present application. In particular, eliminating $[\![V_i\ n_i]\!]$ using (20), gives

$$-\ \rho^{(1)}\ U_R [\![\hat{\mathcal{E}}]\!] = [\![(V_k\ T_{ki} - q_i)\ n_i]\!] \tag{23}$$

Here

$$[\![\mathcal{E}]\!] = [\![u]\!] + 1/2 \left[\!\left[V_k\, V_k\right]\!\right] + [\![\phi]\!]$$

where u is the internal energy and ϕ the body force potential energy. The second term is the change in the kinetic energy density of the material across the boundary. We can realistically neglect the change in ϕ across a failure boundary compared with the change in the kinetic or internal energies.

The change in the internal energy may be viewed as the energy required for the transition process in the material since we may consider the medium on either side of Σ at a given time as two states of the same material. Viewed in this manner we observe that, while the transition is irreversible, we can nevertheless consider u to be a function of the ordering in the material, that is the entropy, and the strain energy density. In the transition process we would expect a decrease in the ordering upon failure, that is an increase in the disorder and in the entropy, while the strain energy density (i.e., the recoverable or reversible energy) should decrease. (Here, of course, the measure of strain is relative to the two distinctly different natural states of the material in question, while the difference in the ordering in these two states is measured by the change in the entropy.) Therefore we let

$$[\![u]\!] = L \tag{24}$$

with L the internal energy change associated with the specific process taking place in the material; where L is used to emphasize the fact that the quantity $[\![u]\!]$ is characteristic of the process for the material and hence a material property. We note that, because of the definition of $[\![u]\!] = u^{(1)} - u^{(2)}$, we expect the change in u across Σ due to disordering of the material to be negative, while the part of the change due to the strain energy positive. Thus the total change, being the sum of these, may in principle be positive or negative. We will show, however, that for a spontaneous process to occur along with rapid growth of the transition zone, then it is generally necessary that L be positive. In particular, if the spatial heat flux jump across Σ is neglected (i.e., if the change in the thermal gradient and possible changes in the thermal coefficient across Σ are neglected as small compared with the other effects), then L must always be positive. In general, for failure processes we expect terms like $[\![V_k\ t_k]\!]$ in (23) to be much larger in magnitude than the term $[\![q_k\ n_k]\!]$, and this size ordering also leads to the requirement that L be positive for non-zero growth rate of a spontaneous failure zone. A requirement that L be positive simply means that the change in the strain energy must generally be larger in magnitude than that part of the internal energy change due solely to disordering. This requires relatively high (nonhydrostatic) strain energy for such a process to occur.

To show that these statements follow from the condition (23), we can rewrite it as

$$U_R = - \frac{\left[\left[V_k \; t_k - q_k \; n_k \right]\right]}{\rho\left(L + 1/2 \left[\left[V_k \; V_k \right]\right]\right)} \tag{25}$$

where we consider the case in which the denominator is non-zero, of course. Here we have suppressed the superscript on the density, $\rho^{(1)}$, and simply written ρ to denote this quantity. Using (21) in this equation, after expanding both $\left[\left[V_k \; t_k \right]\right]$ and $\left[\left[V_k \; V_k \right]\right]$, we have the results:

$$U_R = - \frac{\left[\left[V_k \right]\right] t_k^{(1)} - \left[\left[q_k \; n_k \right]\right]}{\rho\left[L + 1/2 \left[\left[V_k \right]\right]\left[\left[V_k \right]\right]\right]} = - \frac{\left[\left[V_k \right]\right] t_k^{(2)} - \left[\left[q_k \; n_k \right]\right]}{\rho\left[L - 1/2 \left[\left[V_k \right]\right]\left[\left[V_k \right]\right]\right]} \tag{26}$$

Using (21) again, in either of the expressions for U_R in (26), to eliminate terms in $\left[\left[V_k \right]\right]$, we get:

$$U_R^2 - \frac{\left[\left[q_k \; n_k \right]\right]}{\rho L} U_R - \frac{\left[\left[t_k \; t_k \right]\right]}{2 \rho^2 L} = 0 \tag{27}$$

The roots of this quadratic in U_R are real provided

$$\left[\left[q_k \; n_k \right]\right]^2 + 2L \left[\left[t_k \; t_k \right]\right] \geq 0 \tag{28}$$

When this condition is not met, then U_R has complex (or imaginary) roots and this means that initiation and growth of the transition process cannot occur.

When the stresses, and hence the tractions, drop upon failure, then $\left[\!\left[t_k \; t_k \right]\!\right] > 0$, and the scalar terms involving the jumps on Σ are all positive. In this case we must have

$$L \geq - \frac{\left[\!\left[q_k \; n_k \right]\!\right]^2}{2 \left[\!\left[t_k \; t_k \right]\!\right]} \leq 0 \tag{28a}$$

As was already noted, for a failure process we expect the heat flux term to be much smaller than the traction term so that, for all practical purposes, we must have

$$L \geq 0$$

If we neglect the heat flux term completely on the grounds of its relative size for a rapid spontaneous failure process, then (27) gives

$$U_R \simeq \sqrt{\frac{\left[\!\left[t_k \; t_k \right]\!\right]}{2\rho^2 L}} \tag{29}$$

Alternately, under these circumstances

$$L \simeq \frac{\left[\!\left[t_k \; t_k \right]\!\right]}{2\rho^2 U_R^2} \tag{30}$$

We note that rapid growth of a tectonic failure zone involves $U_R \simeq 3 \times 10^5$ cm/sec and traction jumps at the front of the failure boundary which appear to be of the order of 10^8 to 10^9 dynes/cm^2

(e.g., Archambeau, 1976). This implies that the internal energy change L is in the range from 10^4 to 10^6 ergs/gm.

We can also express L in terms of the particle velocity and traction changes across Σ when we neglect the heat flux term. That is, eliminating U_R^2 from (30), using (21), gives:

$$L = 1/2 \left[\!\left[V_k \right]\!\right] \left[\!\left[V_k \right]\!\right] \left\{ \frac{\left[\!\left[t_k \; t_k \right]\!\right]}{\left[\!\left[t_k \right]\!\right] \left[\!\left[t_k \right]\!\right]} \right\} \tag{31}$$

The ratio of the quadratics in traction in (31) will be near unity when the hydrostatic stress is maintained after failure (i.e., small specific volume change and density change) and when the deviatoric stresses nearly vanish upon failure--that is when there is nearly a complete loss of shear strength upon failure. It is quite possible that this situation would prevail for many, if not most, earthquakes. If this is the case then

$$L \simeq 1/2 \left[\!\left[V_k \right]\!\right] \left[\!\left[V_k \right]\!\right] \tag{31a}$$

With L in the range 10^4 to 10^6 ergs/gm then this implies a magnitude of from 1 to 10 m/sec for particle velocity jumps across the failure surface and conversely.

If the heat flux term can be neglected, that is if $| [\![q_k \; n_k]\!] | << | [\![V_k \; t_k]\!] |$, then the energy relation (23) or (25) may be expressed as

$$U_R = - \frac{[\![V_k \; t_k]\!]}{\rho\left(L + 1/2 \; [\![V_k \; V_k]\!]\right)}$$

If we use the expression (31) for L in this, then we find that this expression of energy conservation can be put in the form:

$$\left(\rho \; U_R \; [\![V_k]\!] - [\![t_k]\!]\right)[\![t_k]\!] = 0$$

In view of the relation (21) for U_R, we see that this equation is satisfied when momentum is conserved.

Therefore this shows that if $[\![q_k \; n_k]\!] << [\![V_k \; t_k]\!]$, then conservation of energy is insured when equation (31) (or (31a)) is satisfied along with momentum conservation--which is expressed by equation (21). Consequently, the equations for failure zone growth seem to be well approximated by the relations

$$\left.\begin{aligned} \rho \; U_R \; [\![V_k]\!] &= - \; [\![t_k]\!] \\ L \; [\![t_k]\!] \, [\![t_k]\!] &= 1/2 \; [\![V_k]\!] \, [\![V_k]\!] \left\{[\![t_k \; t_k]\!]\right\} \end{aligned}\right\} \qquad (32)$$

If we treat L as a material property, then the second of these relations can be viewed as a condition for failure growth--that is when the particle velocities and tractions across the failure boundary are such that this relation is satisfied for a value of L appropriate to a specific failure mode of the material, then growth may occur; with the rate of growth then given by the first relation in (32). In at least some instances of rapid failure the shear tractions would be very small within the failure zone, and then, as previously noted, the second relation reduces to $L \simeq 1/2 \left[\!\left[V_k\right]\!\right] \left[\!\left[V_k\right]\!\right]$.

Thus we may view the second relation in (32) as a dynamic failure condition and the first relation as an equation for U_R , the dynamic growth rate.

The dependence of the rupture growth rate--or rupture velocity U_R--on the rheological properties of the material can be inferred from the first relation in (32) if we specify appropriate constitutive relations for the material in its two states, before and after failure has taken place. A constitutive relation of sufficient generality to describe the local behavior of the material after failure is of the form (e.g., Fung 1965)

$$T_{ij} = \sum_{\alpha} \int_0^t e^{-\Omega_\alpha (t-\tau)} \, D^{(\alpha)}_{ijk\ell} \, e_{k\ell}(\tau) \, d\tau$$

$$+ C_{ijk\ell} \, e_{k\ell} + C'_{ijk\ell} \frac{\partial e_{k\ell}}{\partial t} \qquad (33)$$

where the term involving the sum over α arises from relaxation processes within the material, of which there may be N types each denoted by an index α . Here Ω_α is a relaxation frequency (reciprocal relaxation time), and the object $D^{(\alpha)}_{ijk\ell}$ is a time independent relaxation modulus (or "relaxation strength") tensor.

Relaxation terms can be shown to result from a variety of processes, including the movement of interstitial atoms, and vacancies, twining, chemical reactions, crystalline thermal currents and dislocation motion. Descriptions of typical physical processes of this type for solids and liquids are given, for example, by De Groot and Mazur (1969) and Mason (1966).

The second term in (33) is a linear elastic term, while the last term is a simple linear viscous term.

The strain $e_{k\ell}$ is defined as an infinitesimal strain measured from the completely relaxed state[†] of the material *after* transition. Thus, in the infinitesimal strain approximation which we will adopt for the material after transition:

$$e_{k\ell} = u^{(2)}_{(k,\ell)} = 1/2\left(\frac{\partial u^{(2)}_k}{\partial x_\ell} + \frac{\partial u^{(2)}_\ell}{\partial x_k}\right) \tag{34}$$

where $u^{(2)}_k$ is a displacement from the relaxed reference state.

[†]By relaxed state we mean the equilibrium configuration taken by a piece of the material removed from the surrounding medium, so that it is free from external forces and surface tractions.

A similar constitutive relation holds for the material outside the failure zone or for the material before failure. However, the relaxed state of this material is different from that for the failed material, so that the infinitesimal strain is defined as

$$e_{k\ell} = u^{(1)}_{(k,\ell)} \equiv 1/2\left(\frac{\partial u^{(1)}_k}{\partial x_\ell} + \frac{\partial u^{(1)}_\ell}{\partial x_k}\right) \tag{35}$$

with $u^{(1)}_k$ the displacement measured relative to the relaxed state of the unfailed material.

Further, while the form of the constitutive relation may be the same for the material in the two states, the moduli $D^{(\alpha)}_{ijk\ell}$, $C_{ijk\ell}$ and $C'_{ijk\ell}$ would be very different. For the unfailed material we can, in the present context at least, neglect the anelastic moduli $D^{(\alpha)}_{ijk\ell}$ and viscous term $C'_{ijk\ell}$ relative to the linear elastic term $C_{ijk\ell}$ for the unfailed material. Thus for the region outside the failure zone we may use a constitutive relation of the form

$$T_{ij} = C_{ijk\ell}\, e_{k\ell} \tag{36}$$

with $e_{k\ell}$ defined by (35). In any case, however, (33) can be used to represent the form of the constitutive equation in both the failed and unfailed material, with the coefficients and strains taking on different values in the two zones.

We can write (33) in the compact operational form

$$T_{ij} = M_{ijk\ell}\, e_{k\ell} \tag{37}$$

where $M_{ijk\ell}$ is the integral operator

$$M_{ijk\ell} = \sum_{\beta=1} m^{(\beta)}_{ijk\ell} \int_0^t dt'\, e^{-\Omega_\beta (t-t')} \Big[(1-\delta_{1\beta})(1-\delta_{2\beta}) + \delta_{1\beta}\delta(t-t') + \delta_{2\beta}\, \delta_1(t-t') \Big] \tag{38}$$

with $\delta_{\alpha\beta}$ denoting the Kronecker delta, while $\delta(t-t')$ is a Dirac delta function and $\delta_1(t-t')$ its derivative. Here $m^{(\beta)}_{ijk\ell}$ is a time independent modulus tensor, equal to the elastic and viscous tensors for $\beta = 1,2$ and equal to the set of relaxation moduli tensors for $\beta = 3,4 \ldots$.

We can also write (38) as

$$M_{ijk\ell} = \sum_{\beta} m^{(\beta)}_{ijk\ell}\, I_\beta \tag{39}$$

where I_β is the time dependent integral operator in (38).

Now the momentum condition in (32) can be written as

$$\rho\, U_R \left[\!\left[V_k \right]\!\right] = - \left[\!\left[t_k \right]\!\right] = - \sum_{\beta} \left[\!\left[m^{(\beta)}_{ijk\ell}\, I_\beta\, e_{ij} \right]\!\right] n_\ell \tag{40}$$

Without undue loss of generality, we will consider the isotropic case. This gives

$$m^{(\beta)}_{ijk\ell} = \lambda_\beta \, \delta_{ij} \, \delta_{\ell k} + \mu_\beta(\delta_{i\ell} \, \delta_{jk} + \delta_{ik} \, \delta_{j\ell})$$

for the modulus tensor.

If we now define a signal velocity C_S to be associated with the rate at which changes in the displacement fields are propagated, in the sense that displacements are causal with respect to such a velocity, then

$$u_k^{(n)} \equiv u_k^{(n)}(\tau) \tag{41}$$

where $n = 1,2$ for the two material states, and $\tau \equiv t - r/C_S$ with $r \equiv (x_j \, x_j)^{1/2}$. Then we have:

$$\frac{\partial u_k^{(n)}}{\partial x_\ell} = -\frac{1}{C_S}\left(\frac{x_\ell}{r}\right)\frac{\partial u_k^{(n)}}{\partial \tau}$$

Since we can use the infinitesimal strain approximation for the material in its initial (unfailed) and final (failed) states, then the reduced time derivative of u_k is also the particle velocity. Thus

$$\left.\begin{aligned} \frac{\partial u_k^{(n)}}{\partial \tau} &= \frac{\partial u_k^{(n)}}{\partial t} = V_k^{(n)} \\ \frac{\partial u_k^{(n)}}{\partial x_\ell} &= -\frac{1}{C_S}\left(\frac{x_\ell}{r}\right) V_k^{(n)} \end{aligned}\right\} \tag{42}$$

Using (42) in the momentum condition yields

$$\rho\, U_R \left[\!\left[V_k \right]\!\right] = \sum_\beta I_\beta \left\{ \left[\!\left[\frac{\lambda_\beta}{C_S} V_i \right]\!\right] \frac{x_i}{r} n_k + \left[\!\left[\frac{\mu_\beta}{C_S} \left\{ V_k \left(\frac{x_\ell}{r} \right) + V_\ell \left(\frac{x_k}{r} \right) \right\} n_\ell \right]\!\right] \right\} \tag{43}$$

for the isotropic case. The magnitude of U_R is thus directly proportional to the changes in the material moduli upon failure.

For example, suppose the material has the properties of a perfect fluid after transition. If the jump in the normal component of velocity across the transition boundary is small compared with the jump in the tangential components of the velocity (i.e., small changes in density and compressibility) then we have as an approximation to the maximum magnitude of U_R :

$$|U_R| \simeq \left[\!\left[\frac{\mu}{\rho C_S} V_k \right]\!\right] / \left[\!\left[V_k \right]\!\right]$$

considering the failure process to be driven by a shear wave, so that $C_S \simeq V_S$ with $V_S = \sqrt{\mu/\rho}$ the shear velocity in the medium before failure and since $\mu = 0$ for an ideal fluid, then:

$$|U_R| \simeq V_S$$

In conclusion then, it is evident that the form of (43) indicates a dependence of the failure rate on the transition process in terms of the changes in material moduli. In general we see that consideration of an expression like (40) is required in order to obtain a precise estimate

of the magnitude and space-time dependence of U_R . Nevertheless, simplified expressions such as (43) and approximate results, such as that for the ideal fluid transition, are quite useful and can provide a basis for interpretation of observed failure rates.

4. Linearization of the Coupled Conservation Equations

We will now focus our attention on the medium outside the failure zone and express the conservation relations in this region in linearized form, using the usual approximation of infinitesimal strain for this region. This will give linear equations of motion for this part of the medium when we take the material to be elastic and specify the rheology according to (34).

We note that we can also describe the dynamical behavior of the medium within the failure zone itself *after* failure using linear theory, if we adopt (33) as an adequate description of the rheology. In this case we would simply repeat the arguments leading to linearized equations and obtain an integral Green's function solution in a manner analogous to that for the region outside the failure zone. The two integral representations of the medium response would then be connected by the boundary conditions on the failure surface--as given by the equations (32) in the previous section. In this development, however, we will only consider the exterior region. This does not result in any loss of generality in the analytical description of the radiation field since the dynamical behavior of the interior medium manifests itself directly in the boundary conditions for the exterior problem, and these can be treated in a formal manner with the tractions and the particle velocity of the interior zone material at the failure boundary being left completely arbitrary. The resulting general integral representation for the exterior radiation field can then be

evaluated for particular cases when the rheological properties of the material after transition are independently specified. Then the resulting dynamical variation of the boundary surface tractions and the particle velocity are determined by either solving for the interior deformation fields using the Green's function representation or by choosing a simple, yet adequate, rheological description for which the dynamical behavior in the interior is known with sufficient accuracy a priori. An example of the latter would be the assumption of melting and the production of an essentially inviscid interior fluid, so that the shear tractions in the interior would vanish and the particle velocity would only reflect any accompanying density change.

To treat the exterior region we first observe that, in the present context, it may be viewed as containing an elastic material. In this case the energy equations are trivially satisfied in the medium away from the failure boundary if we neglect heat transport and transport terms in the energy equation. On the failure boundary, however, energy is absorbed by the failure process and energy conservation is expressed, approximately, by the second relation in (32).

The linearized equations of motion for the exterior medium can be written in the form

$$\frac{\partial}{\partial t}\left(\rho \frac{\partial u_i}{\partial t}\right) = \frac{\partial}{\partial x_j}\left[C_{ijk\ell} \frac{\partial u_k}{\partial x_\ell}\right] + \rho b_i \qquad (44)$$

where u_i is the elastic displacement, and both the density ρ and the elastic tensor $C_{ijk\ell}$ are treated as functions of the spatial coordinates alone.† In obtaining (43) we have used the symmetry relations (e.g., Landau and Lifschitz, 1965):

$$C_{ijk\ell} = C_{jik\ell} = C_{ij\ell k} = C_{k\ell ij}$$

Because of the form of (44), we can write these linearized equations of motion in the same four dimensional form as was used to express all the conservation relations earlier. Specifically, we define an "elastic-inertial tensor" as:

$$C_{\alpha\beta\gamma\delta} : \begin{cases} C_{\alpha\beta\gamma\delta} = - C_{ijk\ell} & ; \quad \alpha,\beta,\gamma,\delta = 1,2,3 \\ C_{i4k4} = C_{4i4k} = \rho\, \delta_{ik} & ; \quad i,k = 1,2,3 \\ C_{\alpha\beta\gamma\delta} = 0 & ; \quad \text{otherwise} \end{cases} \tag{45}$$

where $C_{\alpha\beta\gamma\delta}$ is seen to have the symmetry properties

$$C_{\alpha\beta\gamma\delta} = C_{\beta\alpha\gamma\delta} = C_{\alpha\beta\delta\gamma} = C_{\gamma\delta\alpha\beta} \tag{46}$$

---

†In what follows, we use the common notation

$$u_{k,\ell} \equiv \frac{\partial u_k}{\partial x_\ell} \quad ; \quad u_{k,\ell m} \equiv \frac{\partial^2 u_k}{\partial x_\ell \, \partial x_m} \quad ; \text{ etc.}$$

for partial derivatives.

with the Greek indices ranging from 1 to 4. If we also define the spacelike fields

$$\left.\begin{aligned} u_\alpha &\equiv (u_1, u_2, u_3, 0) \\ f_\alpha &\equiv (b_1, b_2, b_3, 0) \end{aligned}\right\} \tag{47}$$

then (44) can be written in the form

$$\left.\begin{aligned} \tau_{\alpha\beta,\beta} &= \rho f_\alpha \\ \tau_{\alpha\beta} &= C_{\alpha\beta\gamma\delta}\, u_{\gamma,\delta} \end{aligned}\right\} \tag{48}$$

Alternately, in a form convenient for a solution for the displacement field u_γ, the equations of motion may be expressed in the operator form:

$$L_{\alpha\gamma}\, u_\gamma = \rho f_\alpha \tag{49}$$

where the "elastic operator" is given by[†]

$$L_{\alpha\gamma} \equiv \frac{\partial}{\partial x_\beta}\left(C_{\alpha\beta\gamma\delta}\, \frac{\partial}{\partial x_\delta}\right) \tag{50}$$

[†]Kupradze, 1963, defines the "elastic operator" in an analogous fashion in the frequency domain.

The boundary conditions can also be expressed in terms of the elastic-inertial tensor defined in (45) and the spacelike displacement field u_γ if we define a four dimensional space-time "normal" as

$$\eta_\alpha = (n_1, n_2, n_3, - \underline{U}^* \cdot \hat{n}) \tag{51}$$

with

$$U^*_\ell = U_\ell - V_\ell$$

where n_j is the regular spacelike normal to any spatial surface in the medium, in particular the surface Σ, and $\underline{U}^* \cdot \hat{n} = U_R$ is the projection of the spacelike relative velocity vector for the surface Σ along the normal to the surface. Now we observe that in view of the properties of the elastic-inertial tensor

$$\left[\!\left[\tau_{\alpha\beta} \, \eta_\beta \right]\!\right]_\Sigma = \left[\!\left[C_{\alpha\beta\gamma\delta} \, u_{\gamma,\delta} \, \eta_\beta \right]\!\right]_\Sigma = - \left[\!\left[C_{k\ell mn} \, u_{m,n} \, n_\ell + \rho \, u_{k,4} \, U^*_\ell \, n_\ell \right]\!\right]_\Sigma$$

or

$$\left[\!\left[\tau_{\alpha\beta} \, \eta_\beta \right]\!\right]_\Sigma = \left[\!\left[(\rho \, V_k \, V^*_\ell - T_{k\ell}) \, n_\ell \right]\!\right]_\Sigma$$

but the right side expresses conservation of momentum on Σ, as is verified from (16), and vanishes. Thus we have that

$$\left[\!\left[\tau_{\alpha\beta}\ \eta_\beta \right]\!\right]_\Sigma = 0$$

for all α and β.

Thus the linearized equations for the exterior region are most naturally expressed in a four vector form, as:

$$\left.\begin{aligned} L_{\alpha\gamma}\ u_\gamma = \tau_{\alpha\beta,\beta} &= \rho f_\alpha \\ \left[\!\left[\tau_{\alpha\beta}\ \eta_\beta \right]\!\right]_\Sigma &= 0 \end{aligned}\right\} \qquad (52)$$

with the inertial-stress tensor $\tau_{\alpha\beta}$ given by (48) and where the elastic operator $L_{\alpha\gamma}$ is defined by (50). In the following we will linearize the boundary condition in (52) to the extent that we will use U_ℓ instead of U_ℓ^*, which amounts to the neglect of V_ℓ compared with U_ℓ, as is justified for failure processes.

5. Green's Tensor Equations for the Radiation Field in the Elastic Zone: Elastodynamic Representation Theorems

The differential operator $L_{\alpha\gamma}$ applies to space-like tensors (*i.e.*, tensors without time-like components) with the property,

$$w_{\alpha\beta\ldots\lambda} = w_{\alpha\beta\ldots\lambda}\,(1-\delta_{\alpha 4})\cdots(1-\delta_{\lambda 4})$$

The contraction $L_{\mu\alpha}\, w_{\alpha\beta\ldots\lambda}$ is another space-like tensor. The operator has been defined in a four dimensional space-time, and it is useful to consider an arbitrary four volume Ω in this space over which an inner product of space-like tensors is defined. Thus, given two space-like tensors $g_{\alpha\ldots\lambda}$ and $h_{\beta\ldots\mu}$, we define an inner product in Ω by

$$(g_{\alpha\ldots\lambda}\ ,\ h_{\beta\ldots\mu})_{\Omega} \equiv \int_{\Omega} g_{\alpha\ldots\lambda}\ h_{\beta\ldots\mu}\ d^4x$$

Here $(g_{\alpha\ldots\lambda}\ ,\ g_{\alpha\ldots\lambda})$ is positive and vanishes only when $g_{\alpha\ldots\lambda} \equiv 0$. Let $G_{\alpha}^{\beta}(\underline{x},\ x')$ denote a two point tensor, a function of the independent coordinates $\underline{x}$ and $\underline{x}'$ in Ω, then we define the inner products[†]

$$(G_{\alpha}^{\beta}\ ,\ u_{\alpha})_{\Omega}^{\underline{x}'} \equiv \int_{\Omega} G_{\alpha}^{\beta}(\underline{x},\ \underline{x}')\ u_{\alpha}(\underline{x}')\ d^4x'$$

$$(G_{\alpha}^{\beta}\ ,\ u_{\alpha})_{\Omega}^{\underline{x}} \equiv \int_{\Omega} G_{\alpha}^{\beta}(\underline{x},\ \underline{x}')\ u_{\alpha}(\underline{x})\ d^4x$$

[†] We will use, as a notational convenience, both superscript and subscript indices for the tensors appearing here. However, all tensors are Cartesian and there is no distinction between covariant or contravariant tensors.

which give a vector function of $\underline{x}$ in the first case or a vector function of $\underline{x}'$ in the second. If G^{β}_{α} is symmetric in $\underline{x}$ and $\underline{x}'$, then the two inner product forms are entirely equivalent.

The Green's functions associated with the operator $L_{\alpha\gamma}$ are two point tensors that are of special importance in the present development. In particular, we define the two point Green's tensor associated with $L_{\alpha\gamma}$ to be given by

$$L_{\alpha\gamma}\, G^{\beta}_{\gamma}(\underline{x}, \underline{x}_0) = \Delta^{\beta}_{\alpha}(\underline{x}, \underline{x}_0) \tag{53}$$

where the space-like tensor G^{β}_{γ} is a fundamental solution of the operator $L_{\alpha\gamma}$ with a pole at $\underline{x}_0$; with the space-like tensor Δ^{β}_{α} defined to be the generalized delta function:

$$\Delta^{\beta}_{\alpha} \equiv 4\pi\, \delta_{\alpha\beta}(1 - \delta_{\alpha 4})(1 - \delta_{\beta 4})\, \delta(\underline{x} - \underline{x}_0)$$

Here $\delta(\underline{x} - \underline{x}_o)$ is the (four-dimensional) Dirac delta distribution. Clearly G^{β}_{γ} defined by (53) will have a singularity at $\underline{x} = \underline{x}_o$ due to the presence of the Dirac delta distribution and therefore will satisfy (53) in a distributional sense (see for example: Stakgold, 1968). In the present context $G^{\beta}_{\gamma}(\underline{x}, \underline{x}_o)$ can be viewed as the γ component of the displacement field in the continuum at $\underline{x}$ due to an impulsive force in the β direction located at $\underline{x}_o$. Consequently $\underline{x}_o$ can be thought of as the source point and $\underline{x}$ as the receiver or observer point.

With these definitions of the inner product in Ω for space-like tensors we can generate integral equations that

are equivalent to the differential equations and associated boundary conditions which specify the displacement field u_γ in a continuum. To do so we will make use of the special properties of the Green's function.

In particular, the Green's theorem in Ω is obtained by considering the inner product

$$(L\,\underline{w},\,\underline{v})_\Omega \equiv \int_\Omega v_\alpha\, L_{\alpha\gamma}\, w_\gamma\, d^4x \tag{54}$$

where the operator L is simply the matrix operator with components given in (49), while $\underline{w}$ and $\underline{v}$ are fields satisfying either of the operator equations (48) or (53) and hence may be single or two point space-like tensors of first or second order.

Now using the representation of the components of L given in (49) we have

$$(L\underline{w}\,,\,\underline{v})_\Omega \equiv \int_\Omega v_\alpha\, (C_{\alpha\beta\gamma\delta}\, w_{\gamma,\delta})_{,\beta}\, d^4x \tag{55}$$

A result similar to the ordinary Green's theorem is obtained by first observing that the integrand can be expressed in terms of an identity as:

$$v_\alpha\, (C_{\alpha\beta\gamma\delta}\, w_{\gamma,\delta})_{,\beta} = (v_\alpha\, C_{\alpha\beta\gamma\delta}\, w_{\gamma,\delta})_{,\beta} - v_{\alpha,\beta}\, C_{\alpha\beta\gamma\delta}\, w_{\gamma,\delta}$$

However the final term can be rewritten by using the symmetry properties of $C_{\alpha\beta\gamma\delta}$, so that

$$-v_{\alpha,\beta}\, C_{\alpha\beta\gamma\delta}\, w_{\gamma,\delta} = w_\alpha (C_{\alpha\beta\gamma\delta}\, v_{\gamma,\delta})_{,\beta} - (w_\alpha\, C_{\alpha\beta\gamma\delta}\, v_{\gamma,\delta})_{,\beta}$$

Using these results in (55) we get

$$(L\,\underline{w},\underline{v})_{\Omega}^{x} = \int_{\Omega} [w_\alpha (C_{\alpha\beta\gamma\delta}\, v_{\gamma,\delta})_{,\beta}]\, d^4x$$

$$+\int_{\Omega} [(v_\alpha\, C_{\alpha\beta\gamma\delta}\, w_{\gamma,\delta} - w_\alpha\, C_{\alpha\beta\gamma\delta}\, v_{\gamma,\delta})_{,\beta}]\, d^4x \qquad (56)$$

We can now define a formal adjoint operator L^*, where

$$L^*_{\alpha\gamma} \equiv \frac{\partial}{\partial x_\beta} \left(C_{\alpha\beta\gamma\delta}\, \frac{\partial}{\partial x_\delta}\right) \qquad (57)$$

are the matrix elements of L^* and further define the bilinear concomitant J_β of $\underline{w}$ and $\underline{v}$ where

$$J_\beta \equiv v_\alpha\, C_{\alpha\beta\gamma\delta}\, w_{\gamma,\delta} - w_\alpha\, C_{\alpha\beta\gamma\delta}\, v_{\gamma,\delta} \qquad (58)$$

in order to write (56) in the form

$$(L\underline{w}\,,\underline{v})_{\Omega}^{x} = (\underline{w}, L^*\underline{v})_{\Omega}^{x} + \int_{\Omega} J_{\beta,\beta}\, d^4x \qquad (59)$$

This is the generalized Green's theorem for the operator L in Ω.

We observe from comparison of (57) with (49) that

$$L^* \equiv L$$

and hence that L is formally self adjoint.

In deriving (59) we have considered the operation of L on fields specified at $\underline{x}$ and have formed inner products on Ω with respect to the coordinates $\underline{x}$. We may form inner products with respect to fields specified at the coordinates $\underline{x}_o$, which in the case of two point tensor fields such as $G^{\beta}_{\gamma}(\underline{x}, \underline{x}_o)$ means integrating over the "source coordinates" $\underline{x}_o$ rather then the "observer coordinates" $\underline{x}$. In formal terms we may generate a completely parallel result to (59). Consider the operator $L^{(o)}$ defined by

$$L^{(o)}_{\alpha\gamma} \equiv \frac{\partial}{\partial x^o_\beta} \left(C_{\alpha\beta\gamma\delta} \frac{\partial}{\partial x^o_\delta} \right) \tag{60}$$

in component form. Now

$$L^{(o)}_{\alpha\gamma} u_\gamma = \frac{\partial}{\partial x^o_\beta} \left(C_{\alpha\beta\gamma\delta}(\underline{x}_o) \frac{\partial u_\gamma}{\partial x^o_\delta} \right)$$

is just the operation of L on $\underline{u}$ at $\underline{x}_o$. Here of course u_γ is expressed as a function of the coordinates $\underline{x}_o$. In case the operand is a two point tensor G^{β}_{γ}:

$$L^{(o)}_{\alpha\gamma} G^{\beta}_{\gamma}(\underline{x}_o; \underline{x}) = \frac{\partial}{\partial x^o_\beta} \left[C_{\alpha\beta\gamma\delta}(\underline{x}_o) \frac{\partial G^{\beta}_{\gamma}(\underline{x}_o; \underline{x})}{\partial x^o_\delta} \right]$$

Clearly we can now form the inner product

$$(L^{(o)}\,\underline{w},\,\underline{v})_{\Omega}^{\underline{x}_o} \equiv \int_{\Omega} v_\alpha\, L^{(o)}_{\alpha\gamma}\, w_\gamma\, d^4x^o \tag{61}$$

By exactly the same formal manipulations used to obtain the previous result, we have the complementary Green's theorem in Ω for $L^{(o)}$:

$$(L^{(o)}\underline{w}\,,\,\underline{v})_{\Omega}^{\underline{x}_o} = (\,\underline{w}, L^{(o)*}\,\underline{v})_{\Omega}^{\underline{x}_o} + \int_{\Omega} J^{(o)}_{\beta,\bar{\beta}}\, d^4x^o \tag{62}$$

where $L^{(o)*}$ is the adjoint of $L^{(o)}$ and where

$$L^{(o)*} \equiv L^{(o)}$$

so that $L^{(o)}$ is formally self adjoint, as is obvious since L was self adjoint. Here also $J^{(o)}_{\beta}$ is formally identical with J_β , with the coordinates x_β replaced by the coordinates x^o_β .

If $\underline{w}$ and $\underline{v}$ are one point tensor fields then (59) and (62) are clearly identical results. However if one or both of $\underline{w}$ and $\underline{v}$ are two point tensor fields of $\underline{x}$ and $\underline{x}_o$, then (59) yields relations between function of $\underline{x}_o$ while (62) yields relations involving functions of $\underline{x}$ which may be different.

The integral relations obtained take a physical meaning when the fields $\underline{v}$ and $\underline{w}$ are specified. In particular we will take $\underline{w}$ to be the displacement field $\underline{u}$ satisfying the equations of motion and boundary conditions for the region Ω surrounding a closed failure region. In this region we take the failure zone to have a volume V_2 with a closed boundary surface Σ while the remaining spatial volume is denoted by

V_1 with an external boundary S, as shown in Figure 2. Thus the boundary of V_1 is $\Sigma \oplus S$ while the boundary of V_2 is Σ. The space-time volume Ω is the four volume occupied by the medium external to Σ as shown in Figure 2. The external boundary of Ω is generated by parallel displacement of S in the direction of the x_4 (time) axis, since S does not change with time. The internal boundary of Ω, however, has generators that are not parallel to the x_4 axis, reflecting the growth of the failure volume with time.

In addition to the space-like boundary conditions expressed by the boundary conditions in (52), which apply on the spatial boundary Σ, there may be conditions on the fields that apply on the time-like boundary of Ω. These may be connected with the space-like conditions in (52) in that they may result from the change in Σ as a function of time, and in any case the conditions along the time-like surface of Ω would correspond to "generalized initial conditions". These general time-like conditions are in fact already contained in the boundary conditions (52) provided we recognize that Σ is a function of time and that the fields may be discontinuous in time as well as in space. We will later show how the time-like discontinuous behavior gives rise to relaxation phenomena that account for the stress wave radiation accompanying the growth of the failure zone in an initially stressed medium.

To complete the description of the physical problem we consider the impulse response of the medium to a simple delta "function" point source. This response is of course provided by the Green's function appearing in equation (53), the role of Green's integral theorem being simply to provide the means of superposing or adding together weighted

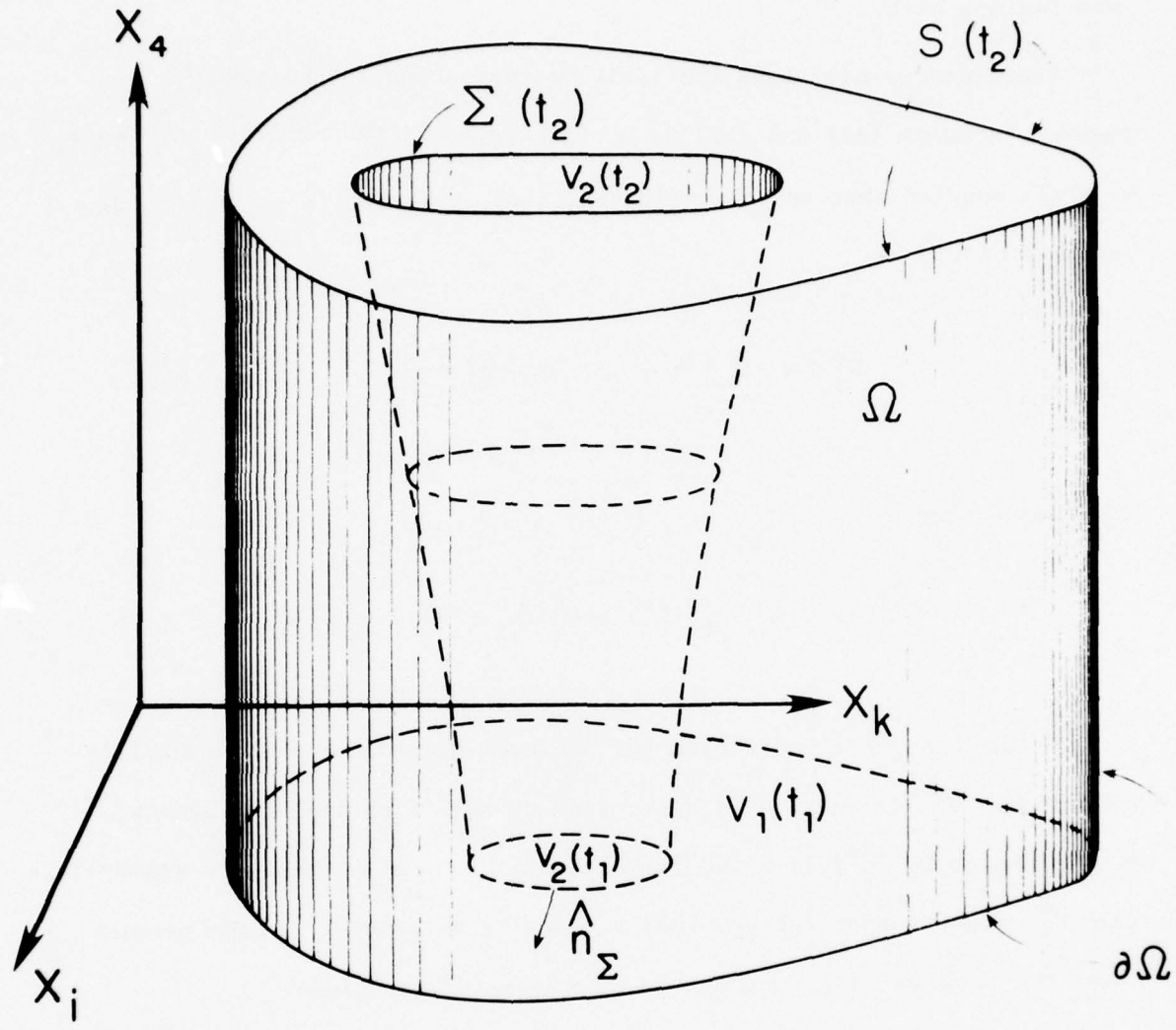

Figure 2: Geometry of the four volume Ω with x_i and x_k spatial coordinates, x_4 the time coordinate. A spatial section through the four dimensional volume Ω^4 at time t_1 is the ordinary spatial volume $V_1(t_1)$, external to the failure region.

Green's functions in such a way as to represent the complex source we are dealing with.

Therefore we will take the field $\mathbf{v}$ appearing in the Green's theorem formulae (59) and (62) to be the two point tensor field $G^{\beta}_{\gamma}(\mathbf{x}, \mathbf{x}_o)$. We shall require that causality is satisifed, that is, (e.g., Morse and Feshbach, 1953)

$$G^{\beta}_{\gamma}(\mathbf{x}, \mathbf{x}_o) = 0 \quad , \quad \text{for} \quad x_4 \leq x^o_4 \tag{63}$$

and hence that

$$G^{\beta}_{\gamma}(x_k, x_4; x^o_k, x^o_4) = G^{\beta}_{\gamma}(x^o_k, -x^o_4; x_k, -x_4) \tag{64}$$

In addition to the differential operator equation and the causality condition, G^{β}_{α} is only fully determined by specification of boundary conditions to be fulfilled and the choice of boundary conditions appropriate for G^{β}_{γ} depends upon the physical problem to be solved. In the present case, the problem is represented by the operator equations:

$$\left.\begin{aligned} L\mathbf{u} &= \rho\mathbf{f} \; ; \; \mathbf{x}\varepsilon\Omega \\ \mathcal{B}\mathbf{u} &= \bar{\mathbf{b}} \; ; \; \mathbf{x}\varepsilon\partial\Omega \end{aligned}\right\} \tag{65}$$

The second equation simply represents the boundary conditions in (52) in compact operational form. In particular $\mathcal{B}$ is a matrix operator with components

$$\mathcal{B}_{\alpha\gamma} \equiv C_{\alpha\beta\gamma\delta}\, n_{\beta} \frac{\partial}{\partial x_{\delta}}$$

so that $S_{\alpha\gamma}\, u_{\gamma} = \tau_{\alpha\beta}\, \eta_{\beta}$. Further, on Σ , $\overline{\mathbf{b}}_{\alpha}$ is the four vector equal to the value of $\tau_{\alpha\beta}\, \eta_{\beta}$ arising from the action of the material within the failure zone enclosed by Σ , which we may take as independently specified. For a physical system governed by operator equations of this form, then $\mathbf{G} \equiv (G^{\beta}_{\gamma})$ is taken to satisfy the homogeneous system (e.g., Stakgold, 1968):

$$\left.\begin{aligned} L\mathbf{G} &= \Delta\,; \quad \mathbf{x}\varepsilon\Omega \\ B\mathbf{G} &= 0\,; \quad \mathbf{x}\varepsilon\partial\Omega \end{aligned}\right\} \tag{66}$$

with L and B being identical operators in (65) and (66). We note that the Green's theorems expressed by (59) and (62) involve the adjoint operators L^{*} and $L^{(o)*}$. Consequently we also define a system adjoint to (66) as

$$\left.\begin{aligned} L^{*}\mathbf{G}^{*} &= \Delta \;\; ; \; \mathbf{x}\varepsilon\Omega \\ B^{*}\mathbf{G}^{*} &= 0 \;\; ; \; \mathbf{x}\varepsilon\partial\Omega \end{aligned}\right\} \tag{67}$$

where $\mathbf{G}^{*}$ is defined as the adjoint Green's function, L^{*} the operator adjoint to L and $B^{*}\,\mathbf{G}^{*} = 0$ as adjoint boundary conditions defined to be such that:

$$(L\mathbf{G},\, \mathbf{G}^{*})^{\mathbf{x}}_{\Omega} = (\mathbf{G},\, L^{*}\mathbf{G}^{*})^{\mathbf{x}}_{\Omega} \tag{68}$$

Referring to the results (59) - (62) we observe, for the system represented by the differential operator and boundary conditions of (65) and the associated systems (66) and (67), that $\mathcal{B}^*$ is determined by the condition that the bilinear concomitant of $\mathbf{G}$ and $\mathbf{G}^*$ vanish.

Noting that

$$L_{\alpha\gamma}\, G_{\gamma}^{\beta}\,(\mathbf{x};\,\mathbf{x}_o) = \Delta_{\alpha}^{\beta}(\mathbf{x};\,\mathbf{x}_o)$$

$$L^{*}_{\alpha\gamma}\, G_{\gamma}^{\beta *}\,(\mathbf{x};\,\mathbf{x}_1) = \Delta_{\alpha}^{\beta}(\mathbf{x};\,\mathbf{x}_1)$$

with $\mathbf{x}_o$ and $\mathbf{x}_1$ arbitrary source points in Ω, and inserting these expressions in the integral relationship (68) involving $\mathbf{G}$ and $\mathbf{G}^*$, we have, using the properties of the delta functions:

$$\left.\begin{aligned} G_{\gamma}^{\beta *}(\mathbf{x}_o;\,\mathbf{x}) &= G_{\gamma}^{\beta}\,(\mathbf{x};\,\mathbf{x}_o) \\ G_{\gamma}^{\beta *}(\mathbf{x};\,\mathbf{x}_o) &= G_{\gamma}^{\beta}\,(\mathbf{x}_o;\mathbf{x}) \end{aligned}\right\} \qquad (69)$$

which is the reciprocity relation. Thus, from (64) and (69) it follows that the causal Green's tensor G_{γ}^{β} has the adjoint given by

$$\left.\begin{aligned} G_{\gamma}^{\beta *}(x_k^o,\, x_4^o;\, x_k,\, x_4) &= G_{\gamma}^{\beta}\,(x_k^o,\, -x_4^o;\, x_k,\, -x_4) \\ G_{\gamma}^{\beta *}(x_k,\, x_4;\, x_k^o,\, x_4^o) &= G_{\gamma}^{\beta}\,(x_k,\, -x_4;\, x_k^o,\, -x_4^o) \end{aligned}\right\} \qquad (70)$$

Now consider the operator $L^{(o)}$, defined to act on the source coordinates $\mathbf{x}_o$. Clearly, interchanging the roles of $\mathbf{x}$ and $\mathbf{x}_o$ in (66) gives

$$L^{(o)}_{\alpha\gamma}\ G^{\beta}_{\gamma}\ (\mathbf{x}_o;\mathbf{x}) = \Delta^{\beta}_{\alpha}\ (\mathbf{x}_o;\mathbf{x}) = \Delta^{\beta}_{\alpha}\ (\mathbf{x};\mathbf{x}_o)$$

$$B^{(o)}_{\alpha\gamma}\ G^{\beta}_{\gamma}\ (\mathbf{x}_o;\mathbf{x}) = 0$$

By the reciprocity relation (69), then

$$\left.\begin{aligned} L^{(o)}_{\alpha\gamma}\ G^{\beta *}_{\gamma}(\mathbf{x};\mathbf{x}_o) &= \Delta^{\beta}_{\alpha}(\mathbf{x};\mathbf{x}_o) \\ B_{\alpha\gamma}\ G^{\beta *}_{\gamma}(\mathbf{x};\mathbf{x}_o) &= 0 \end{aligned}\right\} \qquad (71)$$

Similarly,

$$\left.\begin{aligned} L^{(o)*}_{\alpha\gamma}\ G^{\beta}_{\gamma}\ (\mathbf{x};\mathbf{x}_o) &= \Delta^{\beta}_{\alpha}\ (\mathbf{x};\mathbf{x}_o) \\ B^{(o)*}_{\alpha\gamma}\ G^{\beta}_{\gamma}\ (\mathbf{x};\mathbf{x}_o) &= 0 \end{aligned}\right\} \qquad (72)$$

Now returning to the Green's theorem expressed by (62), where the integration is over the source coordinates $\mathbf{x}_o$, and using $\mathbf{G}$ for $\mathbf{v}$ and $\mathbf{u}$ for $\mathbf{w}$, we have

$$(L^{(o)}\,\mathbf{u},\mathbf{G})^{\mathbf{x}_o}_{\Omega} = (\mathbf{u},\ L^{(o)*}\mathbf{G})^{\mathbf{x}_o}_{\Omega} + \int_{\Omega} J^{\mu}_{\beta,\beta}(\mathbf{u},\mathbf{G})\ d^4x^o \qquad (73)$$

where J^{μ}_{β} is seen from (68) to be

$$J^{\mu}_{\beta} = G^{\mu}_{\alpha}\ (\mathbf{x};\mathbf{x}_o)\ \tau_{\alpha\beta}(\mathbf{x}_o) - u_{\alpha}(\mathbf{x}_o)\ G^{\mu}_{\alpha\beta}\ (\mathbf{x};\mathbf{x}_o) \qquad (74)$$

and where

$$G^{\mu}_{\alpha\beta}(\mathbf{x};\mathbf{x}_o) \equiv C_{\alpha\beta\gamma\delta}(\mathbf{x}_o)\,\frac{\partial G^{\mu}_{\gamma}(\mathbf{x};\mathbf{x}_o)}{\partial x^{o}_{\delta}} \tag{75}$$

From the equations for u_α in (65) we have:

$$(L^{(o)}\mathbf{u},\mathbf{G})^{\mathbf{x}_o}_{\Omega} = \int_{\Omega} \rho f_\alpha G^{\mu}_{\alpha}\, d^4 x^o$$

and from (72) we have that:

$$L^{(o)*}_{\alpha\gamma}\, G^{\mu}_{\gamma} = \Delta^{\mu}_{\alpha}$$

$$(\mathbf{u},\, L^{(o)*}\mathbf{G})^{\mathbf{x}_o}_{\Omega} = \int_{\Omega} \Delta^{\mu}_{\alpha}(\mathbf{x};\mathbf{x}_o)\, u_\alpha(\mathbf{x}_o)\, d^4 x_o$$

$$= \begin{cases} 0\ , & \text{if } \mathbf{x} \notin \Omega \\ 4\pi\, u_\mu(\mathbf{x}), & \text{if } \mathbf{x} \in \Omega \end{cases}$$

Therefore the Green's theorem in (73) yields

$$4\pi\, u_\mu(\mathbf{x}) = \int_{\Omega} \rho(\mathbf{x}_o)\, f_\alpha(\mathbf{x}_o)\, G^{\mu}_{\alpha}(\mathbf{x};\mathbf{x}_o)\, d^4 x^o$$

$$- \int_{\Omega} \frac{\partial}{\partial x^{o}_{\beta}} \left\{ G^{\mu}_{\alpha}(\mathbf{x};\mathbf{x}_o)\, \tau_{\alpha\beta}(\mathbf{x}_o) - u_\alpha(\mathbf{x}_o)\, G^{\mu}_{\alpha\beta}(\mathbf{x};\mathbf{x}_o) \right\} d^4 x^o \tag{76}$$

Now formal application of the divergence theorem to the second integral on the right gives:

$$\int_{\Omega} \frac{\partial}{\partial x^o_\beta}\left[G^\mu_\alpha \tau_{\alpha\beta} - u_\alpha G^\mu_{\alpha\beta}\right] d^4x^o = \int_{\partial\Omega} \left[G^\mu_\alpha \tau_{\alpha\beta} - u_\alpha G^\mu_{\alpha\beta}\right] N_\beta \, d^3x^o \qquad (77)$$

The integral over the boundary $\partial\Omega$ however takes a special form because some of the fields, namely u_α and G^μ_α, are purely space-like, while both $\tau_{\alpha\beta}$ and $G^\mu_{\alpha\beta}$ have, by construction, time-like components. Hence, we can give more explicit form to the "surface" integral in (77) by applying the divergence theorem to the expanded form of the integrand, where $\tau_{\alpha\beta}$ and $G^\mu_{\alpha\beta}$ are written out in terms of the purely space-like fields used in their construction. From the definitions of $\tau_{\alpha\beta}$ and $G^\mu_{\alpha\beta}$ we have

$$\int_{\Omega} \frac{\partial}{\partial x^o_\beta}\left[G^\mu_\alpha \tau_{\alpha\beta} - u_\alpha G^\mu_{\alpha\beta}\right] d^4x^o =$$

$$-\int_{\Omega} \frac{\partial}{\partial x^o_\beta}\left[G^m_k \left\{C_{k\ell ij}\,\delta_{\beta\ell}\frac{\partial u_i}{\partial x^o_j} - \rho\delta_{ik}\delta_{\beta 4}\frac{\partial u_i}{\partial x^o_4}\right\}\right.$$

$$\left. - u_k\left\{C_{k\ell ij}\,\delta_{\beta\ell}\frac{\partial G^m_i}{\partial x^o_j} - \rho\delta_{ik}\delta_{\beta 4}\frac{\partial G^m_i}{\partial x^o_4}\right\}\right] d^4x^o$$

where the latin indices take only the values 1, 2, 3. Regrouping the terms and noting that the ordinary elastic stress is $-\tau_{k\ell}$ and similarly that $-G^m_{k\ell}$ is the elastic stress associated with the displacement G^m_k, we have:

$$\int_{\Omega} \frac{\partial}{\partial x^o_\beta} \left[G^u_\alpha \tau_{\alpha\beta} - u_\alpha G^u_{\alpha\beta} \right] d^4x^o = \int_{\Omega} \frac{\partial}{\partial x^o_\ell} \left[G^m_k \tau_{k\ell} - u_k G^m_{k\ell} \right] d^4x^o$$

$$- \int_{\Omega} \frac{\partial}{\partial x^o_4} \left[u_k \left(\rho \frac{\partial G^m_k}{\partial x^o_4} \right) - G^m_k \left(\rho \frac{\partial u_k}{\partial x^o_4} \right) \right] d^4x^o \qquad (78)$$

Now we observe that the first integral involves a purely spatial divergence of a space-like field, while the second integral involves the purely time-like part of the (four dimensional) divergence of a spatial field. Thus we integrate over only spatial coordinates in the first and over the time coordinate in the second, in the latter case observing that Ω is an explicit function of time since the surface Σ is expanding. In particular, taking the initiation of the process resulting in a dynamic field to begin at $x^o_4 \equiv t_o = 0$ and noting that G^m_k is causal, so that $G^m_k = 0$ when $x^o_4 > x_4$, then

$$\int_{\Omega} \frac{\partial}{\partial x^o_\ell} \left[G^m_k \tau_{k\ell} - u_k G^m_k \right] d^4x^o = \int_o^{t^+} dt^o \int_{\partial v_1} \left[G^m_k \tau_{k\ell} - u_k G^m_{k\ell} \right] n_\ell d\alpha$$

(79)

by an ordinary application of the divergence theorem. Here ∂v_1 is the boundary of the spatial volume v_1 at time t, and n_ℓ is the normal to this spatial boundary, as shown in Figure 2. Also, t^+ denotes $t + \varepsilon$, with $\varepsilon > 0$ and infinitesimal. Here t^+ is used instead of t

alone in order to avoid any (distributional) singularity of the Green's function at the integral limit. Further, we have replaced x_4^o and x_4 by the equivalents t_o and t.

The second integral in (78) demands special care in performing the integration over the time coordinate x_4^o since v_1 is an explicit function of time, so that the integration over the spatial coordinates is to be performed before that over the time coordinate. Further, the resulting integrand for the time integration need not be continuous, as was noted earlier. The integral in question is

$$\int_\Omega \frac{\partial}{\partial x_4^o}\left[u_k\left(\rho\,\frac{\partial G_k^m}{\partial x_4^o}\right) - G_k^m\left(\rho\,\frac{\partial u_k}{\partial x_4^o}\right)\right] d^4x^o =$$

$$\int_o^{t^+} dt_o \int_{v_1(t_o)} \frac{\partial}{\partial t_o}\left[u_k\left(\rho\,\frac{\partial G_k^m}{\partial t_o}\right) - G_k^m\left(\rho\,\frac{\partial u_k}{\partial t_o}\right)\right] dv^o$$

where we let $dv^o \equiv dx_1^o\, dx_2^o\, dx_3^o$ denote the purely spatial volume element. Now we observe that, for a spatial integral of a function F of the medium deformation or flow, evaluated over a volume v_1 with v_1 a function of time t_o :

$$\frac{d}{dt_o}\int_{v_1(t_o)} F\, dv^o = \int_{v_1(t_o)} \frac{\partial F}{\partial t_o}\, dv^o + \int_{\partial v_1(t_o)} F\,\mathbf{U}\cdot\hat{n}\, da$$

which follows from the transport theorem of equation (3). Here the surface integral is due to movement of the boundary ∂v_1 with velocity $\mathbf{U}$. This form is valid no matter

what the value of $\mathbf{U}$, that is whether the boundary of v_1 moves with the material or not. Hence it is immediately applicable to the integral being considered, where we may regard the integrand in brackets as corresponding to F, so that:

$$\int_{\Omega} \frac{\partial}{\partial x_4^o}\left[u_k\left(\rho \frac{\partial G_k^m}{\partial x_4^o}\right) - G_k^m\left(\rho \frac{\partial u_k}{\partial x_4^o}\right)\right] d^4x^o =$$

$$\int_o^{t^+} d \int_{v_1(t_o)} \left[u_k\left(\rho \frac{\partial G_k^m}{\partial t_o}\right) - G_k^m\left(\rho \frac{\partial u_k}{\partial t_o}\right)\right] dv^o$$

$$- \int_o^{t^+} dt_o \int_{\partial v_1(t_o)} \left[u_k\left(\rho \frac{\partial G_k^m}{\partial t_o}\right) - G_k^m\left(\rho \frac{\partial u_k}{\partial t_o}\right)\right] U_\ell n_\ell d\alpha^o \qquad (80)$$

where the first term on the right hand side must be considered as a Stieljes integral (Archambeau, 1972; Minster, 1973).

In the theory of elastic continua and in linear continuum theory the second integral in (80) is neglected since the boundary movement is with the particle velocity and the integral term is small - a second order effect due to transport which is negligible for solids. However, when the boundary is not simply a material boundary and may in fact move with a normal velocity $\underline{U}\cdot\hat{n}$ much larger than the particle velocity, then this term cannot be neglected since it may, in fact, be as large as the traction term at the boundary. We are dealing with precisely the case in which $\underline{U}$ may be large along that part of the boundary of V_1 corresponding to Σ and so the term will be retained for integration over the "phase transition" boundary Σ. It can, however, be neglected on other boundaries corresponding to regular material boundaries or external

boundaries of the medium, since there $U_\ell n_\ell$ has the value of the particle velocity. For consistency with previous neglect of second order terms we are in fact forced to neglect material boundary position variations for which U_ℓ in (80) is equal to the particle velocity. In expressing (80), however, we will retain $\partial\nu_1$ for the surface integral limit, but consider U_ℓ to be zero on material boundaries, which in effect neglects this transport integral term for boundaries other than Σ . In addition, $\underline{U}$ is of course a spatial function so that its value may be negligible on parts of the surface Σ as well. Indeed, for spontaneous failure processes we would expect it to be of the order of the particle velocity over much of the failure surface except near the expanding "edges" of the failure zone,which usually has a elongated shape. The magnitude of $\underline{U}$ on Σ is of course determined by the jump conditions in (32), so that $\underline{U}$ is not arbitrary but determined by the radiation field itself. The shape of the failure boundary is thus determined by the spatial variation of $\underline{U}$, so that some parts of Σ may move rapidly while other sections may simply move with the particles as a simple material boundary.

Now substituting (79) and (80) into (78) yields:

$$\int_\Omega \frac{\partial}{\partial x^o_\beta}\left[G^\mu_\alpha\,\tau_{\alpha\beta} - u_\alpha\,G^\mu_{\alpha\beta}\right]d^4x_o =$$

$$\int_o^{t^+} dt_o \int_{\partial\nu_1}\left[G^m_k\left(\tau_{k\ell} - \rho\,\frac{\partial u_k}{\partial t_o}\,U_\ell\right) - u_k\left(G^m_{k\ell} - \rho\,\frac{\partial G^m_k}{\partial t_o}\,U_\ell\right)\right]n_\ell\,da^o$$

$$- \int_o^{t^+} d\left\{\int_{\nu_1(t_o)} \rho\left[u_k\,\frac{\partial G^m_k}{\partial t_o} - G^m_k\,\frac{\partial u_k}{\partial t_o}\right]d\nu^o\right\} \qquad (81)$$

From previous definitions of $\tau_{\alpha\beta}$ and $G^{\mu}_{\alpha\beta}$ and from the definition of the elastic-inertial tensor we have

$$\tau_{\alpha\beta}\,\eta_\beta = \left[\tau_{k\ell} - \rho\,\frac{\partial u_k}{\partial t_o}\,U^*_\ell\right] n_\ell$$

$$G^{\mu}_{\alpha\beta}\,\eta_\beta = \left[G^m_{k\ell} - \rho\,\frac{\partial G^m_k}{\partial t_o}\,U^*_\ell\right] n_\ell$$

However as previously noted, we must neglect terms involving products of the particle velocities in comparison with traction terms or terms involving products of the particle velocity and $U_\ell n_\ell$. Therefore we can replace U^*_ℓ appearing in these identities by U_ℓ alone. Thus in this linearized theory we use

$$\left.\begin{aligned}\tau_{\alpha\beta}\,\eta_\beta &= [\tau_{k\ell} - \rho\,\frac{\partial u_k}{\partial t_o}\,U_\ell]n_\ell \\ G^{\mu}_{\alpha\beta}\,\eta_\beta &= [G^m_{k\ell} - \rho\,\frac{\partial G^m_k}{\partial t_o}\,U_\ell]n_\ell\end{aligned}\right\} \qquad (82)$$

and observe that these factors appear in (81). Further, we observe that, from (74)

$$J^{\mu}_4 = \rho\left[u_k\,\frac{\partial G^m_k}{\partial t_o} - G^m_k\,\frac{\partial u_k}{\partial t_o}\right]$$

Using these identities in the integrals in (81), we get

$$\int_\Omega \frac{\partial}{\partial x^o_\beta}\left[G^{\mu}_{\alpha}\,\tau_{\alpha\beta} - u_\alpha\,G^{\mu}_{\alpha\beta}\right]d^4x_o = \int_o^{t^+} dt_o \int_{\partial v_1} J^{\mu}_\beta\,\eta_\beta\,da^o -$$

$$\int_o^{t^+} d\left[\int_{v_1} J^{\mu}_4\,dv^o\right] \qquad (83)$$

Thus the basic representation theorem for $u_\gamma(\mathbf{X})$, expressed by equation (76), is

$$4\pi\, u_\mu(\mathbf{X}) = \int_\Omega \rho f_\alpha\, G_\alpha^\mu \; d^4x_o - \int_o^{t^+} dt_o \int_{\partial\nu_1} J_\beta^\mu\, \eta_\beta \, da^o + \int_o^{t^+} d\left[\int_{\nu_1} J_4^\mu \, d\nu^o\right] \tag{84}$$

Here

$$J_\beta^\mu = G_\alpha^\mu\, \tau_{\alpha\beta} - u_\alpha\, G_{\alpha\beta}^\mu$$

and

$$\eta_\beta = (n_1, n_2, n_3, -\,\mathbf{U}\cdot\hat{n})$$

Written out explicitly in three dimensional spatial components, this result takes the form:

$$\begin{aligned} 4\pi u_m(\mathbf{X}) = {} & \int_o^{t^+} dt_o \int_{\nu_1} \rho\, f_k\, G_k^m \, d^3x_o \\ & + \int_o^{t^+} dt_o \int_{\partial\nu_1} \left[G_k^m \left(C_{ijk\ell} \frac{\partial u_i}{\partial x_j^o} + \rho \frac{\partial u_k}{\partial t_o}\, U_\ell \right) \right. \\ & \left. - u_k \left(C_{ijk\ell} \frac{\partial G_i^m}{\partial x_j} + \rho \frac{\partial G_k^m}{\partial t_o}\, U_\ell \right) \right] n_\ell\, da^o \\ & + \int_o^{t^+} d \int_{\nu_1} \rho \left[u_k \frac{\partial G_k^m}{\partial t_o} - G_k^m \frac{\partial u_k}{\partial t_o} \right] d\nu^o \end{aligned} \tag{85}$$

Here ρ and $C_{ijk\ell}$ are functions of the spatial coordinates x_k^o alone.

6. Approximate Radiation Field Solutions for Growing Failure Zones

The fields u_γ and G_γ^β satisfy the boundary conditions

$$\left.\begin{aligned} B_{\alpha\gamma}\, u_\gamma &= \bar{b}_\alpha \quad ; \quad \underline{x}\in\partial\Omega \\ B_{\alpha\gamma}\, G_\gamma^\beta &= 0 \quad ; \quad \underline{x}\in\partial\Omega \end{aligned}\right\} \tag{86a}$$

or, equivalently

$$\left.\begin{aligned} \tau_{\alpha\beta}^{(1)}\eta_\beta &= \tau_{\alpha\beta}^{(2)}\,\eta_\beta \quad ; \quad \underline{x}\in\partial\Omega \\ G_{\alpha\beta}^{(1)\mu}\,\eta_\beta &= 0 \quad ; \quad \underline{x}\in\partial\Omega \end{aligned}\right\} \tag{86b}$$

where the superscripts (1) and (2) refer to the quantities evaluated by limits on the surface approached from the inside or from the outside of Ω, respectively. Thus the result in (84) reduces to:

$$4\pi u_\mu(\underline{x}) = \int_\Omega \rho\, f_\alpha\, C_\alpha^\mu\, d^4x_o - \int_o^{t^+} dt_o \int_{\partial v_1} G_\alpha^\mu[\tau_{\alpha\beta}^{(2)}\,\eta_\beta]\, da^o$$

$$+ \int_o^{t^+} d\left[\int_{v_1} J_4^\mu\, dv^o\right] \tag{87}$$

with $\tau^{(2)}_{\alpha\beta}$ "prescribed" on the boundary of v_1 . The reduction of (84) to (87) is a consequence of the choice of the Green's function, which eliminates the integral involving the unknown displacement field u_α on the boundary of v_1 , as well as from the fact that the "generalized tractions" $\tau_{\alpha\beta}\,\eta_\beta$ appear explicitly in the boundary integral over ∂v_1 so that the "jump condition" $\left[\!\left[\tau_{\alpha\beta}\,\eta_\beta\right]\!\right] = 0$ can be used to introduce the action of the material external to v_1 at the boundary of v_1 .

It is clear, however, that determination of the Green's function satisfying the boundary conditions in (86) is at best difficult and quite impractical for applications in view of the necessity of satisfying boundary conditions on the growing failure boundary as well as on the material boundaries of the medium. We can, instead, introduce a Green's function Γ^β_α defined on a space Ω' that includes the problem space Ω , *i.e.*, $\Omega\subset\Omega'$. In particular we can take Ω' to be the space bounded by the same external boundaries as Ω but without the internal boundary created by the failure zone. Then Γ^β_γ is given by

$$\left.\begin{aligned} L_{\alpha\gamma}\,\Gamma^\beta_\gamma(\underline{x}\,;\,\underline{x}_o) &= \Delta^\beta_\alpha(\underline{x}\,;\,\underline{x}_o) \quad ; \quad \underline{x}\in\Omega' \\ B_{\alpha\gamma}\,\Gamma^\beta_\gamma(\underline{x}\,;\,\underline{x}_o) &= 0 \quad ; \quad \underline{x}\in\partial\Omega' \end{aligned}\right\} \tag{88}$$

where $L_{\alpha\beta}$ is defined throughout Ω' as if the whole medium were in its initial, unfailed state. The Green's function defined by (88) has the same properties as G_α^β and is also such that inner products over the subregion Ω of Ω' can be defined. Thus the Green's representation of (84) is reproduced, with G_α^μ replaced by Γ_α^μ. However the price paid for the presence of the simpler Green's function is that (84) cannot be reduced to the simple form of the solution given in (87). In particular, we get, from (84) and (88)

$$4\pi\, u_\mu(\underline{x}) = \int_\Omega \rho\, f_\alpha\, \Gamma_\alpha^\mu\, d^4x_o - \int_o^{t^+} dt_o \int_{\partial\nu_1} \Gamma_\alpha^\mu[\tau_{\alpha\nu}^{(2)}\ \eta_\beta]\, da^o$$

$$+ \int_o^{t^+} dt_o \int_{\partial\nu_1 \ominus \partial\nu_1'} u_\alpha\, [\gamma_{\alpha\beta}^\mu\ \eta_\beta]\, da^o + \int_o^{t^+} d\left[\int_{\nu_1} J_4^\mu\, d\nu^o\right] \qquad (89)$$

where $\partial\nu_1 \ominus \partial\nu_1'$ is the difference between the spatial boundaries of Ω and Ω'. With Ω' defined as above this is just the failure surface Σ. Here $\gamma_{\alpha\beta}^\mu$ is the "generalized Green's stress tensor" associated with Γ_α^μ, that is

$$\gamma_{\alpha\beta}^\mu(\underline{x}\ ;\ \underline{x}_o) = C_{\alpha\beta\gamma\delta}(\underline{x}_o)\, \frac{\partial \Gamma_\gamma^\mu}{\partial x_\delta^o}$$

and J_4^μ is obtained from

$$J_\beta^\mu = \Gamma_\alpha^\mu\, \tau_{\alpha\beta} - u_\alpha\, \gamma_{\alpha\beta}^\mu$$

Thus we get an extra integral in (89) involving u_α on the failure boundary Σ. Clearly this term arises from the fact that we have in effect relaxed the boundary conditions required for the Green's function.

The natural boundary conditions on Σ do not involve u_α directly, but instead specify conditions relating space and time derivatives of u_α across Σ, *i.e.*, $\left[\!\left[\tau_{\alpha\beta}\ \eta_\beta\right]\!\right]_\Sigma = 0$. Hence u_α on Σ is unknown and (95) is an integral equation for $u_\mu(\underline{x})$ rather than a solution.

Note that instead of the Green's function Γ^μ_γ, we can use the infinite space Green's function $\bar{\Gamma}^\mu_\gamma$. The latter affords a relatively simple closed form expression (e.g., Maruyama, 1963). In that case, however, the boundary integral over $\partial v_1 \ominus \partial v_1'$ in the representation theorem (89) extends over all boundaries of v_1, including exterior boundaries as well as Σ. In addition, we must consider the process to occur in an isotropic and homogeneous space from the onset. This is quite an acceptable assumption, to first order at least, in the vicinity of the failure zone.

Successive approximations to the solution of (89) can be obtained by iteration. In this particular case we take the first iterate, $u^I_\mu(\underline{x})$, to be the final term in (89), the "relaxation", or "initial value" term. Hence, using the infinite space Green's function we define:

$$4\pi\, u^I_\mu(\underline{x}) = \int_o^{t^+} d\left[\int_{v_1} \bar{J}^\mu_4\, dv^o\right] \tag{90}$$

A correction to this term, which yields the next iterate $u_\mu^{II}(\underline{x})$ is defined by

$$4\pi\left[u_\mu^{II}(\underline{x}) - u_\mu^{I}(\underline{x})\right] = \int_o^{t^+} dt_o \int_\Sigma u_\alpha^I \left[\bar{\gamma}_{\alpha\beta}^{\mu}\ \eta_\beta\right] d\alpha^o$$

$$- \int_o^{t^+} dt_o \int_\Sigma \bar{\Gamma}_\alpha^\mu \left[\tau_{\alpha\beta}^I\ \eta_\beta\right] d\alpha^o \qquad (91)$$

where the integration is only over the failure surface Σ . (Generally the volume integral over the body force density f_α is neglected as being small and is not included.) In the past we have referred to $\underline{u}^I(\underline{x})$ as the "transparent source approximation to the direct source field", since it neglects the scattering at the failure boundary. The field $\underline{u}^{II}(\underline{x})$ will simply be referred to as the "approximate direct source field".

By adding a general eigenfunction expansion with adjustable coefficients, which is regular everywhere in the domain Ω (or Ω'); one can then satisfy boundary conditions on the other boundaries. For example, for a problem involving failure in the Earth, we could use a layered spherical model, and hence a vector spherical harmonic expansion for each layer zone. One could also express the Green's function Γ_α^μ in (89) as an eigenfunction expansion and use it in place of $\bar{\Gamma}_\alpha^{\ \mu}$ in (90) and (91) to obtain, directly, the approximate source fields in the domain Ω' .

It is clear that the relaxation or initial value term plays a dominant role in this procedure. In fact, we have pointed out that it represents the essentials of the elastic wave radiation attributable to the source. Therefore we will consider its expression in more explicit and simplified form for spontaneous processes such as failure under a static or quasi-static initial stress condition. Related investigations have also been considered by Archambeau (1968, 1972) and Minster (1973).

If we consider the field $u^I(\underline{x})$ at any particular time t_1 we can represent its evolution at any later time t in terms of the initial value integral (e.g., Love, 1944)

$$4\pi\, u_m^I(\underline{x},\, t;\, t_1) = \int_{v_1(t_1)} \rho \left[u_k \frac{\partial G_k^m}{\partial t_o} - G_k^m \frac{\partial u_k}{\partial t_o} \right]_{t_o = t_1} dv^o$$

This expression in the radiation field due to all effects occurring up to time t_1, including prior rupture growth. It is therefore the radiation that would be observed for $t > t_1$ if the failure zone boundary were fixed for times $t > t_1$. If we now consider the same initial value representation of the field at $t_1 + \delta t_1$, where some additional change in the failure boundary has occurred in the time increment δt_1, then the difference in the radiation fields is given by

$$u_m^I(\underline{x},\, t;\, t_1 + \delta t_1) - u_m^I(\underline{x},\, t;\, t_1) =$$

$$\frac{\delta t_1}{4\pi} \int_{v_1(t_1 + \delta t_1)} \rho \left[\left(\frac{\partial u_k^*}{\partial t_o} \right) \frac{\partial G_k^m}{\partial t_o} \right]_{t_o = t_1} dv^o + O(\delta t_1^2)$$

where $\left.\frac{\partial u_k^*}{\partial t_o}\right|_{t_o=t_1} \delta t_1$ is the incremental initial value, equal to the change in the equilibrium field caused by incremental growth of the failure zone, and where we have used the fact that accelerations remain finite so that the velocity is continuous.

Dividing through by δt_1, and taking the limit as δt_1 approaches zero gives

$$\frac{\partial u_m^I(\underline{x},\, t;\, t_1)}{\partial t_1} = \frac{1}{4\pi} \int_{v_1(t_1)} \left[\left(\frac{\partial u_k^*}{\partial t_o}\right) \frac{\partial G_k^m}{\partial t_o}\right]_{t_o = t_1} dv^o \qquad (92)$$

For failure occurring at a finite rate and of total duration τ, then the derivative with respect to t_1 vanishes for $t_1 > \tau$. Thus integration of (92) yields

$$u_m^I(\underline{x},\, t) = c(\underline{x},\, t) + \frac{1}{4\pi} \int_o^{\min(t,\tau)} dt_1 \int_{v_1(t_1)} \left[\left(\frac{\partial u_k^*}{\partial t_o}\right) \frac{\partial G_k^m}{\partial t_o}\right]_{t_o = t_1} dv^o \qquad (93)$$

where the constant of integration is fixed by the choice of reference equilibrium state. If we chose to measure u_m relative to the final equilibrium state after the complete boundary has been formed, then

$$c(\underline{x},\, t) = u_m^*(\underline{x},\, t) - u_m^*(\underline{x},\, \tau)$$

so that

$$u_m(\underline{x},\, 0) = u_m^*(\underline{x}, 0) - u_m^*(\underline{x},\, \tau)$$

If we refer the displacements to the initial equilibrium state then $c(\underline{x}, t) = 0$. In either case $c(\underline{x}, t)$ vanishes for $t > \tau$. This result is formally exact; if Γ_{α}^{μ} or $\overline{\Gamma}_{\alpha}^{\mu}$ is used, however, source boundary scattering is neglected. On the other hand, the equilibrium field changes expressed by $u_{\ell}^{*}(\underline{x}_o, t_o)$ account for both the spatial and temporal behavior of the failure boundary, so that the only term neglected, as expressed approximately in (91) represents the dynamic interaction of the radiation field and the boundary, that is scattering. We expect this scattering to be significant only for wave lengths smaller than the characteristic source dimension. This is confirmed by the results of Burridge (1975), Koyama et al. (1973) and Minster and Suteau (1976). These authors considered expanding spherical failure zones in an uniformly prestress infinite space. Scattering by Σ is shown to affect the spectrum only for frequencies greater that the source characteristic frequency $f_c = \overline{U}_R/L$, where L is the maximum source dimension and $\overline{U}_R$ the average failure rate, and the effects are not large. In the time domain, the "transparency" approximation leads to a minor shortening of the far-field pulse and elimination of its small amplitude oscillatory coda.

7. Conclusions and Consequences

Some of the conclusions that we have drawn from the results of the work described are:

(1) Conservation relations expressed on an expanding material transition surface (or failure zone boundary) show that traction and particle velocity jumps across such a boundary cannot be specified independently, as has been (implicitly) assumed, for example, in dislocation and stress pulse (crack theory) models for failure. In

particular, it has been shown that the proportionality factor between particle velocity changes and traction changes across the failure boundary is ρU_R, with U_R the rupture rate and ρ the initial material density.

(2) Introduction of a transition energy function provides a means of characterizing failure processes in terms of energy requirements. This function can be determined from seismically estimated rupture variables--in particular from the stress drop (on the failure boundary) and the rupture velocity. Hence the transition energy (density) function can be obtained for natural failure processes and compared to laboratory determined values which should lead to a more complete quantitative description and subsequent understanding of failure processes in the earth. (See also Husseini et al., 1975.)

(3) Since rupture rates have been shown to be directly proportional to stress drops on the failure boundary and also proportional to the change in the material moduli, it follows that observations of high rupture rates for earthquakes, near the shear velocity of the medium, imply near total loss of shear strength and probable melting during failure. (See also Archambeau, 1976.)

(4) The Green's function solution for the radiation field exterior to the failure zone shows that the field depends explicitly on the failure boundary growth rate, whereas previous radiation field representations did not contain any such explicit dependence since dynamical boundary conditions were ignored in favor of heuristic kinematical representations of boundary growth effects. This suggests that source representations such as those generated by displacement dislocations and stress pulse equivalents, that are formulated entirely in terms of equivalent *applied* boundary displacements or equivalent *applied* boundary tractions, must be carefully reconsidered

since, at present, they do not account for the boundary integral terms involving the surface growth rate (i.e., the surface integral terms with integrands involving U_{ℓ} explicitly, as given for example in equation (85)).

(5) The Green's function solution shows that an appropriate first order representation of the radiation field is obtained using the "initial value" or "relaxation" term in the Green's integral representation. The radiation field predictions based on this integral representation can be directly related to the physical parameters for the failure process (i.e., the transition energy and the material rheology moduli before and after failure as well as the rupture rate and stress level changes) and can be used for the representation of the radiation from complex failure phenomena in inhomogeneous media that is also inhomogeneously prestressed. Since strong prestress inhomogeneities are considered to be present for most if not all failure processes (especially for earthquakes) and to have a very important effect on the character of the radiated elastic wave field, then it follows that the ability to theoretically predict the field from such complex sources is critical to the advancement of understanding of the mechanics of failure processes, particularly in the earth.

Acknowledgements

This research has been supported under Advanced Research Projects Agency, Department of Defense, Contracts F 44620-72-C-0078 and F 44620-72-C-0083 monitored by the Air Force Office of Scientific Research and the Air Force Cambridge Research Laboratory monitored contract No. F 19628-76-C-0061. A part of this work was also supported by the National Science Foundation under grants GI-44212 and DES 75-20137.

References

Archambe..., C. B., 1964. Elastodynamic Source Theory, Ph.D. Thesis, California Institute of Technology, Pasadena, California.

Archambeau, C. B., 1968. General Theory of Elastodynamic Source Fields, Rev. Geophys., 16, 241-288.

Archambeau, C. B., 1969. Elastodynamic Representation Theorems in Prestress Elastic Media with Moving Boundaries, Abstract, SSA Meeting, St. Louis, Missouri.

Archambeau, C. B., 1972. The Theory of Stress Wave Radiation from Explosions in Prestressed Media, Geophys. J. R. astr. Soc., 29, 329-366. (Appendix, Geophys. J. R. astr. Soc., 31, 361-363, 1973.)

Archambeau, C. B., 1976. Shear Stress in the Earth's Lithosphere: Estimates Based on the Analysis of Seismic Radiation, to be published in Pure and Applied Geophysics, Special Issue on Stress in the Earth, February, 1977.

Burridge, R., 1975. The Pulse Shape and Spectra of Elastic Waves Generated when a Cavity Expands in an Initial Shear Field, J. Geophys. Res., 80, 2606-2607.

Burridge, R., 1976. Reply to Commentary by J. A. Snoke, J. Geophys. Res., 81, 1037.

DeGroot, S. R., and P. Mazur, 1969. Non-Equilibrium Thermodynamics, North-Holland.

Edelen, G. B., 1962. The Structure of Field Space, U. of Calif. Press.

Eringer, A. C., 1971, 1975. Continuum Physics, Vol. I and II, Academic Press, New York.

Fletcher, D. C., 1974. The Conservation Laws of Three Dimensional Linearized Elasticity Theory, Ph.D. Thesis, California Institute of Technology, Pasadena, California.

Freund, L. B., 1970. Conditions at a Propagation Interface of Two Media, Transactions of the ASME, Applied Mechanics Division, 190-192.

Fung, Y. C., 1965. Foundations of Solid Mechanics, Prentice-Hall Series in Dynamics.

Husseini, M. I., D. B. Jovanavich, M. J. Randall, and L. B. Freund, 1975. The Fracture Energy of Earthquakes, Geophys. J. R. astr. Soc., 43.

Koyama, J., S. E. Hariuchi, and T. Hirasawa, 1973. Elastic Wave Generated from Sudden Vanishing of Rigidity in a Spherical Region, J. Phys. Earth, 21, 213-226.

Kupradze, V. D., 1963. Dynamical Problems in the Theory of Elasticity, in Progress in Solid Mechanics, Vol. III, Sneddon and Hill, Ed., North Holland, Amsterdam.

Love, A. E. H., 1944. A Treatise on the Mathematical Theory of Elasticity, Dover,

Maruyama, T., 1963. On the Force Equivalents of Dynamic Elastic Dislocations with Reference to the Earthquake Mechanism, Bull. Earthq. Res. Inst. Tokyo, 41, 467.

Mason, W. P., 1966. Physical Acoustics, Vol. III, Part A, The Effect of Imperfections, Academic Press.

Minster, J. B., 1973. Elastodynamics of Failure in a Continuum, Ph.D. Thesis, California Institute of Technology, Pasadena, California.

Minster, J. B., and A. M. Suteau, 1976. Far-Field Waveforms from an Arbitrarily Expanding, Transparent Spherical Cavity in a Prestressed Medium, J. Geophys. Res., in press.

Morse, P.M., and H. Feshbach, 1953. Methods of Theoretical Physics, Parts I and II, McGraw Hill.

Randall, M. J., 1964. On the Mechanism of Earthquakes, Bull. Seism. Soc. Amer., 54, 1283.

Randall, M. J., 1966. Seismic Radiation from a Sudden Phase Transition, J. Geophys. Res., 71, 5297.

Snoke, J. A., 1976. Implications of Moving Boundaries in Elastodynamics: Comments on "The Pulse Shapes and Spectra of Elastic Waves Generated when a Cavity Expands in an Initial Shear Field" by Robert Burridge, J. Geophys. Res., 81, 1035-1036.

Stakgold, I., 1968. Boundary Value Problems of Mathematical Physics, Vol. I and II, MacMillan Publishing Co.